Towards Majorana Bound States Induced by Ferromagnets in Nanowires

by

Yifan Jiang

Bachelor of Science in Electrical Engineering, Pennsylvania State University, 2014

Bachelor of Science in Physics, Pennsylvania State University, 2014

Master of Science in Electrical Engineering, University of California, Los Angeles, 2016

Submitted to the Graduate Faculty of the

Dietrich School of Arts and Sciences in partial fulfillment

of the requirements for the degree of

Doctor of Philosophy

University of Pittsburgh

2023

UNIVERSITY OF PITTSBURGH

DIETRICH SCHOOL OF ARTS AND SCIENCES

This dissertation was presented

by

Yifan Jiang

It was defended on

April 24, 2023

and approved by

Robert P. Devaty, Associate Professor, Department of Physics and Astronomy

W. Vincent Liu, Professor, Department of Physics and Astronomy

David Turnshek, Professor, Department of Physics and Astronomy

Vincent M. Sokalski, Associate Professor, Department of Material Science and Engineering, Carnegie Mellon University

Dissertation Director: Sergey M. Frolov, Associate Professor, Department of Physics and Astronomy

Copyright © by Yifan Jiang

2023

Towards Majorana Bound States Induced by Ferromagnets in Nanowires

Yifan Jiang, PhD

University of Pittsburgh, 2023

Majorana bound states are topological states predicated in condensed matter physics. These states obey non-Abelian statistics and are promising candidates for topological quantum computing. Hybrid superconductor-semiconductor nanowires are believed to be platforms for Majorana bound states and experimental signatures have been reported in the past ten years. Nevertheless, there is still no strong evidence confirming observation of these topological states since these signatures may be attributed to trivial states.

This thesis focuses on semiconductor nanowire devices with ferromagnets. We first discuss the local magnetic field effect induced by ferromagnets. By numerical simulations, we demonstrate how to induce and manipulate Majorana bound states in a Majorana nanowire or T-junction with ferromagnets. Hybrid superconductor-semiconductor nanowire devices with ferromagnets are fabricated. In quantum transport measurements, we observe hysteretic supercurrents and zero-bias peaks of differential conductance in these devices. Additionally, we observe long zero-bias peaks at zero applied magnetic field but at finite local magnetic field generated by ferromagnets. Even though a zero-bias peak is a signature of Majorana bound states, trivial Andreev bound states may also explain above observations. Future experiments based on hybrid devices with ferromagnets may give us insight into Majorana bound states and their applications in topological quantum computing.

Table of Contents

Acknowledgment xxvii

1.0 Introduction 1

1.1 Majorana Bound States and Semiconductor Nanowire Devices 1

1.2 Semiconductor Nanowire Devices with Ferromagnetic Components 2

1.3 Other Majorana Fermions and Motivations 3

1.4 Thesis Outline 4

2.0 Basic Theory 6

2.1 Majorana Bound States and Kitaev Chain 6

2.1.1 A Chain of Sites and Majorana Operators 6

2.1.2 Majorana Bound States in the Kitaev Chain Model 9

2.1.3 Bulk-edge Correspondence 12

2.1.4 Issues of Kitaev Chain Model for Experiments 17

2.1.5 A More Feasible Model for MBSs 18

2.2 Quantum Dots 24

2.2.1 The General Physical Picture of Quantum Dots 24

2.2.2 Coulomb Blockade and Constant-interaction Model 29

2.2.3 Semiconductor Nanowire Devices and Quantum Dots 35

2.3 Superconducting Proximity and Andreev Bound States 35

2.3.1 Superconducting Proximity and Andreev Reflection 36

2.3.2 Andreev levels and Andreev Bound States 41

2.3.3 Resonant Transmission and the Signature of Majorana Bound States 46

3.0 Methods of Device Fabrication and Experiments 49
3.1 InSb and InAs Nanowires 49
3.2 Device Fabrication Based on Nanowires 52
3.2.1 Gate Chips 53
3.2.2 Thin Film Deposition 56
3.2.3 Lithography 58
3.2.4 Processing of Nanowires 61
3.3 Measurement Setups 64
3.3.1 Dilution Refrigerators 64
3.3.2 Measurement System 65
3.3.3 More about Measurement Setup 66
4.0 Local Magnetic Field Effect in InSb Nanowire Devices 71
4.1 Ferromagnetic Materials 71
4.2 Ferromagnetic Contacts to InSb Nanowires 75
4.3 Hysteretic Magnetoresistance in a Device with Ferromagnetic Contacts 79
4.3.1 Two-terminal Device without Ferromagnetic Components 80
4.3.2 Two-terminal Device with Ferromagnetic Contacts 82
4.3.3 Four-terminal Device with Ferromagnetic Contacts 83
4.4 Hysteretic Magnetoresistance in a Device without Ferromagnetic Contacts 87
4.4.1 Local Magnetic Field Effect in InSb Nanowire Devices 88
4.4.2 Numerical Simulations of Ferromagnets 92
5.0 Local Magnetic Field Effect for Majorana Bound States 97
5.1 Method of Simulation 98

5.2 Numerical Results 99
5.2.1 Stray Fields of a Bar Magnet 99
5.2.2 Dragonfly Setup 101
5.2.3 Double Dragonfly Setup 106
5.2.4 Braiding of Majorana Bound States in a T-junction 111
5.3 Preliminary Evaluation of Magnetization Pattern from Magnetic Force Microscopy 115
6.0 Andreev Bound States under Local Magnetic Field Profiles 119
6.1 Superconductor-semiconductor-superconductor Junctions 120
6.1.1 S-N-S Junctions Based on InSb Nanowires 120
6.1.2 Hysteresis in S-N-S Devices 122
6.2 Superconductor-semiconductor Junctions 128
6.2.1 S-N Junctions Based on InAs Nanowires 128
6.2.2 Visually Long ZBPs in S-N Junctions 134
6.3 More Comments on S-N Junctions 139
6.3.1 Induced Superconducting Gap and Shift from Measurement Setups 139
6.3.2 Charge Jumps 140
6.3.3 More Examples of ABSs 141
6.3.4 ZBPs, MBSs and ABSs 143
7.0 Conclusions and Outlook 144
7.1 Conclusions of the Thesis 144
7.2 Efforts for Searching MBSs 146
7.2.1 Superconducting Proximity 147

7.2.2 Spin-orbit Interaction **148**

7.2.3 Development of Chemical Potential Tuning **148**

7.2.4 Other Development **148**

7.2.5 Personal Comment on the History of Searching for MBSs in Hybrid Superconductor-semiconductor Nanowire Devices **149**

7.3 Outlook **150**

Appendix A Recipes of Fabrication **152**

Appendix B List of Publications **157**

Appendix C Links of Available Data **158**

Bibliography **159**

List of Tables

Table 5.1. Energies of MBSs in Figure 5.16.. 114

List of Figures

Figure 2.1. A quantum wire on a superconductor's surface.. 8

Figure 2.2. Diagrams of Kitaev chain model and different types of pairing. Figure 2.1 (a) shows a chain of sites. Figure 2.1 (b) shows the trivial case. Figure 2.1 (c) shows the topological case.. 10

Figure 2.3. Energy spectrum of the Kitaev ring model at different chemical potentials when $\Delta = w$. Figure (c) and (d) show the topological case and Figure (a), (b), (e) and (f) show the trivial case. $\mu = \pm 2\ w$ are critical points of topological phase transition............ 16

Figure 2.4. Energy spectrum of the Kitaev ring model at different chemical potentials when $\Delta = 0.2\ w$. Figure (c) and (d) show the topological case and Figure (a), (b), (e) and (f) show the trivial case. $\mu = \pm 2\ w$ are critical points of topological phase transition... 17

Figure 2.5. Energy spectrum of the hybrid superconductor-semiconductor nanowire model. The chemical potential is 0.2 meV. (a) $B = 0$, $\alpha_R = 0$ and $\Delta = 0$. (b) $B = 0$, $\alpha_R = 20$ meV·nm and $\Delta = 0$. (c) $B = 0.05$ meV, $\alpha_R = 20$ meV·nm and $\Delta = 0$. (d) $B = 0.05$ meV, $\alpha_R = 20$ meV·nm and $\Delta = 0.25$ meV. 21

Figure 2.6. Energy spectrum of the hybrid superconductor-semiconductor nanowire model at different Zeeman fields. The parameters are: $\mu = 0.2$ meV, $\alpha_R = 20$ meV·nm and $\Delta = 0.25$ meV. (a) $B = 0.3$ meV. (b) $B = B_c$. (c) $B = 0.35$ meV....................................... 22

Figure 2.7. Energy spectrum of the hybrid superconductor-semiconductor nanowire model at different chemical potentials. The parameters are: $B = 0.35$ meV, $\alpha_R = 20$ meV·nm and $\Delta = 0.25$ meV. (a) $\mu = 0.15$ meV. (b) $\mu = \mu_c$. (c) $\mu = 0.3$ meV. 23

Figure 2.8. A diagram of a semiconductor nanowire quantum dot device. Gates G_1 and G_3 define a dot by creating potential barriers and gate G_2 can tune the energy levels in the dot. 25

Figure 2.9. A PbTe nanowire quantum dot device. (a) The conceptual diagram of the device. (b) SEM image of the device. The source and drain are Ti/Au contacts. A back-gate is underneath the nanowire and a top-gate is on top of the nanowire. The figure is adapted from [41]. 27

Figure 2.10. Differential conductance of a PbTe nanowire quantum dot device with different combinations of bias voltage V_{bias} and top gate voltage V_g at different magnetic fields B. The back-gate underneath the nanowire is set at -15 V. (a) B = 0 T. (b) B = 0.34 T. (c) B = 2.6 T. (d) B = 4.0 T. The figure is adapted from [41]. 28

Figure 2.11. The circuit diagram of a quantum dot device. 30

Figure 2.12. Schematics of a quantum dot at low bias. (a) There are no energy levels in the dot between the chemical potentials μ_{left} and μ_{right} on the leads. No electrons can transport to the dot. (b) There is an energy level in the dot between the chemical potentials μ_{left} and μ_{right} on the leads. One extra electron can transport from the left lead to the dot and from the dot to the right lead. 32

Figure 2.13. Sample description and conductance spectroscopy of an InSb nanowire quantum dot. This figure and its caption are adapted with permission from [45]. Copyright {2009} American Chemical Society. (a) SEM image of InAs/InSb heterostructure nanowires grown on an InAs(111)B substrate using aerosol gold particles with a diameter of 40 nm as initial seeds. The image is recorded with a 30° tilt of the substrate from the horizontal position and the scale bar is uncompensated

for the tilt. In the heterostructure nanowires, the base segments with a small diameter are InAs, crystallizing in the wurtzite phase, and the upper segments with a large diameter are InSb, crystallizing in the zinc blende phase. Note that the InSb segments do not show any tapering at the sidewalls. (b) TEM image of a top part of an InSb nanowire, after detachment from the growth substrate, with the single crystalline $AuIn_2$ seed particle on top and the pure zinc blende InSb nanowire segment below. This InSb nanowire segment has a diameter of 79 nm. (c) SEM-picture of an InSb quantum dot device. The device is made by electrically contacting the InSb segment of an InAs/InSb heterostructure nanowire on a SiO_2 capped, highly doped Si substrate using electron beam lithography. (d) Differential conductance on a color scale as a function of the source-drain voltage V_{sd} and the back-gate voltage applied to the Si substrate V_{bg} (charge stability diagram), measured for an InSb nanowire quantum dot device with a nanowire diameter of 70 nm and a contact spacing of 70 nm. The conventional spin-1/2 Kondo effect (a Kondo enhanced conductance ridge) at zero bias is observed in the N = 9 Coulomb blockade diamond region. (e) Addition energy versus electron number in the InSb nanowire quantum dot measured in (d) (addition energy spectrum), revealing a typical shell structure of a few-electron quantum dot system. 33

Figure 2.14. Schematics of different reflection mechanisms at the interface of a semiconductor (N) and a superconductor (S). (a) Normal reflection where an electron coming from the N side hits the interface and reflects back. (b) Andreev reflection where an electron coming from the N side hits the interface and reflects as a hole, leaving a pair of electrons into the superconductor. 37

Figure 2.15. Possible energy excitations in a quantum dot coupled with a superconductor. The ground state can be a spin doublet (|D⟩) or a spin singlet (|S⟩). When there is a magnetic field, the spin doublet splits and the excitations are different depending on the ground state. 42

Figure 2.16. Schematic of a quantum dot coupled with a superconductor. μ_N is the chemical potential of a normal (not superconducting) lead connected to the quantum dot and μ_S is the chemical potential of the superconductor. Andreev levels exist due to Andreev reflection and when μ_N is aligned with an Andreev level, electron transport is possible from the normal lead to the superconductor. 43

Figure 2.17. Phase diagram of a quantum dot coupled with superconductors. The transition line is from E_{-}^{0}. The ground state can be singlet or doublet based on this diagram. 46

Figure 3.1. SEM images of InSb nanowires adapted with permission from [67]. Copyright {2012} American Chemical Society. (a) An array of nanowires. The scale bar represents 1 μm. (b) Image of a single nanowire. The scale bar represents 200 nm. The arrow indicates the zone of evaporated InAs stem.......... 50

Figure 3.2. SEM images of nanowires grown with a shadow technique. (a) InSb nanowires are shadowed by nano-flakes during the deposition of Sn. A S-N junction is formed in situ. The figure is adapted from [81]. Reprinted with permission from AAAS. (b) InAs nanowire arrays for a shadow technique. Two nanowires form a cross and therefore, deposition of a superconductor can be shadowed for a proper deposition direction. S-N-S junctions are formed in situ. This figure is adapted with permission from [82]. Copyright {2020} American Chemical Society. 52

Figure 3.3. Schematic of the cross section for two types of global back-gate chip. The figures are not on scale. 55

Figure 3.4. A nanowire placed on a rectangular local back gate. (a) An SEM image of the local back gate. A layer of HfO_x is covered on a layer of Ti/Au. Undoped silicon substrate with a layer of SiO_2 underneath. (b) Schematic of the cross section for the local gate. The figure is not on scale. 55

Figure 3.5. A nanowire placed on more advanced local back gates. There are alternating wide and narrow rectangular fine gates designed on the substrate. 56

Figure 3.6. Schematics of e-beam deposition for a hexagonal nanowire. The arrows indicate the direction of the coming evaporated materials. (a) Common perpendicular deposition. (b) Deposition with an angle other than 90°. 57

Figure 3.7. Deposition of metal onto a nanowire placed on a substrate. The technique of deposition with an angle is applied. The thickness of the metal can be smaller than the thickness of the nanowire by using this technique. 58

Figure 3.8. Schematic of lithography process for deposition materials on selective locations on a substrate. The figures are not on scale. 60

Figure 3.9. Design of gate chips with leads and markers. The upper small picture gives the enlarged format of the small area indicated by an arrow. The lower small picture gives an SEM image of the enlarged area. Leads, large and small markers are also indicated by arrows 62

Figure 3.10. (a) A dilution refrigerator. (b) A probe used to load a chip with devices 65

Figure 3.11. Racks of the measurement system: matrix rack and IVVI rack 66

Figure 3.12. A two-terminal measurement circuit. Voltage V is applied to the device, R_{device}, by a voltage source. An ammeter (I-measure) is connected in series. R_{in} represents the overall input resistance. 69

Figure 3.13. A four-terminal measurement circuit. V is applied to the left section of a nanowire by a voltage source. An ammeter is connected in series. R_{in} represents the overall input resistance. Additionally, a voltmeter is connected across the right section of the nanowire to monitor the corresponding voltage........ 70

Figure 4.1. Hysteresis loop of a ferromagnetic material. h is the applied magnetic field and m_h is the magnetization of the material. The schematic is conceptual and for a real material, the loop may be different. 73

Figure 4.2. Schematic of spin-valve. h is a magnetic field and R is the resistance of the spin-valve device. The arrows indicate the magnetization directions of two ferromagnetic contacts of the device. 75

Figure 4.3. An InSb nanowire with two CoFe contacts fabricated by angle deposition. There are residues of CoFe because during the angle deposition, the InSb nanowire can shadow the deposition........ 77

Figure 4.4. Measurement on a two-terminal device. Vbias is the applied bias voltage. V_g is the applied back-gate voltage. Current is measured through a device. (a) Pinch-off curve of an InSb nanowire device with two ferromagnetic contacts. (b) I-V curve of an InSb nanowire device with two ferromagnetic contacts. 79

Figure 4.5. Measurement on an N-N device. (a) Scanning electron microscope image of a device without any ferromagnetic components. (b) Representative magnetic field scan taken at V_{sd} = 5 mV and V_g = 1 V. V_{sd} is the applied bias voltage and V_g is the applied

back-gate voltage. Data are acquired by DC measurement. There is no observable hysteresis and the signal is peaked at zero field. The peak width is of order 100 mT. This figure is adapted from [104]. 81

Figure 4.6. Measurement on an N-N device. V_{sd} is the applied bias voltage. V_g is the applied back-gate voltage. B is the applied magnetic field. (a) Pinch-off curve. (b) I-V curve. 81

Figure 4.7. (a) Scanning electron microscope (SEM) image of an F-F device. The direction of the applied magnetic field B is indicated by arrow. (b) Schematic of measurement setup. All data shown in this figure are acquired by DC measurement. (c) Current as a function of magnetic field taken at V_{sd} = 0.1 mV and V_g = 0 V. (d) Magnetic field scan taken at V_{sd} = 0.1 mV and V_g = 0.08 V. The sign of the hysteresis is reversed compared to panel (c). This figure is adapted from [104]. 82

Figure 4.8. (a) Scanning electron microscope (SEM) image of a N-F-F-N device. The direction of the applied magnetic field B is indicated by arrow. (b) Schematic of the device. Data shown in this figure are acquired by a lock-in. (c, d) Local and non-local signals from magnetic field scan taken at 0.1 mV AC voltage bias, zero DC voltage bias and V_g = 1.2 V in configuration 1. (e, f) Local and non-local signals from magnetic field scan in configuration 2 taken at 0.1 mV AC voltage bias, 1 mV DC voltage bias and V_g = 1.35 V. For (c) and (e), the resistance of the measurement circuit is not subtracted (around 4.5 kΩ). For (d) and (f), the voltage is the AC voltage measured by lock-in. This figure is adapted from [104]. 84

Figure 4.9. Additional data from N-F-F-N device. Magnetic field scan measured from the device shown in Figure 4.8 (a). Voltage is applied across contacts 1 and 3. Non-local

signal is the voltage across contacts 2 and 4. (a,b) Local and non-local magneto-conductance measured at 0.1 mV AC bias and 1.2 V gate voltage. (c,d) Local and non-local magneto-conductance measured at the same bias and gate setting as in (a,b), but at a different time. (e,f) Local and non-local magneto-conductance measured at 0.1 mV AC bias and 2.85 V gate voltage. This figure is adapted from [104].................. 86

Figure 4.10. More data from N-F-F-N device shown in Figure 4.8 (a). Voltage is applied across contacts 2 and 4. Non-local signal is the voltage across contacts 1 and 3. (a,b) Local and non-local magneto-conductance measured at 1mV DC bias, 0.1 mV AC bias and 1.35 V gate voltage. (c,d) Local and non-local magneto-conductance measured at 1mV DC bias, 0.1 mV AC bias and 1.5 V gate voltage. (e,f) Local and non-local magneto-conductance measured at 1mV DC bias, 0.1 mV AV bias and 2.7 V gate voltage. This figure is adapted from [104]. 87

Figure 4.11. (a) Scanning electron microscope image of a N-(F,F)-N device. The two CoFe strips are insulated from the nanowire by native oxide. The direction of the external magnetic field *B* is indicated by arrow. (b) Schematic of measurement setup. (c) Current as function of external magnetic field using the source-drain bias voltage V_{sd} = 2 mV and gate voltage V_g = 1.05 V. Directions of magnetic field sweeps are indicated by arrows. (d) Magnetic field scan taken at V_{sd} = 2 mV and V_g = 1.1 V. This figure is adapted from [104]... 89

Figure 4.12. Additional magnetic field scans measured in the N-(F,F)-N device shown in Figure 4.11. We observe that the response can be modulated by gate voltage and bias voltage. Current vs. magnetic field measured at different gate and bias settings. Data

are acquired by DC measurement. (a-c) at V_g = 1.1 V. (d-e) at V_{sd} = 5 mV. This figure is adapted from [104]. 91

Figure 4.13. Measurements in a finite B_x. (a) SEM image of the device also shown in Figure 4.11 with field directions indicated. (b-c) B_y magnetic field scan with B_x = -0.2 T and B_x = 0.2 T respectively. Data are acquired by DC measurement. Both plots are measured at V_{sd} = 2 mV and V_g = 1.05 V. Magnetoresistance is not symmetric, but hysteresis is observable. (d) B_y magnetic field scan with B_x = -1 T. The measurement is performed at V_{sd} = 2 mV and V_g = 1 V. At this large B_x field, there is no observable hysteresis as the magnetization of CoFe strips is pinned by B_x. Measurements are performed using a 2D vector magnet with sample plane aligned with magnetic field plane. This figure is adapted from [104]. 92

Figure 4.14. (a) The numerical simulation geometry and the coordinate system. The origin of the coordinates is located at the center of the nanowire segment. u axis is along the nanowire. The angle θ between x and u is 20º. (b) Average normalized magnetization in y direction of the two strips. (c) The stray field in the nanowire for parallel up magnetization (achieved when $B_{ext,y}$ = 75 mT) as function of u. This figure is adapted from [104]. 94

Figure 4.15. The averaged stray field in the nanowire for anti-parallel up-down magnetization ($B_{ext,y}$ = -50 mT) as function of the nanowire coordinate u. This figure is adapted from [104]. 95

Figure 4.16. The averaged stray field calculated in the nanowire for parallel down magnetization ($B_{ext,y}$ = -75 mT) as function of the nanowire coordinate u. This figure is adapted from [104]. 96

Figure 4.17. The averaged stray field in the nanowire for anti-parallel down-up magnetization ($B_{ext,y}$ = 50 mT) as function of the nanowire coordinate u. This figure is adapted from [104].. 96

Figure 5.1. A heat map for magnetic field magnitude for a micromagnet of dimensions 230 × 1000 × 100 nm. This is shown for a 2D X-Y plane slice through the middle of the micromagnet (50 nm), the magnet is shown as grey. Note the field is very weak away from the micromagnet ends. 100

Figure 5.2. A X-Y plane heat map for magnetic field magnitude in a small region near the nanowire, the magnet areas have been set to 0 field (black triangular regions). This is for a 5 nm thick slice in the middle where the nanowire is (marked by red lines). 100

Figure 5.3. A simple configuration that generates magnetic field along a nanowire. Magnetization directions are represented by arrows. 101

Figure 5.4. The Dragonfly setup with four micromagnets (blue/red) and an overlay of the magnetic field calculated with MuMax3 (gray arrows). The nanowire runs horizontally with the spin-orbit axis vertical, indicated by B_{so}. 102

Figure 5.5. Magnetic field profile, as a function of position, of the four magnet Dragonfly setup. Solid line is field amplitude and dashed line is field angle θ relative to negative x-axis (inset). The field is averaged over a hexagonal cross-section of the nanowire with a characteristic dimension of 100 nm. In this figure only, the reader is invited to imagine an infinitely long nanowire without ends and consider what field profile would be created along such a nanowire. The horizontal dashed gray line indicates a uniform field for entering the topological regime in an infinite nanowire. 103

Figure 5.6. This compares the rotated and un-rotated Dragonfly configuration. The solid line is the rotated set-up and the dashed line is the straight set-up. Rotating the magnets makes them easier to magnetize through hysteresis. This figure is for a 1000 nm nanowire segment.. 104

Figure 5.7. Shows the magnetic field magnitude's standard deviation (dashed) across the hexagonal cross-section and mean value over the nanowire region for the single Dragonfly set-up. The insets are field magnitude cross sections of the nanowire at different positions.. 105

Figure 5.8. (a) Probability distributions for two Majorana wavefunctions γ_1 and γ_2. The first excited state (dashed line) is a bulk nanowire state. (b) Magnetic field profile reproduced from Figure 5.5 over a smaller range. Hard boundaries are introduced at ±350 nm to calculate the wavefunctions. There is no applied external field. 105

Figure 5.9. (a) Probability distributions for two lowest energy states, this system shows two overlapping and degenerate states with no clear Majorana polarization and no higher energy state being gapped out. The energies of both states $E_1/\Delta = 3.9 \times 10^{-2}$ and $E_2/\Delta = 4.6 \times 10^{-2}$. (b) Field profile along wire. External field is 40 mT in positive y-direction. 107

Figure 5.10. The double Dragonfly setup with the magnet in the middle and a potential gate, dimensions given. Toggling this gate allows the left and right side of the wire to be coupled or uncoupled.. 107

Figure 5.11. (a) Probability distributions of two lowest energy states for double Dragonfly setup with gate open (shown in inset). MZM (red/blue) with $E_0/\Delta = 5.1 \times 10^{-4}$. The first excited state (grey dashed) with $E_1/\Delta = 1.6 \times 10^{-1}$. External field of 40 mT is

applied in positive y-direction. Inset: two dragonfly configurations, with zigzag indicating an electrostatic gate capable of dividing the nanowire in two parts. (b) Magnetic field profile along the wire, showing amplitude (solid) and angle (dashed). 108

Figure 5.12. Comparing the double Dragonfly with different external fields. (a) 40 mT in the positive y direction (b) no field and (c) 40 mT in the positive x direction. 109

Figure 5.13. (a) Probability distributions for two lowest energy states for double Dragonfly setup with the central vertical magnet and the gate closed (inset). The probability distributions shows two separate pairs of MZMs in each section of the wire, the left is shown in the Majorana basis with energy $E_1/\Delta = 3.1 \times 10^{-2}$ (red and cyan), the other pair in the right section is in the electronic state basis with energy $E_2/\Delta = 3.1 \times 10^{-2}$ (black- dashed line). The third state is well separated at $E_3/\Delta = 8.9 \times 10^{-1}$. (b) Field profile along wire. External field is 40 mT in positive y-direction. 110

Figure 5.14. B_z field component along the wire for the double Dragonfly with the middle vertical magnet. 111

Figure 5.15. T-Junction setup. The top two sections of nanowire are 5000 nm in length in total and the perpendicular section is 1100 nm. Zigzag lines indicate electrostatic gates. Circles indicate desired positions of 6 MBSs with all gates on...................... 112

Figure 5.16. Probability distributions (color) of the ground, second and third lowest energy with (a) all gates (b) gate G_3, (b) gate G_1, (c) gate G_2 activated. Colors chosen so that red wavefunction always has a weight on the left end. 114

Figure 5.17. (a) Magnetic field of top wire for T-Junction. (b) Magnetic field in the T-Junction leg (vertical segment of nanowire). There is an external field of 40 mT applied in positive y-direction. 115

Figure 5.18. (a) Atomic force microscopy (AFM) of a T-junction setup with three Dragonfly magnet configurations. Magnetic film thickness is 20 nm. (b) Magnetic force microscopy (MFM) data on a different T-Junction of the same design. Arrows indicate magnetization direction; white dashed lines are example of magnet dimensions. Blue dashed line is where the Majorana nanowire is envisioned. The magnetic history was a magnetizing field from 100 mT to -16 mT to 0 mT applied at 45-degree direction, then 100 mT to -16 mT to 0 mT at 135 degrees. 116

Figure 5.19. Magnetic force microscopy (MFM) data on 24 T-junction setups using three Dragonfly's. The magnet dimensions are the same as in Figure 5.4 but the distance between them differs. Top left: Atomic force microscopy (AFM) of one T-junction setup with three dragonfly magnet configurations. Magnetic film height 20 nm. Dashed ovals point out magnetizations favorable for generating MZM. The magnetic history was a magnetizing field from 100 mT to -16 mT to 0 mT applied at 45-degree direction, then 100 mT to -16 mT to 0 mT at 135 degrees. 118

Figure 6.1. (a) Schematic of an InSb S-N-S junction device. (b) A SEM image of an InSb S-N-S device, SNS_1. A back gate is underneath. 121

Figure 6.2. Scans of bias voltage (V) vs. gate voltage (V_g). (a) Measured in device SNS_1. (b) Measured in device SNS_2. 122

Figure 6.3. Schematic of an InSb S-N-S junction device with a CoFe strip. Stray field from a magnetized CoFe may penetrate the nanowire device, as indicated by arrows. 123

Figure 6.4. An InSb nanowire device (device SNS_3) with two S-N-S junctions. (a) A SEM image of device SNS_3. The direction of the applied magnetic field is given by the arrow. (b) Top-view schematic of device SNS_3. (c) Cross-section of the double S-N-S junctions.. 124

Figure 6.5. 2D plot of injected current (*I*) with respect of gate voltage (V_g) in device SNS_3. Resistance is acquired by taking differential of measured voltage and extracting input resistance. The switching current is indicated by arrows. 125

Figure 6.6. 2D plots of injected current (*I*) with respect to magnetic field (B_y) in device SNS_3. V_g = 3 V. (a) B_y is swept from -0.2 T to 0.2 T. (b) B_y is swept from 0.2 T to -0.2 T. 126

Figure 6.7. 2D plots of injected current (*I*) with respect to magnetic field (B_x) in device SNS_3. V_g = 3 V. (a) B_x is swept from -0.2 T to 0.2 T. (b) B_x is swept from 0.2 T to -0.2 T. 127

Figure 6.8. An InAs nanowire device (device SN_1) with one S-N junction and two CoFe strips. (a) A SEM image of device SN_1. The upper CoFe strip is also used as a side gate (V_{sg}). (b) Top-view schematic of device SN_1. (c) Cross-section of the S-N junction. 129

Figure 6.9. 2D plots of voltage bias (*V*) with respect of side-gate voltage (V_{sg}) in device SN_1. Conductance is acquired by taking differential of measured current. The CoFe strips are pre-magnetized by applying a -0.2 T magnetic field B_θ where $\theta = 44^o$. After pre-magnetization, the external magnetic field is swept back to zero for taking the data. (a) V_g = 9 V. Weak-coupled case. (b) V_g = 9.75 V. Between weak-coupled and strong-coupled. (c) V_g = 9 V. Strong-coupled case. 130

Figure 6.10. ZBP and hysteresis under magnetic field scans. V_g = 10.5 V (a) 2D plots of voltage bias (*V*) with respect of side-gate voltage (V_{sg}) in device SN_1. Conductance is

acquired by taking differential of measured current. The CoFe strips are pre-magnetized by applying a -0.1 T magnetic field B_θ where θ = 90°. After pre-magnetization, the external magnetic field is swept back to zero for taking the data. (b, c) 2D plots of voltage bias (V) with respect of the external magnetic field, B_θ (θ = 90°) in device SN_1. Sweeping direction of magnetic field is given by arrows........ 132

Figure 6.11. ZBP and hysteresis under magnetic field scans. V_g = 10.5 V (a) 2D plots of voltage bias (V) with respect of side-gate voltage (V_{sg}) in device SN_1. Conductance is acquired by taking differential of measured current. The CoFe strips are pre-magnetized by applying a -0.1 T magnetic field B_θ where θ = 90°. After pre-magnetization, the external magnetic field is swept back to zero for taking the data. (b, c) 2D plots of voltage bias (V) with respect of the external magnetic field, B_θ (θ = 90°) in device SN_1. Sweeping direction of the magnetic field is given by arrows. 133

Figure 6.12. 2D plots of voltage bias (V) with respect of side-gate voltage (V_{sg}) in device SN_1 at different magnetic fields. Conductance is acquired by taking differential of measured current. The CoFe strips are pre-magnetized by applying a -0.1 T magnetic field B_θ where θ = 90°. After pre-magnetization, the external magnetic field is swept back to zero before taking any new data. V_g = 10.5 V. (a). B_θ = 0 mT. (b) Data acquired by adding a magnetic field that B_θ = 50 mT, θ = 90°. (c) Data acquired by adding a magnetic field that B_θ = -50 mT, θ = 90°. 134

Figure 6.13. (a) SEM image of device SN_2, an InAs nanowire device. This device has an S-N junction and two CoFe strips close to the junction. The two CoFe strips also work as two side gates (V_{sg1} and V_{sg2}). (b) A scan of Vbias (V) vs. side-gate voltage (V_{sg1}) measured on device SN_2. The back-gate voltage is 8.25 V and the second side gate

voltage (V_{sg2}) is 0 V. The CoFe strips are magnetized in the direction of θ = 180° and the external magnetic field is 0 T. (c, d) Scans of Vbias vs. magnetic field. The angle of the magnetic field is labeled on the plots. The back-gate voltage is 8.25 V and both side gate voltages are 0 V. Sweeping directions of the magnetic field are given by arrows. (e) Scans of Vbias vs. magnetic field. The angle of the magnetic field is labeled on the plots. The CoFe strips are magnetized in the direction of θ = 180°. The back-gate voltage is 8.25 V and side gate voltages are 0 V. Sweeping direction of the magnetic field is given by an arrow. (f) Scans of Vbias vs. magnetic field at different angles. The magnitude of the external magnetic field is 0.04 T. The back-gate voltage is 8.25 V and both side-gate voltages are 0 V. Sweeping direction of the magnetic field is given by an arrow. 136

Figure 6.14. (a) A scan of V_{bias} (V) vs. side gate voltage (V_{sg1}) measured on device SN_2. The back-gate voltage is 6.075 V and the second side gate voltage (V_{sg2}) is 0 V. The CoFe strips are magnetized in the direction of θ = 180° and the external magnetic field is 0 T. (b) Line-cut of the differential conductance peak along the first side gate voltage (V_{sg1}) in plot (a). 138

Figure 6.15. Scans of V_{bias} (V) vs. side gate voltage (V_{sg1}) measured on device SN_2. Vg = 7.5 V. Data are taken at zero external magnetic field. The CoFe strips are magnetized using the pre-magnetization process for Figure 6.13 (a). (a) Induced superconducting gap. (b) The plot uses the same data set as in (a). Offset from measurement setup and data at larger bias are not extracted. 140

Figure 6.16. 2D plots of voltage bias (V) with respect to the external magnetic field, B_θ (θ = 113°) in device SN_2. Sweeping directions of the magnetic field are given by arrows.

V_g = 6.075 V. V_{sg1} = -0.56 V. V_{sg2} = 0 V. (a) No charge jump. (b) There is a charge jump (indicated by the small arrow) which changes the original state............................. 141

Figure 6.17. Scans of V_{bias} (V) vs. side gate voltage (V_{sg1}) measured on device SN_2. V_g = 6.45 V. V_{sg2} = 0 V. Data are taken at zero external magnetic field. The CoFe strips are magnetized using the pre-magnetization process described for Figure 6.13 (b)..... 142

Figure 6.18. Scans of V_{bias} (V) vs. side gate voltage (V_{sg1}) measured on device SN_2. V_g = 6.075 V. V_{sg2} = 0 V. Data are taken at zero external magnetic field. The CoFe strips are magnetized using the pre-magnetization process described for Figure 6.13 (b)..... 142

Acknowledgment

This dissertation is dedicated to my parents and home country.

I also would like to sincerely thank my supervisor, Prof. Sergey Frolov, and all other people who helped me during my PhD journey.

1.0 Introduction

My graduate research mainly focuses on quantum transport measurements of hybrid devices based on semiconductor nanowires. Typical devices compose a semiconductor nanowire and superconductor contacts or ferromagnetic components. These kinds of hybrid devices are platforms for interesting physics and have possible applications for industry.

1.1 Majorana Bound States and Semiconductor Nanowire Devices

Majorana bound state (MBS) is a popular topic in condensed matter physics. It is believed that this topological state can be used for topologically protected quantum computation, which may be beneficial for problems that classical computers have difficulties to solve [1, 2]. In condensed matter physics, we typically consider electrons in solid materials. Unlike a single free electron in vacuum, electrons in a solid material may pose different properties depending on the properties of the material. Kitaev [3] proposed a simple model that is composed of a chain of sites available for electrons and with proximity of a p-wave superconductor. It is shown that two "Majorana Fermions" may exist at the two ends of the chain. Even though these "Majorana Fermions" are not the particles expected to be found in particle physics, we still call them "Majorana Fermions" or maybe better, MBSs in condensed matter physics. These quasi particles are thought to be topological states and non-Abelian anyons which are candidates of fault-tolerant quantum computation. This makes this model not only physically interesting, but also valuable for industrial applications. Inspired by Kitaev's idea, efforts are dedicated to find feasible approaches

to realize MBSs. It is predicted that a quantum wire with spin-orbit coupling, Zeeman field and conventional s-wave superconductor proximity may be a realizable platform for MBSs [4, 5]. Experimentally, this approach can be realized by a hybrid device composed of a semiconductor nanowire with strong spin-orbit interaction, superconductor proximity and magnetic fields. Quantum transport measurements on this semiconductor nanowire device are performed to detect MBSs. Indeed, experimental results on these transport measurements were reported and signatures of MBSs [6-10] are claimed to be observed. In these experiments, the typical devices are based on semiconductor nanowires with strong spin-orbit interaction (InAs or InSb nanowires). Conventional superconductors are deposited on the nanowires and form superconductor-semiconductor junctions (S-N junctions). Transport measurements show zero-bias peaks (ZPBs) on differential conductance and this ZPB is considered as the signature of MBSs. Even though some numerical simulations of the devices are also included to support the ZBP signature's agreement with theoretical predictions of MBSs, reasons other than MBSs still exist, which poses questions on the discovery of these topological states. For example, a topologically trivial state, called Andreev bound state (ABS), commonly exits in a semiconductor with superconducting proximity and shares similar features with MBSs, including ZBPs. Even though ZPBs are theoretically necessary observations for MBSs in the semiconductor nanowire platforms, ZBPs themselves cannot confirm the existence of MBS [11-14].

1.2 Semiconductor Nanowire Devices with Ferromagnetic Components

Ferromagnetic materials are commonly known as magnets that produce magnetic fields. A familiar example of ferromagnetic materials is refrigerator magnets that can be "pasted" on fridges.

In condensed matter physics, ferromagnetic materials may be integrated with other materials to produce interesting properties. For semiconductor nanowire devices, ferromagnetic materials are also useful. When ferromagnetic contacts are formed to a nanowire, spin-polarized currents may be injected into the nanowire [15-19]. We may study spin transport or spintronics using this platform. We also consider applications of ferromagnetic components on MBS devices. In MBS experiments, instead of applying magnetic fields externally (for example, using a superconducting coil), ferromagnetic components may be used. One of the ideas is to deposit a layer of ferromagnetic insulator onto a semiconductor nanowire. The exchange fields from the ferromagnetic insulator may be used instead of the external magnetic fields [20-23]. MBSs may appear at zero or low magnetic field. This is beneficial since strong magnetic fields may destroy superconductivity. Another idea is to use the stray fields produced by ferromagnetic components [24, 25]. Ferromagnetic components are used as micromagnets which are sources of magnetic fields. By utilizing micromagnets, we may apply inhomogeneous local magnetic field profiles which may allow more freedom to design MBS device and manipulate the MBSs. This stray field idea will be an important topic in this thesis. More details about this idea will be discussed in chapter 5 and 6.

1.3 Other Majorana Fermions and Motivations

The use of the term “Majorana Fermions” is not limited to the case of the bound states that exist in the nanowire model. In condensed matter physics, there are other topological states predicted in other platforms and some of these states are also referred to as “Majorana Fermions” or Majorana zero modes (MZMs). For example, Majorana Fermions may exist at the surface of a

topological insulator [26] or a quantum anomalous Hall insulator [27, 28]. The original term of Majorana Fermion is used in particle physics [29]. In short, it is a particle that is its own antiparticle. This is an interesting physical property to be discovered experimentally. The study of particle physics and the study of condensed matter physics can be quite different. It may be believed that the condensed matter Majorana and the particle physics Majorana are essentially the same concept. Though, readers of this thesis may be careful based on their different academic backgrounds.

Besides the interesting physical properties, an important motivation to study MBSs in condensed matter physics is their possible application for quantum computing. Quantum computing is based on quantum states. A major problem of the current developments of quantum computing is that the quantum states are very fragile. However, MBSs are believed to be topological states, which are much less fragile and more robust. A quantum computer based on MBSs may be fault-tolerant at the physical level so that quantum error-correction codes are not necessary.

1.4 Thesis Outline

Chapter 2 of this thesis introduces the theory for MBSs in condensed matter physics. Other topics including superconducting proximity, quantum dots and ABS are also discussed since they are essential parts of MBS devices.

Chapter 3 introduces the device fabrication and experiment method.

Chapter 4 presents a stray field effect from micromagnets on simple semiconductor nanowire devices.

Chapter 5 discusses how ferromagnetic components may be used to search for MBSs.

Chapter 6 presents hysteretic supercurrents in nanowire superconductor-semiconductor-superconductor (S-N-S) devices and ZBPs at zero external magnetic field in nanowire superconductor-semiconductor devices.

Chapter 7 is a summary of this thesis and gives my outlook.

2.0 Basic Theory

In general, my work is experimental condensed matter physics, and the main purpose of this thesis is to discuss related experiments. However, it is helpful for readers to have knowledge of some basic theories about my research topic. In this chapter, we will introduce some basic theoretical backgrounds which may be useful to understand my research motivations and data from experiments.

2.1 Majorana Bound States and Kitaev Chain

Kitaev chain is a model that allows existence of MBSs [3] and becomes a concept which is popularly introduced for the basic theories about MBSs in condensed matter physics. It is a toy model that is simple but unrealistic experimentally within my knowledge. Nevertheless, many more realistic theories and proposals of MBSs are more or less inspired by this toy model. The Kitaev chain is a good first reference for readers who have interest in MBS theories and related numerical calculations.

2.1.1 A Chain of Sites and Majorana Operators

The Kitaev chain can be thought of as a chain on the surface of a three-dimensional (3D) superconductor [3]. We first imagine a 3D superconductor. At a surface of this superconductor, there is a piece of one-dimensional (1D) quantum wire, as shown in Figure 2.1. This 1D quantum

wire is a chain of sites that can be empty or occupied by an electron. Using a circle to represent each site and for a chain with $L >> 1$ sites, the chain is shown as the diagram of Figure 2.2 (a). For this chain, electrons from one site may tunnel to its neighboring sites. This means that there are terms describing the tunneling appearing in the Hamiltonian of these sites. Additionally, the common terms from chemical potential should exist. Since this chain is on the superconductor, there should be terms describing the superconductivity. The important point is that the superconductor has a superconducting gap such that a term in the Hamiltonian should be a term related to this gap. Electrons have spins and their states can be spin-up or spin-down. However, for this toy model, the electrons are considered as spinless, or all electrons have the same spin direction and will not flip spins. Giving these considerations, the Hamiltonian of this quantum wire may have the following format:

$$H = \sum_j \left[-w\left(a_j^\dagger a_{j+1} + a_{j+1}^\dagger a_j\right) - \mu\left(a_j^\dagger a_j - \frac{1}{2}\right) + \Delta a_j a_{j+1} \right. \\ \left. + \Delta^* a_{j+1}^\dagger a_j^\dagger \right] \tag{2.1}$$

Here w is the hopping or tunneling amplitude, μ is the chemical potential, and Δ is the superconducting gap. The superconducting gap can have a phase term such that $\Delta = |\Delta/e^{i\theta}$.

The Hamiltonian in equation (2.1) uses site a_j as the fermionic operator to construct different terms and there are no observable MBSs appearing in this expression. However, by introducing Majorana operators, the hidden MBSs in the original Hamiltonian will appear. Without losing generality, the phase term of the superconducting gap can also be hidden by defining the Majorana operators. The Majorana operators are constructed by combination of fermionic creation and annihilation operators $a_j^\dagger$ and a_j as follows:

$$c_{2j-1} = e^{i\frac{\theta}{2}}a_j + e^{-i\frac{\theta}{2}}a_j^\dagger, \qquad c_{2j} = -ie^{i\frac{\theta}{2}}a_j + ie^{-i\frac{\theta}{2}}a_j^\dagger, \qquad j = 1, \dots, L \tag{2.2}$$

Since fermionic creation and annihilation operators anti-commute, it is clear that:

$$a_j = \frac{c_{2j-1} + ic_{2j}}{2}e^{-i\frac{\theta}{2}}, \qquad a_j^\dagger = \frac{c_{2j-1} - ic_{2j}}{2}e^{i\frac{\theta}{2}} \tag{2.3}$$

$$c_j^\dagger = c_j \tag{2.4}$$

The conjugate of the Majorana operator c_j or $c_j^\dagger$ is just itself. This satisfies the requirement that a Majorana fermion is its own antiparticle.

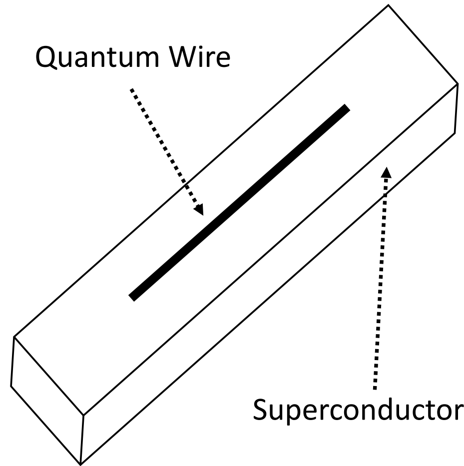

Figure 2.1. A quantum wire on a superconductor's surface

2.1.2 Majorana Bound States in the Kitaev Chain Model

With the Majorana operators shown in equation (2.2), the Hamiltonian representing the quantum wire in equation (2.1) can be transformed to the new format:

$$H = \frac{i}{2}\sum_j \left[-\mu c_{2j-1}c_{2j} + (w + |\Delta|)c_{2j}c_{2j+1} + (-w + |\Delta|)c_{2j-1}c_{2j+2}\right] \quad \textbf{(2.5)}$$

It is not straightforward to diagonalize this new Hamiltonian compared to some simple Hamiltonians, for example, a simple harmonic oscillator. However, by considering a couple of special cases, we may easily observe one trivial and one topological case from the Hamiltonian.

For the first case, where the chemical potential dominates the Hamiltonian in equation (2.5), the terms with hopping and induced superconducting gap can be neglected. We set $w = |\Delta| = 0$ and $\mu < 0$. The Hamiltonian in equation (2.5) therefore has the simple form:

$$H = -\frac{i}{2}\mu \sum_j c_{2j-1}c_{2j} = -\mu \sum_j \left(a_j^\dagger a_j - \frac{1}{2}\right) \quad \textbf{(2.6)}$$

This Hamiltonian can be easily understood with the help of Figure 2.2 (b), where the diagram shows that the two Majorana operators in one specific site are paired. This is also the common case of a chain of sites without superconducting proximity and this is a trivial case.

We now consider the case that the hopping and superconducting terms dominate, and the chemical potential is neglectable. This gives the condition that $w = |\Delta| > 0$ and $\mu = 0$. This reduces the Hamiltonian to:

$$H = i|\Delta| \sum_{j} c_{2j} c_{2j+1} \qquad \textbf{(2.7)}$$

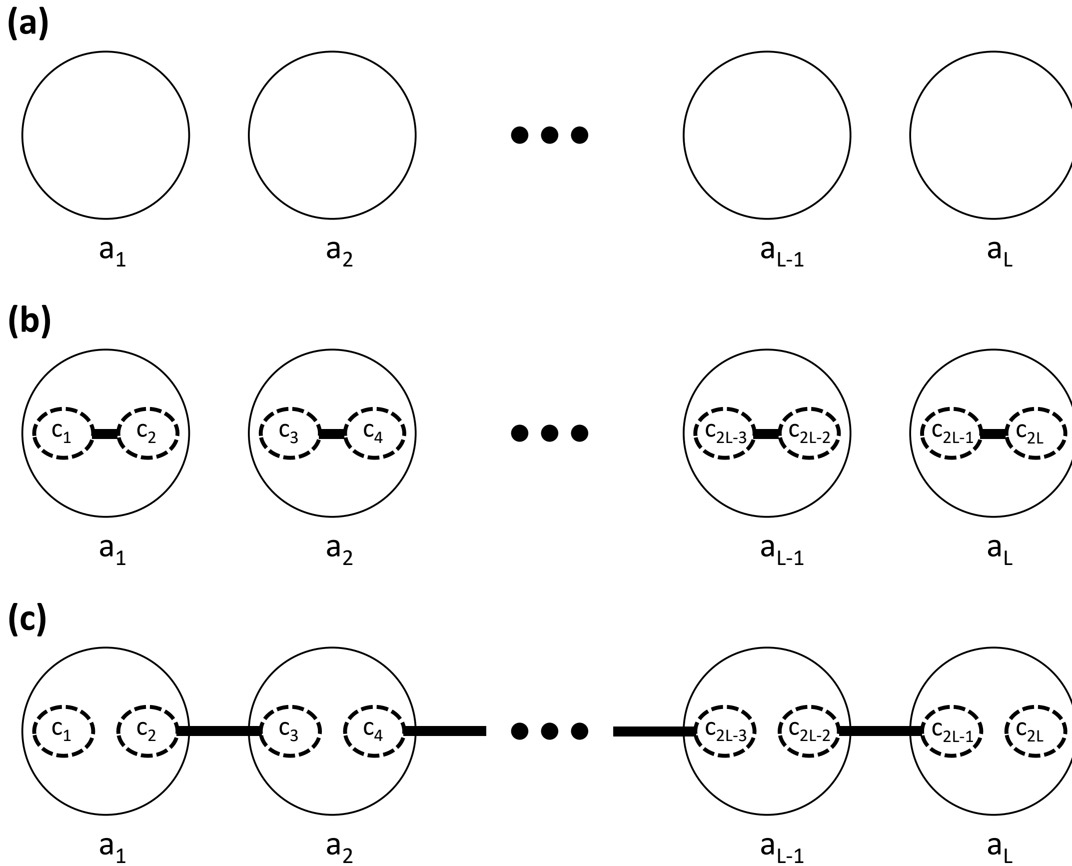

Figure 2.2. Diagrams of Kitaev chain model and different types of pairing. Figure 2.1 (a) shows a chain of sites. Figure 2.1 (b) shows the trivial case. Figure 2.1 (c) shows the topological case.

The Hamiltonian in equation (2.7) is a sum of pairs of neighboring Majorana operators located at different sites. Additionally, the Majorana operators c_1 and c_{2L} do not appear in the

Hamiltonian. These two Majorana operators can be considered as the two ends of this quantum wire as shown in Figure 2.2 (c). To make the Hamiltonian even better, we can define annihilation and creation operators composed of Majorana operators:

$$\tilde{a}_j = \frac{1}{2}\left(c_{2j} + ic_{2j+1}\right), \qquad \tilde{a}_j^{\dagger} = \frac{1}{2}\left(c_{2j} - ic_{2j+1}\right) \tag{2.8}$$

and the Hamiltonian becomes

$$H = 2|\Delta| \sum_{j}^{L-1} \left(\tilde{a}_j^{\dagger}\tilde{a}_j - \frac{1}{2}\right) \tag{2.9}$$

The operator pair has a similar format to a number operator in a simple harmonic oscillator's Hamiltonian and equation (2.9) has a diagonalized format. Since the two ends of the chain do not appear in the Hamiltonian of equation (2.7), it takes zero energy to occupy the state. If the two Majorana sites are not occupied, this gives an ordinary ground state. For a state where the two Majorana sites are occupied, the energy is the same as the ordinary ground state since this is a zero-energy state. Thus, two unpaired Majorana operators result in a two-fold degenerate ground state corresponding to occupied or not occupied state. The unpaired Majorana operators give MBSs or two Majorana zero modes available in this toy model. The two-fold degeneracy makes MBSs candidates as a qubit, but we need four MZMs from two wires to realize a qubit because coherent superposition cannot be formed based on two MZMs [2].

The paired Majorana operators result in a bulk energy gap to the unpaired MBSs. Even though we divide each site into a pair of quasi particles, we cannot divide one electron into two "half electrons" by simply rearranging Hamiltonians in the real world. Nevertheless, the paired

operators protect the unpaired states because to destroy the zero energy states, the two MZMs need to be coupled but the paired sites separate the two modes, and this coupling is forbidden unless the bulk energy gap from the paired sites is closed. This is a bulk-edge correspondence, and we call this kind of protection topological protection. The robustness from topological protection makes MBSs in a quantum wire candidates for topologically protected quantum computation.

2.1.3 Bulk-edge Correspondence

The above discussions mention that there is correspondence between the bulk and edge of the Kitaev chain. Here the bulk is the paired chain, and the edge is the unpaired two quasiparticles at the two ends of the chain. Topological properties are implicated by this correspondence.

To have a better understanding of the bulk-edge correspondence, it is helpful to have some knowledge of the energy spectrum of the Hamiltonian. To have some quantitative information, we consider a new model. This new model is achieved by making a small adjustment of the original chain model. We connect the first site with the last site of the chain and the Kitaev chain now becomes a “Kitaev ring” [30]. By this adjustment, it is possible to apply periodic boundary conditions since there is a translational symmetry along a circle. This condition is similar to that of dealing with a crystal. Enlightened by this, we first transform the fermionic operators to momentum space. This is a Fourier transform with the following format:

$$a_k = \frac{1}{\sqrt{N}} \sum_{n=1}^{N} e^{-ikn}\, a_n \quad \textbf{(2.10)}$$

$$a_k^\dagger = \frac{1}{\sqrt{N}} \sum_{n=1}^{N} e^{ikn} a_n^\dagger \tag{2.11}$$

The Hamiltonian is required by adding the following terms to meet the periodic boundary conditions:

$$-w\left[a_L^\dagger a_{L+1} + a_{L+1}^\dagger a_L\right] + \Delta a_L a_{L+1} + \Delta^* a_{L+1}^\dagger a_L^\dagger \tag{2.12}$$

The site 1 and the site L+1 correspond to the same site based on the periodic boundary conditions. The wave vector can be constructed from the fermionic operators in momentum space:

$$\psi_k = \begin{pmatrix} a_k \\ a_{-k}^\dagger \end{pmatrix} \tag{2.13}$$

With these preparations, we may realize that it is preferable to re-write the Hamiltonian using the Bogoliubov-de Gennes (BdG) formalism. This formalism indeed gives a neat expression of the Hamiltonian:

$$H = \frac{1}{2} \sum_k \psi_k^\dagger H_{BdG}\, \psi_k + \frac{1}{2} \sum_k (-2w\cos k) \tag{2.14}$$

The BdG Hamiltonian is:

$$H_{BdG} = (-\mu - 2w\cos k)\tau_z - 2\Delta\tau_y \sin k \quad \textbf{(2.15)}$$

τ_y and τ_z are the Pauli matrices:

$$\tau_y = \begin{pmatrix} 0 & -i \\ i & 0 \end{pmatrix}, \qquad \tau_z = \begin{pmatrix} 1 & 0 \\ 0 & -1 \end{pmatrix} \quad \textbf{(2.16)}$$

The calculation is not very straightforward, and more details are given in references [31] and [30]. The energy spectrum can be easily calculated by diagonalization of the 2 × 2 matrix H_{BdG}. It is given by:

$$E_{k,\pm} = \pm\sqrt{(\mu + 2w\cos k)^2 + 4\Delta^2 \sin^2 k} \quad \textbf{(2.17)}$$

To have a direct understanding of this energy spectrum, the plots of the energies are given in Figure 2.3 and Figure 2.4. The energy spectrum gives the band structure of the “Kitaev ring”. We first consider the case that the induced superconducting gap is the same as the hopping amplitude. This means $\Delta = w$. By adjusting the chemical potential, it is possible to observe a topological transition from the band structure. In Figure 2.3 (a), the chemical potential is set at -2.5w. There is an energy gap between the two energy bands. When the chemical potential is increased to -2w, the energy gap is closed at $k = 0$ (Figure 2.3 (b)). If the chemical potential is increased to -1w, the two energy bands again split away, and the energy gap re-appears (Figure 2.3 (c)). Figure 2.3 (a) to Figure 3 (c) shows a progress that an energy gap exists, closes and then re-opens. For such progress, the

Hamiltonian cannot always be transformed continually. The discontinuity appears when the chemical potential gets just larger than -2w. When the transformation is not continuous, we say that there is a topological phase transition. Figure 2.3 (d) to Figure 2.3 (f) gives another example of the topological phase transition by increasing the chemical potential. By examining the topological case of the chain model, the ring should be topological at zero chemical potential. Therefore, this ring model is topological for $-2w < \mu < 2w$.

For a case of a smaller induced superconducting gap, similar plots are presented in Figure 2.4 where Δ is 0.2w. We observe that at $\mu = \pm 0.2w$, the energy gap at $k = 0$ or $k = \pm \pi$ closes, indicating the following topological phase transitions. The topological phase appears when the value of the chemical potential is between these two critical potions ($-2w < \mu < 2w$).

By calculating the energy spectrum and tracing the energy gap with different chemical potentials, we observe topological phase transitions in the Kitaev ring model. We can infer if there is a topological phase by studying the bulk energy gap. The topological quasiparticles are located at the edges but the existence of them is related to the bulk energy gap. When the system is in a topological phase, if the related bulk energy gap is finite, the topological state will stay.

Mathematically, a topological phase transition can be characterized by topological invariants. If two Hamiltonians have different topological invariants, they cannot transfer to each other continuously. A discontinuous transformation between two Hamiltonians indicates a topological phase transition. The closing and re-opening of energy gaps discussed in the above examples in fact correspond to change of topological invariants. For a specific Hamiltonian, the corresponding topological invariant will not change due to local perturbations. This is the topological protection. A detailed instruction of topological invariants is out of the scope of this

thesis. For readers who are interested in more details about the corresponding topological invariants, see these references [32-34].

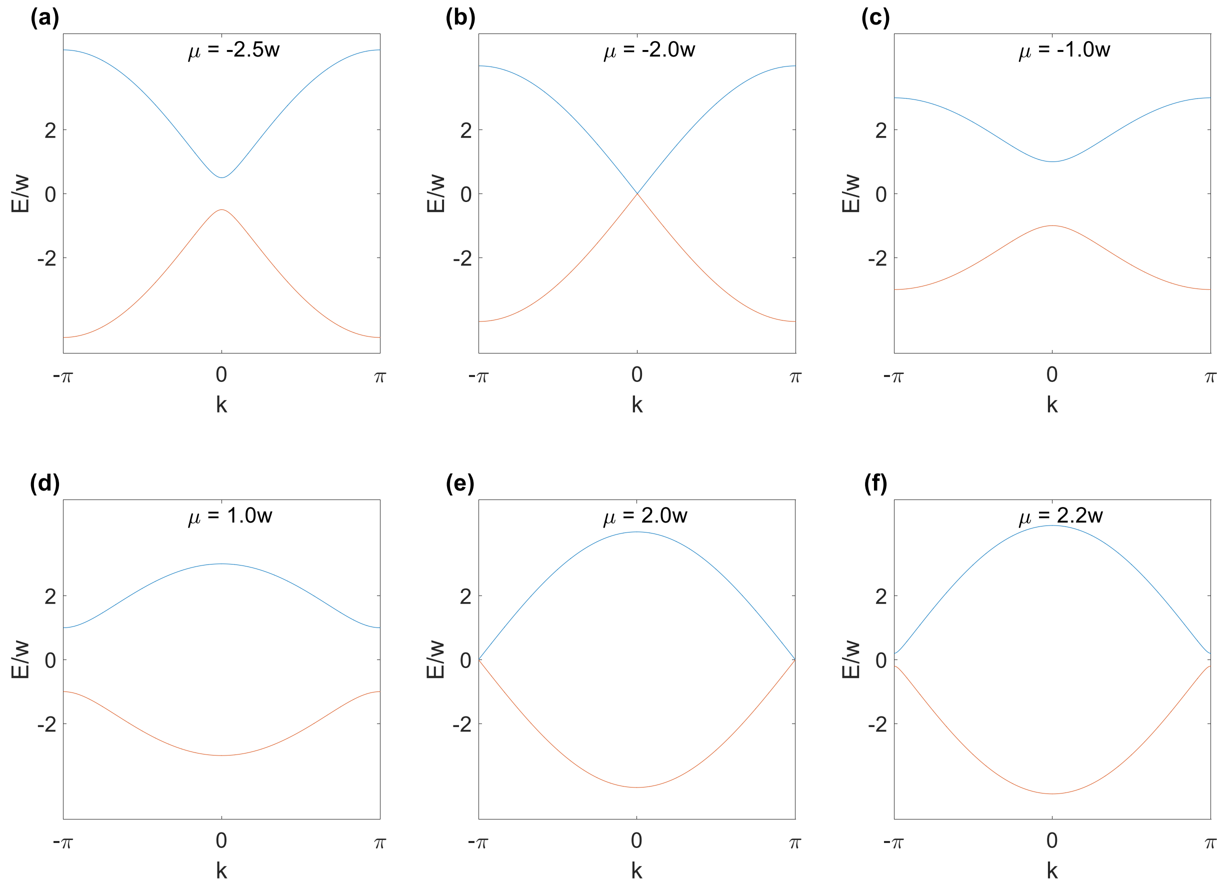

Figure 2.3. Energy spectrum of the Kitaev ring model at different chemical potentials when $\Delta = w$. Figure (c) and (d) show the topological case and Figure (a), (b), (e) and (f) show the trivial case. $\mu = \pm 2\,w$ are critical points of topological phase transition.

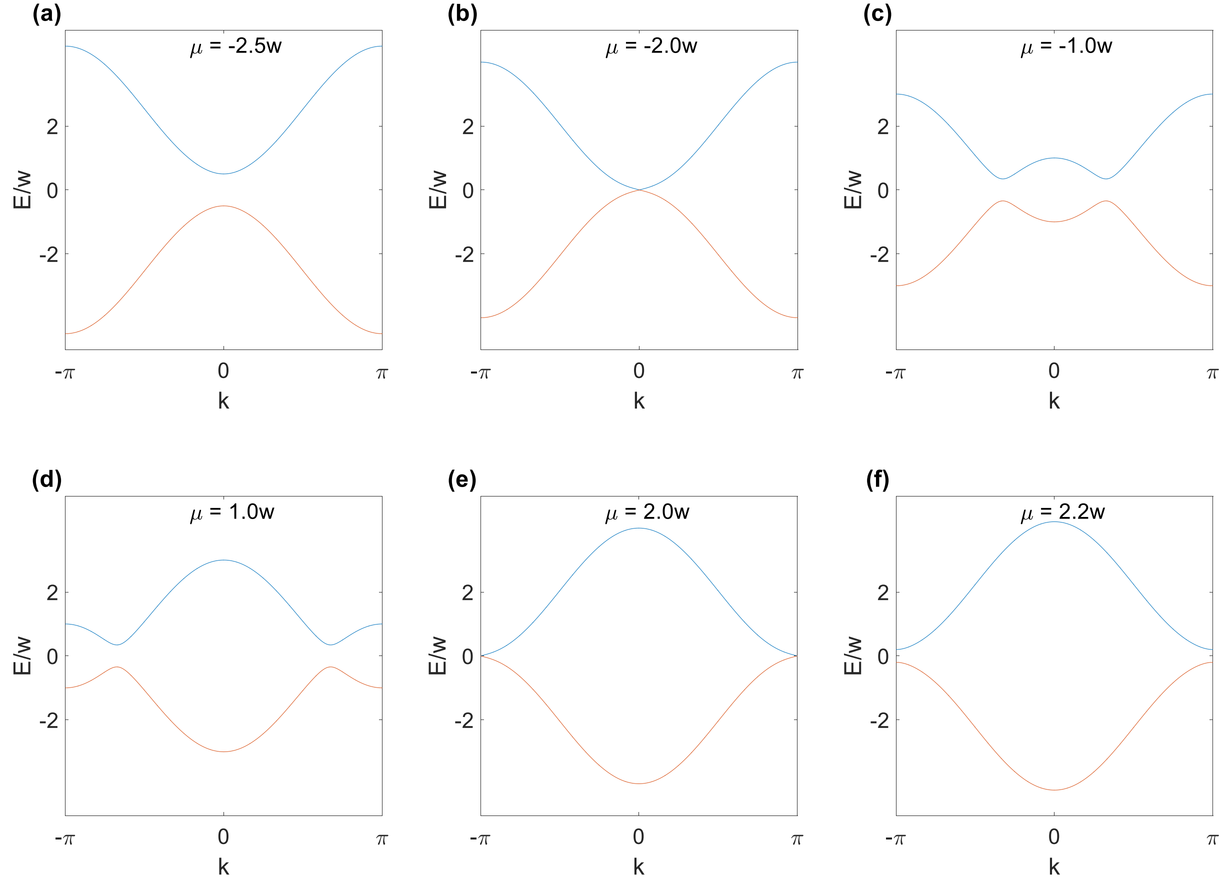

Figure 2.4. Energy spectrum of the Kitaev ring model at different chemical potentials when Δ = 0.2 w. Figure (c) and (d) show the topological case and Figure (a), (b), (e) and (f) show the trivial case. $\mu = \pm 2\ w$ are critical points of topological phase transition.

2.1.4 Issues of Kitaev Chain Model for Experiments

As for many other theoretical models, the Kitaev chain model is not based on realism from experiments. To realize this model experimentally is not easy. The most important issue is likely from the fact that this model is based on spinless electrons, or all the electrons have the same spin direction. For a chain of electrons, there are in general no limitations to restrict spin directions of all the electrons to be in the same direction. However, for the Kitaev chain model,

superconductivity is necessary. Within my knowledge, there are real superconductors which can induce electron pairs with different spin directions (spin-singlet superconductors) in a quantum wire. To induce electron pairs with the same spin direction, there seems to be no convincing experiments to demonstrate such a special superconductor. This uncommon superconductivity is called p-wave or triplet superconductivity. Even though efforts are made to discover a p-wave superconductor [35-37], the claim is still controversial [38, 39]. We need a more feasible model for experiments.

2.1.5 A More Feasible Model for MBSs

For approaching a more feasible model for experiments, we examine the physical picture of the Kitaev chain model shown in Figure 2.1. In experiments, the quantum wire can be a one-dimensional nanowire. By depositing superconducting contacts to the nanowire, the required superconducting gap can be induced. The chemical potential in the Hamiltonian suggests that the nanowire can be a semiconductor since semiconductors' chemical potential is gate-tunable. We can use electrostatic gates to tune the chemical potential of a semiconductor device since the electron density in a semiconductor is low. However, it is still not easy to find a p-wave superconductor to induce the desired electron pairing.

Instead of searching for a natural p-wave superconductor, people found that it is possible to achieve an effective p-wave superconductor with some extra components [4, 5]. The method is to use a nanowire with Rashba spin-orbit coupling and Zeeman field. In Figure 2.1, if the quantum wire is such a semiconductor and a magnetic field is applied along the wire, and by choosing the *x*-axis be along the wire, and the *y*-axis along the spin-orbit field direction, the Hamiltonian density of the nanowire is given as:

$$H_{wire} = \frac{p_x^2}{2m} - \mu - \frac{\alpha_R}{\hbar}\sigma_y p_x + B\sigma_x \quad \textbf{(2.18)}$$

where m is the effective electron mass in the semiconductor, α_R is the spin-orbit strength, σ_x and σ_y are the Pauli matrices, $\hbar$ is the reduced Planck's constant, and p_x and p_y are momentum operators:

$$p_x = -i\hbar\partial_x, \qquad p_y = -i\hbar\partial_y \quad \textbf{(2.19)}$$

By incorporating the induced superconducting gap into the nanowire's Hamiltonian, a quantum system that can have MBSs is achieved.

To show how a topological phase transition appears in the above hybrid system, we can write the system's Hamiltonian using the Bogoliubov-de Gennes Hamiltonian and solve for the energy spectrum by diagonalizing of H_{BdG}. For more detailed procedures, readers may check the reference [30]. Compared with equation (2.14) and equation (2.15), noticing that now this hybrid system not only has a subspace for electrons and holes, the freedom of spins also gives a spin subspace, the H_{BdG} matrix is four-dimensional instead of two-dimensional. That is why there are different types of Pauli matrices labeled by τ and σ. Therefore, we should have:

$$H = \frac{1}{2}\int dx\psi_k^\dagger H_{BdG}\,\psi_k, \qquad \psi_k = \left(\psi_\uparrow(k), \psi_\downarrow(k), \psi_\uparrow^\dagger(-k), \psi_\downarrow^\dagger(-k)\right)^\dagger \quad \textbf{(2.20)}$$

and H_{BdG} is:

$$H_{BdG} = \left(-\frac{\hbar^2 \partial_x^2}{2m} - \mu\right)\tau_z\sigma_0 - i\alpha_R\tau_z\sigma_y\partial_x + B\tau_z\sigma_x + \Delta\tau_y\sigma_y \tag{2.21}$$

where σ_0 is the zeroth Pauli matrix (just the identity matrix). The energy spectrum is:

$$E_{k,\pm}^2 = \xi_k^2 + (\alpha_R k)^2 + B^2 + \Delta^2 \pm 2\sqrt{B^2\Delta^2 + [B^2 + (\alpha_R k)^2]\xi_k^2} \tag{2.22}$$

$$\xi_k = \frac{\hbar^2 k^2}{2m} - \mu \tag{2.23}$$

Recall from the energy spectrum of the simple Kitaev chain model, we may expect that there should be an energy gap opening, closing and re-opening if there is a topological phase transition. Before that, we can check what is the role of spin-orbit coupling or Zeeman field in this system.

We use the parameters of devices based on InSb nanowires [6]. The induced gap is 0.25 meV and the spin-orbit coupling strength is 20 meV·nm. The effective electron mass is $0.015m_e$, where m_e is the electron mass in vacuum. First, when there is no spin-orbit coupling, Zeeman field and superconductivity, the remaining Hamiltonian just has the format for free electrons. The corresponding energy spectrum is shown in Figure 2.5 (a). The spectrum is the typical parabolic dispersion for free electrons in a solid. Visually we see two bands corresponding to electrons and holes. However, the Hamiltonian matrix is four-dimensional and there are four energy eigenstates. The state is double-degenerate since there is freedom from the two spin directions. When the spin-orbit coupling is added into the system, as shown in Figure 2.5 (b), the energy spectrum is still

parabolic. However, the energies of electrons or holes shifted away from zero *k*. The degeneracy is lifted except for the position at zero *k*. Now if there is a magnetic field, the degeneracy at zero *k* is also lifted and a gap is open. This is shown in Figure 2.5 (c). In Figure 2.5 (d), superconductivity is also involved. Further gaps are open and this gives separated energy dispersions for different spins. Therefore, we indeed have the desired spinless model.

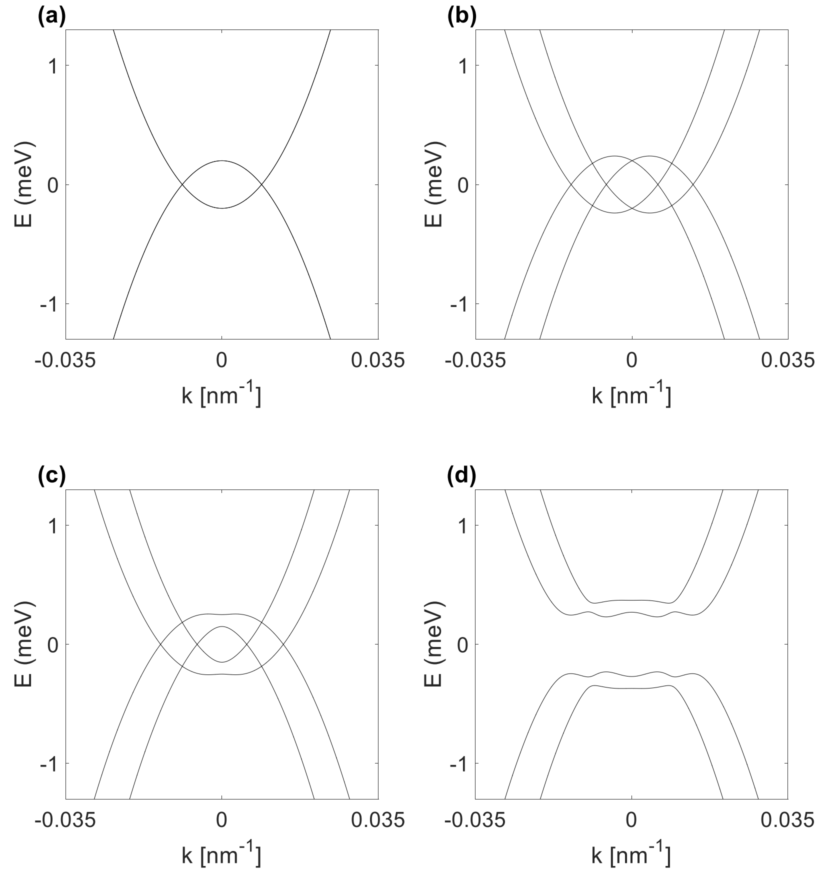

Figure 2.5. Energy spectrum of the hybrid superconductor-semiconductor nanowire model. The chemical potential is 0.2 meV. (a) B = 0, α_R = 0 and Δ = 0. (b) B = 0, α_R = 20 meV·nm and Δ = 0. (c) B = 0.05 meV, α_R = 20 meV·nm and Δ = 0. (d) B = 0.05 meV, α_R = 20 meV·nm and Δ = 0.25 meV.

When there is a gap in the energy spectrum, it does not necessarily mean that there is a topological phase transition. Though, we can deduce a topological phase transition if there is a gap opening, closing and re-opening. It can be justified from the zero lower band [4] that the critical Zeeman field B_c for a topological phase is:

$$B_c^2 = \Delta^2 + \mu^2 \quad \textbf{(2.24)}$$

In a real device, the values of α_R and Δ are not quite adjustable. Instead, the values of B and μ are parameters that can be tuned relatively easily. We examine a topological phase transition by examining different combinations of magnetic fields and chemical potentials.

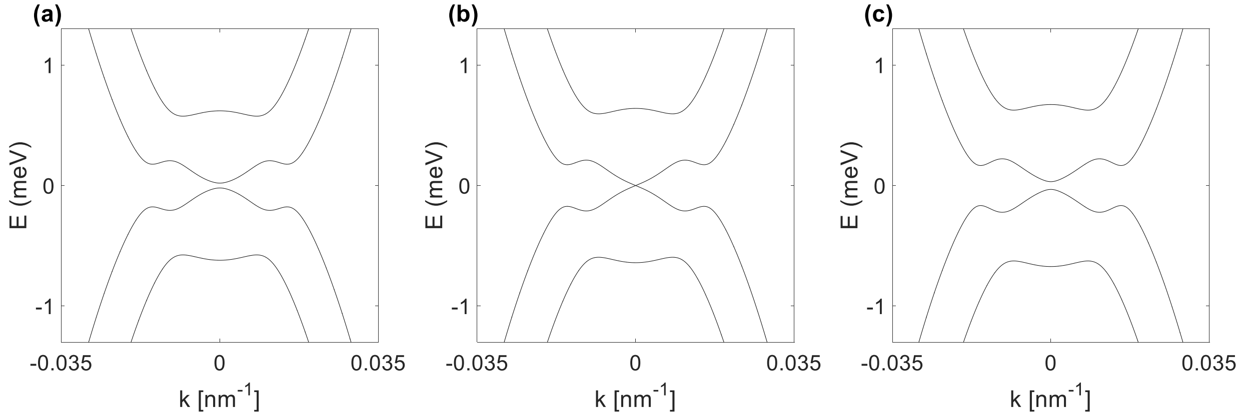

Figure 2.6. Energy spectrum of the hybrid superconductor-semiconductor nanowire model at different Zeeman fields. The parameters are: μ = 0.2 meV, α_R = 20 meV·nm and Δ = 0.25 meV. (a) B = 0.3 meV. (b) $B = B_c$. (c) B = 0.35 meV.

In Figure 2.6, a topological phase transition is shown by adjusting the Zeeman field. In Figure 2.6 (a), the Zeeman field is smaller than the critical field. There is a small energy gap at the

zero-*k* position. When the field is increased to the critical field, the gap at zero *k* is closed, as shown in Figure 2.6 (b). In Figure 2.6 (c), the Zeeman field is increased to a value larger than the critical field, the energy gap at zero *k* appears again. The re-opening of the energy gap indicates that there is a topological phase transition and thus, appearance of MBSs.

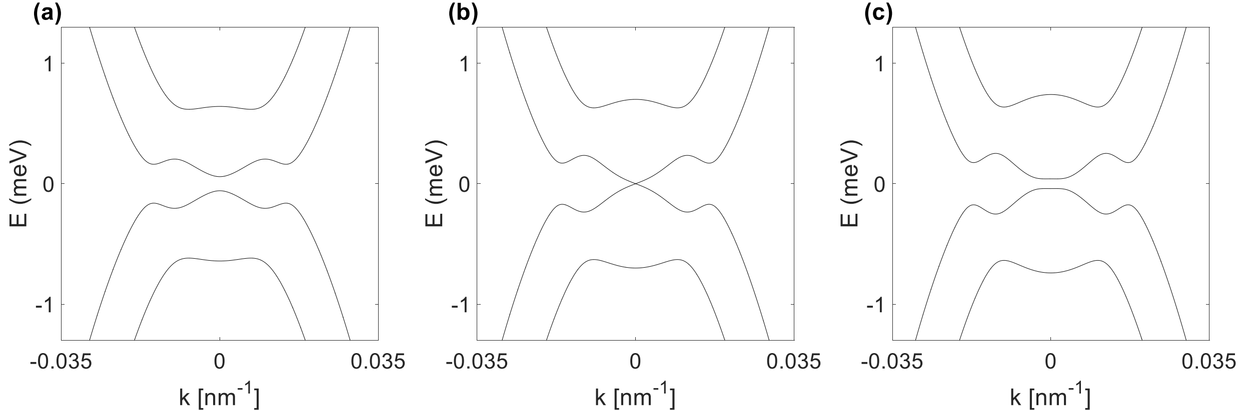

Figure 2.7. Energy spectrum of the hybrid superconductor-semiconductor nanowire model at different chemical potentials. The parameters are: B = 0.35 meV, α_R = 20 meV·nm and Δ = 0.25 meV. (a) μ = 0.15 meV. (b) $\mu = \mu_c$. (c) μ = 0.3 meV.

The topological phase transition can also be shown by adjusting the chemical potential. We can define the critical chemical potential μ_c from equation (2.24):

$$\mu_c^2 = B^2 - \Delta^2 \quad \textbf{(2.25)}$$

The corresponding plots are given in Figure 2.7. In Figure 2.7 (a), the chemical potential is smaller than the critical chemical potential and we observe an energy gap at $k = 0$. In Figure 2.7 (b), the chemical potential is equal to the critical value and the energy gap at $k = 0$ is closed. In Figure 2.7

(c), the chemical potential is increased to a larger value than the critical value. The energy gap at $k = 0$ re-opens, just as expected.

To conclude this section, we recall the physical picture of the hybrid superconductor-semiconductor nanowire model and its Hamiltonian. This model is more feasible than the simple Kitaev chain model and the topological phase transition can be achieved by adjusting magnetic fields or chemical potentials. It tells us that for experiments for MBSs, we can select common superconductors and semiconductor nanowires with strong spin-orbit interaction as platforms. For such a device that satisfies the conditions for MBSs, we can also call it a topological superconductor.

2.2 Quantum Dots

The discussion above focuses on MBSs but a physical device like that in Figure 2.1 can be more than a simple platform only for topological phases. One-dimensional semiconductor nanowires can be platforms of different physical phenomena. One important phenomenon commonly observed experimentally is a quantum dot [40, 41]. This section is a brief introduction of this concept in a semiconductor nanowire. A more detailed review of quantum dots can be found in references [42, 43].

2.2.1 The General Physical Picture of Quantum Dots

A quantum dot can be thought of as a physical object that has available states empty or filled for electrons or holes. Experimentally, a quantum dot can be fabricated by quantum

confinement in zero-dimensional nanostructures which provide discrete levels of electron energy states. Recall from basic quantum mechanics, a quantum well can be formed by applying potential barriers which confine particles. In Figure 2.8, a diagram of a semiconductor nanowire quantum dot device is shown. A semiconductor nanowire is placed on a substrate with a source and a drain. Three electrostatic gates are underneath the nanowire. For a one-dimensional nanowire, an electron is only free to move along the nanowire. Applying voltage to gates G_1 and G_3 can create potential barriers and defines quantum confinement. Therefore, the nanowire section between the gates G_1 and G_3 can be a quantum dot and the energy levels in the dot can be tuned by gate G_2. This is not the only method to fabricate a quantum dot, but it is straightforward for a device based on a semiconductor nanowire. In real experiments, a simple nanowire with a source, a drain and only one gate may still have quantum dots, which indicates that potential barriers may form without sophisticated design of potential barriers.

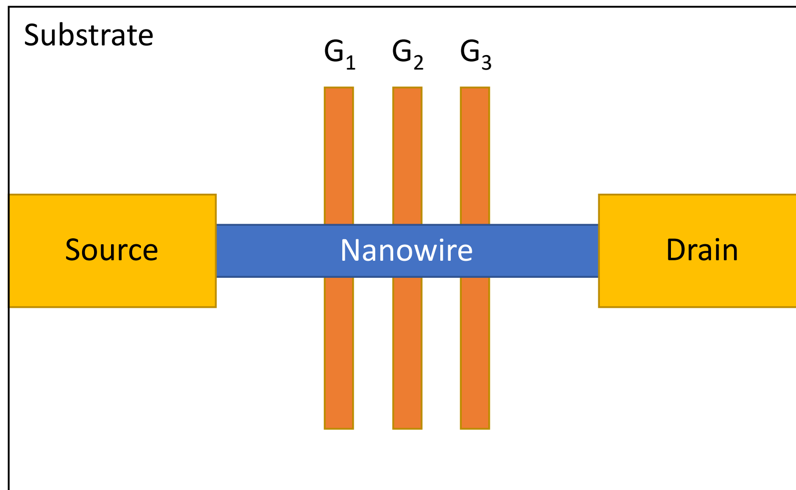

Figure 2.8. A diagram of a semiconductor nanowire quantum dot device. Gates G_1 and G_3 define a dot by creating potential barriers and gate G_2 can tune the energy levels in the dot.

Quantum transport measurements of quantum dots monitor tunneling of electrons through the quantum dots. The energy levels in an electron dot are discrete. A finite energy is required to add an extra electron into the dot. We expect to observe sharp peaks of measured current if a voltage bias is applied across the source and the drain because an extra electron can be added by increasing voltage bias. Figure 2.9 shows a quantum dot device based on lead telluride (PbTe) nanowires. The device has metal contacts as a source and a drain. It has a back-gate underneath the nanowire and a top-gate on top of the nanowire. Figure 2.10 shows the differential conductance of a PbTe nanowire dot from quantum transport measurement. We observe distinct lines from the differential conductance which are just the expected peaks due to the discrete energy levels inside the dot. The voltage bias adjusts the chemical potentials of the source and drain. The tuning of the top gate voltage V_{tg} adjusts the available energy levels for electrons or holes that can tunnel into the dot. This gives the diamond feature of the plots. Magnetic fields can also influence the energy levels, for example, splitting the energy levels for spin up and spin down electrons. This is also shown in Figure 2.10.

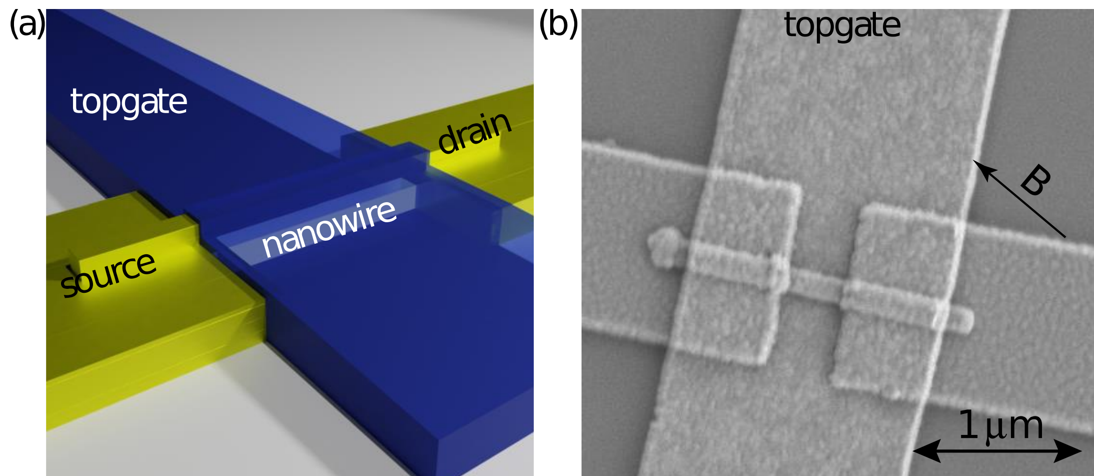

Figure 2.9. A PbTe nanowire quantum dot device. (a) The conceptual diagram of the device. (b) SEM image of the device. The source and drain are Ti/Au contacts. A back-gate is underneath the nanowire and a top-gate is on top of the nanowire. The figure is adapted from [41].

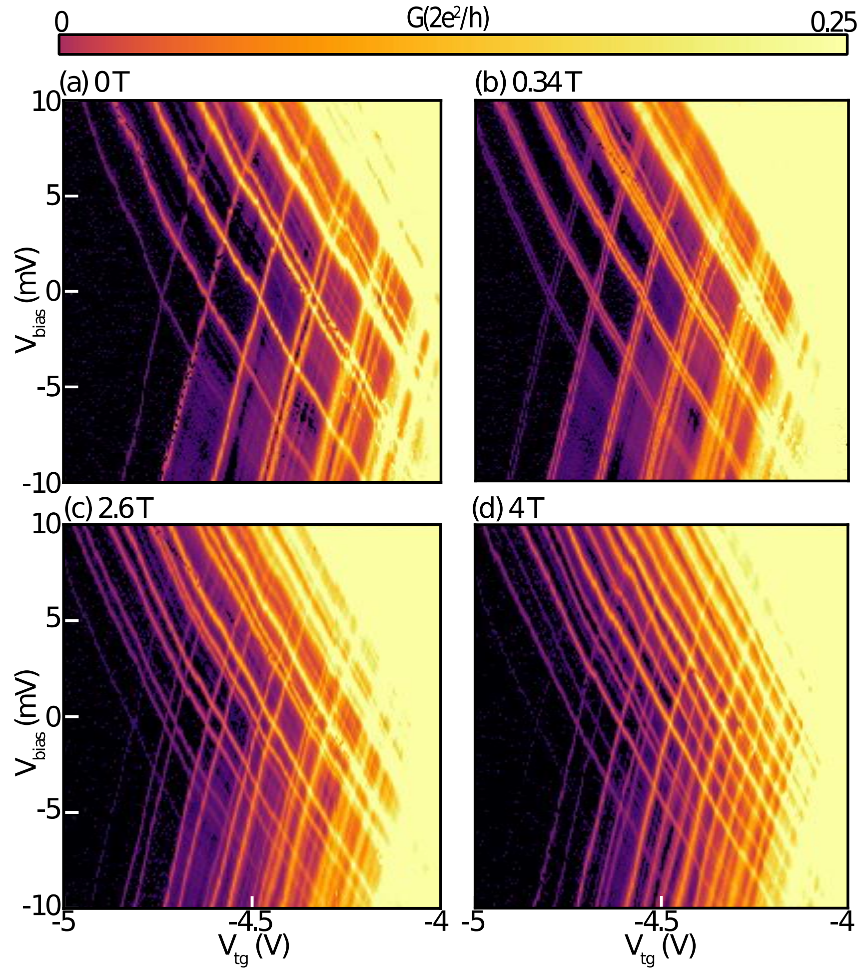

Figure 2.10. Differential conductance of a PbTe nanowire quantum dot device with different combinations of bias voltage V_{bias} and top gate voltage V_g at different magnetic fields B. The back-gate underneath the nanowire is set at -15 V. (a) B = 0 T. (b) B = 0.34 T. (c) B = 2.6 T. (d) B = 4.0 T. The figure is adapted from [41].

The quantum dot demonstrated in Figure 2.9 and Figure 2.10 is not usual because of the absence of Coulomb blockade [41]. Coulomb blockade is a phenomenon due to charging energy from electrons and exists in more conventional quantum dots. In the next sub-section, we introduce Coulomb blockade and a simple model of quantum dots.

2.2.2 Coulomb Blockade and Constant-interaction Model

When two particles have the same type of charge, they may feel a force which is repulsive. Two electrons have the same negative charge and they are repulsive with each other. This Coulomb repulsion introduces another important factor for a quantum dot device. To add an extra electron into a dot, energy cost is required to overcome the Coulomb repulsion. When the provided energy is not enough, no electrons can tunnel into the dot and this phenomenon is known as Coulomb blockade. Coulomb repulsion and the confinement discussed in the above section dominate the behaviors of a quantum dot.

To quantitatively describe a quantum dot, we may use the constant-interaction model [44]. In this model, the interactions between electrons or holes in the dot and other reservoirs are described by constant capacitance. A quantum dot can be described as an object coupled with a source, a drain and a gate. The corresponding electrical circuit is given in Figure 2.11. The difference of the chemical potential μ_{left} *and* μ_{right} of the left and right lead is given by the bias voltage such that $eV_{bias} = \mu_{left} - \mu_{right}$. The ground state energy of an N electron dot is defined as $U(N)$ and the total capacitance C is given as $C = C_g + C_L + C_R$. For a small bias, the constant-interaction model tells us that:

$$U(N) = \frac{\left[e(N - N_0) + C_g V_g\right]^2}{2C} + \sum_N E_n(B) \qquad \textbf{(2.26)}$$

where B is the applied magnetic field, $E_n(B)$ is the occupied energy levels of the confined quantum well, and $N = N_0$ for zero V_g. The chemical potential of the dot $\mu(N)$ can be calculated as:

$$\mu(N) = U(N) - U(N-1) = \left(N - N_0 - \frac{1}{2}\right) E_c + \frac{E_c}{e} C_g V_g + E_N \tag{2.27}$$

where $E_c = e^2/C$ is called the charging energy. The energy required to add one extra electron is:

$$E_{add}(N) = \mu(N+1) - \mu(N) = E_c + E_{N+1} - E_N \tag{2.28}$$

This quantitative description is a powerful tool to analyze experimental data from a quantum dot device. It is clear that a two-dimensional plot of differential conductance as a function of bias voltage and gate voltage has diamond-like features. When there is the charging energy from Coulomb repulsion, we call these features Coulomb diamonds.

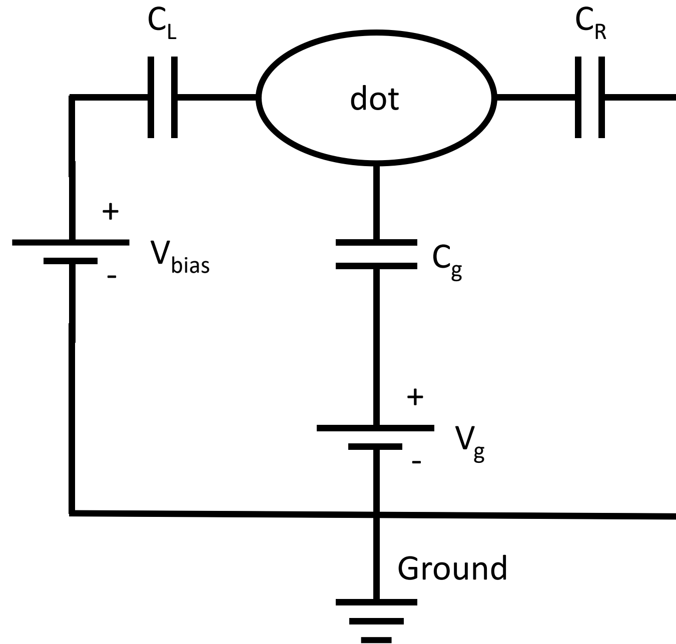

Figure 2.11. The circuit diagram of a quantum dot device.

To have a more direct understanding of a quantum dot, Figure 2.12 gives the progress of how an extra electron can be added to a quantum dot. In Figure 2.12 (a), the energy levels equal to or lower than μ (N-1) have been filled by electrons. The chemical potential of higher energy levels in the dot is higher than the chemical potential of available electrons in the left lead or right lead. Thus, electrons cannot go from the left lead or right lead to the dot. This is the condition for block. Now, we adjust the position of the energy levels in the dot by tuning the gate. For the energy levels shown in Figure 2.12 (b), μ (N) is now still higher than the right lead's chemical potential but is lower than the left lead's chemical potential. An extra electron can go from the left lead to the dot and then from the dot to the right lead. If we monitor this device as adjusting the gate voltage from the conditions shown in Figure 2.12 (a) to Figure 2.12 (b), a differential conductance peak will appear, indicating the transport of an extra electron. When the energy level μ (N) is filled by the extra electron in Figure 2.12 (b), this device is again blocked if μ (N) is tuned to be lower than μ_{right}. To add even more electrons to the dot, the gate voltage has to be tuned again.

Figure 2.13 demonstrates a quantum dot device fabricated by InSb nanowire and the measured conductance spectroscopy. From the conductance spectroscopy, we observe diamond-like features. Unlike the PbTe nanowire quantum dots shown in Figure 2.9 and 2.10, there is Coulomb blockade [45] and we call these diamond-like features Coulomb diamonds.

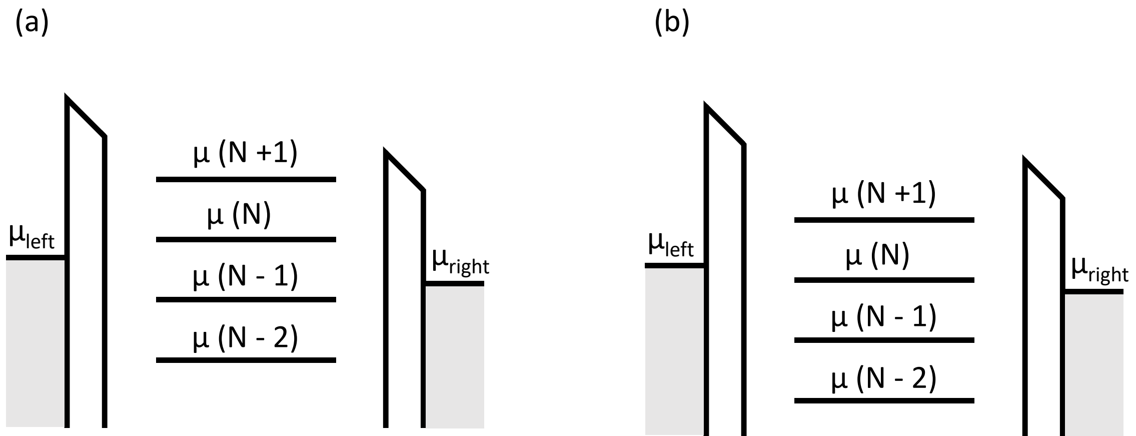

Figure 2.12. Schematics of a quantum dot at low bias. (a) There are no energy levels in the dot between the chemical potentials μ_{left} and μ_{right} on the leads. No electrons can transport to the dot. (b) There is an energy level in the dot between the chemical potentials μ_{left} and μ_{right} on the leads. One extra electron can transport from the left lead to the dot and from the dot to the right lead.

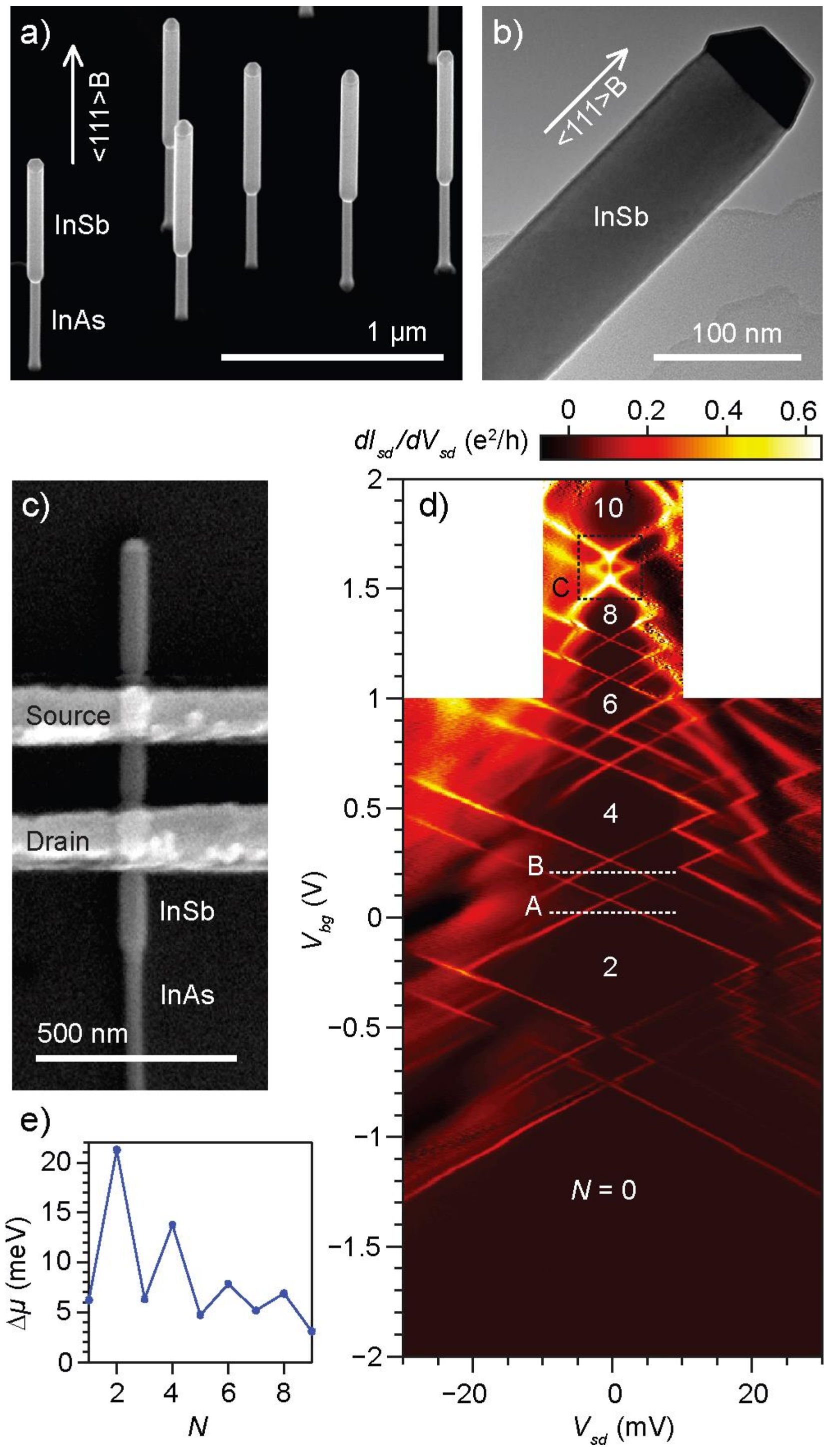

Figure 2.13. Sample description and conductance spectroscopy of an InSb nanowire quantum dot. This figure and its caption are adapted with permission from [45]. Copyright

{2009} American Chemical Society. (a) SEM image of InAs/InSb heterostructure nanowires grown on an InAs(111)B substrate using aerosol gold particles with a diameter of 40 nm as initial seeds. The image is recorded with a 30° tilt of the substrate from the horizontal position and the scale bar is uncompensated for the tilt. In the heterostructure nanowires, the base segments with a small diameter are InAs, crystallizing in the wurtzite phase, and the upper segments with a large diameter are InSb, crystallizing in the zinc blende phase. Note that the InSb segments do not show any tapering at the sidewalls. (b) TEM image of a top part of an InSb nanowire, after detachment from the growth substrate, with the single crystalline $AuIn_2$ seed particle on top and the pure zinc blende InSb nanowire segment below. This InSb nanowire segment has a diameter of 79 nm. (c) SEM-picture of an InSb quantum dot device. The device is made by electrically contacting the InSb segment of an InAs/InSb heterostructure nanowire on a SiO_2 capped, highly doped Si substrate using electron beam lithography. (d) Differential conductance on a color scale as a function of the source-drain voltage V_{sd} and the back-gate voltage applied to the Si substrate V_{bg} (charge stability diagram), measured for an InSb nanowire quantum dot device with a nanowire diameter of 70 nm and a contact spacing of 70 nm. The conventional spin-1/2 Kondo effect (a Kondo enhanced conductance ridge) at zero bias is observed in the N = 9 Coulomb blockade diamond region. (e) Addition energy versus electron number in the InSb nanowire quantum dot measured in (d) (addition energy spectrum), revealing a typical shell structure of a few-electron quantum dot system.

2.2.3 Semiconductor Nanowire Devices and Quantum Dots

As a one-dimensional or quasi one-dimensional material, a semiconductor nanowire is naturally a good platform for quantum dots since it is easy to confine electrons. On the other hand, a device based on semiconductor nanowires may have unwanted quantum dots which may complicate the behaviors of the device. It is important to notice possible quantum dots for experiments not aiming at quantum dots.

Quantum dots are also possible platforms for quantum computation. For people who have an interest in this topic, these references may be helpful [46-48].

2.3 Superconducting Proximity and Andreev Bound States

Both the Kitaev chain model and the hybrid superconductor-semiconductor nanowire model need a superconducting gap. This gap is from superconducting proximity. However, this device for MBSs is also a good platform for quantum dots. For MBSs, we want the superconducting proximity only supporting the gap and providing pairs of electrons. However, when a quantum dot is coupled with a superconductor, energy states other than MBSs can appear. A very important state is the Andreev bound state since ABSs and MBSs share similar features. In this section, we examine the superconducting proximity and ABSs in semiconductor nanowires.

2.3.1 Superconducting Proximity and Andreev Reflection

When a semiconductor is connected to a superconductor, the superconductor may introduce its superconducting properties into the semiconductor. This is the superconducting proximity. This can be a natural phenomenon and in general, proximity effects may appear when two objects with different properties are connected. For example, when a superconductor is connected with a ferromagnet, the superconductor may feel the ferromagnetic proximity. In a hybrid superconductor-semiconductor nanowire device for MBSs, the superconducting proximity induces a superconducting gap in and provides electron pairs for the nanowire. To understand the transport mechanism, we need to examine the interface between the semiconductor and the superconductor.

The interface of a semiconductor and a superconductor is the boundary between two very different objects. The properties of electrons in a semiconductor and in a superconductor are essentially different and the boundary is a natural barrier for electrons. When an electron hits the barrier, it may "bounce" back, just as a ball thrown onto a wall. The schematic of this procedure is shown in Figure 2.14 (a). An electron coming from the N side (a semiconductor) hits the boundary to the S side (a superconductor). The electron is reflected back and there is no electron transported to the superconductor in this case. We call this mechanism normal reflection.

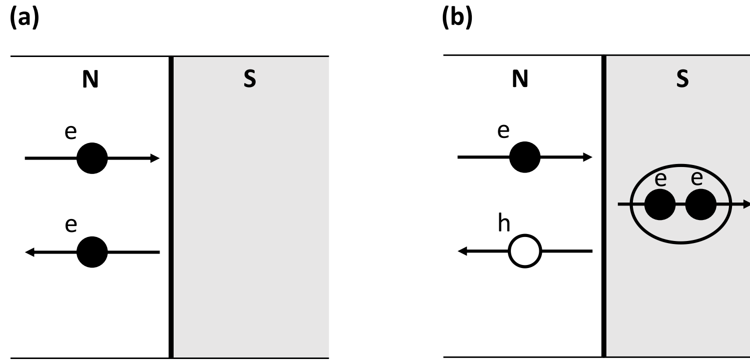

Figure 2.14. Schematics of different reflection mechanisms at the interface of a semiconductor (N) and a superconductor (S). (a) Normal reflection where an electron coming from the N side hits the interface and reflects back. (b) Andreev reflection where an electron coming from the N side hits the interface and reflects as a hole, leaving a pair of electrons into the superconductor.

For an N-S interface, the interesting point is that there is another possible reflection mechanism, called Andreev reflection. This special reflection is shown in Figure 2.14 (b). When a coming electron in the N side hits the N-S interface, the electron reflects back as a hole and since the charge needs to be conserved, a pair of electrons appears in the superconductor. Superficially, a superconductor has a gap which forbids electrons without enough energy to transport into the superconductor. This means that a large voltage bias compared to the induced superconducting gap is required if transport of electrons through the superconductor is wanted. Otherwise, for a small bias, the provided electrons have energies smaller than the superconducting gap and a current cannot be developed. However, Andreev reflection gives the possibility for developing a current through the N-S interface even at a small bias. A semiconductor with superconducting proximity may have states inside the induced superconducting gap.

A quantitative description of Andreev reflection is given by the Blonder-Tinkham-Klapwijk (BTK) model [49]. For the case given in Figure 2.14, we set the S-N interface at $x = 0$. We consider a superconductor described by the BdG formalism with gap $\Delta(x)$, chemical potential $\mu(x)$ and Hartree potential V(x). In this physics system, the wave function of electrons or holes is represented by a column vector:

$$\psi_k = \begin{bmatrix} u_k(x,t) \\ v_k(x,t) \end{bmatrix} \tag{2.29}$$

such that:

$$\left[-\frac{\hbar^2}{2m}\nabla^2 + V(x) - \mu(x)\right]u_k(x,t) + \Delta(x)v_k(x,t) = i\hbar\frac{\partial u_k(x,t)}{\partial t} \tag{2.30}$$

$$-\left[-\frac{\hbar^2}{2m}\nabla^2 + V(x) - \mu(x)\right]v_k(x,t) + \Delta^*(x)u_k(x,t) = i\hbar\frac{\partial v_k(x,t)}{\partial t} \tag{2.31}$$

In the superconductor far away from the S-N interface, $\Delta(x)$, $\mu(x)$ and V(x) are constants and the solutions of the wave functions have the format of planes waves:

$$\psi_k = \begin{bmatrix} u_k(x,t) \\ v_k(x,t) \end{bmatrix} = \begin{bmatrix} u_k e^{ikx - iE_k t/\hbar} \\ v_k e^{ikx - iE_k t/\hbar} \end{bmatrix} \tag{2.32}$$

By substituting equation (2.32) to the equation (2.30) and (2.31), for $V(x) = 0$, the wave functions are solved to be:

$$\psi^S_{\pm k_\pm} = e^{\pm i k_\pm x} \begin{bmatrix} \sqrt{\frac{1}{2}\left(1 \pm \frac{\sqrt{E_k^2 - \Delta^2}}{E_k}\right)} \\ \sqrt{\frac{1}{2}\left(1 \mp \frac{\sqrt{E_k^2 - \Delta^2}}{E_k}\right)} \end{bmatrix} e^{-iE_k t/\hbar} \quad \textbf{(2.33)}$$

Here, we use k_+ for electrons and k_- for holes. The superscript S on the wavefunction indicates that these solutions are applicable to the superconductor side.

Similarly, in the normal region far away from the interface, we can solve for the wavefunctions where $V(x) = \Delta(x) = 0$. We use superscript N to indicates that the following solutions are in the normal region:

$$\psi^N_{\pm k_+} = e^{\pm i k_+ x} \begin{bmatrix} 1 \\ 0 \end{bmatrix} e^{-iE_k t/\hbar} \quad \textbf{(2.34)}$$

$$\psi^N_{\pm k_-} = e^{\pm i k_- x} \begin{bmatrix} 0 \\ 1 \end{bmatrix} e^{-iE_k t/\hbar} \quad \textbf{(2.35)}$$

The wavefunctions in this system include the incident wave, the reflected wave and the transmitted wave:

$$\psi^N_{inc} = \begin{bmatrix} 1 \\ 0 \end{bmatrix} e^{i k_+ x} \quad \textbf{(2.36)}$$

$$\psi_{refl}^{N} = a\begin{bmatrix}0\\1\end{bmatrix}e^{ik_{-}x} + b\begin{bmatrix}1\\0\end{bmatrix}e^{-ik_{+}x} \tag{2.37}$$

$$\psi_{trans}^{S} = c\begin{bmatrix}u_{k0}^{2}\\v_{k0}^{2}\end{bmatrix}e^{ik_{+}x} + d\begin{bmatrix}v_{k0}^{2}\\u_{k0}^{2}\end{bmatrix}e^{-ik_{-}x} \tag{2.38}$$

where:

$$u_{k0}^{2} \equiv \frac{1}{2}\left(1 + \frac{\sqrt{E_{k}^{2} - \Delta^{2}}}{E_{k}}\right), \qquad v_{k0}^{2} \equiv \frac{1}{2}\left(1 - \frac{\sqrt{E_{k}^{2} - \Delta^{2}}}{E_{k}}\right) \tag{2.39}$$

The wavefunction in the overall system needs to be continuous, including the N-S interface. Additionally, the derivative of the wavefunction at the interface needs to satisfy:

$$\frac{\hbar}{2m}\frac{d\psi^{S}(0)}{dx} - \frac{\hbar}{2m}\frac{d\psi^{N}(0)}{dx} = H\psi(0) \tag{2.40}$$

Given the above boundary conditions, we can solve for the coefficients in equation (2.37) and (2.38). Notice that the coefficients a and b correspond to the Andreev reflection and normal reflection, the conductance of the interface at zero-temperature limit is proportional to $[1 + |a|^2 - |b|^2]^2$. More detailed derivations of the conductance can be found in references [50, 51]. Experimentally, this conductance can be probed by a quantum point contact [52, 53].

2.3.2 Andreev levels and Andreev Bound States

When a semiconductor quantum dot is coupled with a superconductor, the superconducting proximity plays a significant role. For a quantum dot with discrete energy levels for electrons, two electrons are not preferred to form a pair since Coulomb repulsion trends to separate two electrons. Even though spin-up and spin-down electrons may share the same energy level, Coulomb repulsion requires the additional charging energy and for a quantum dot, electrons are preferred to be added one-by-one. However, in a superconductor, electrons are paired and an even number of electrons are preferred to transport into the superconductor. Thus, for a quantum dot coupled with a superconductor, there is a competition between Coulomb repulsion and pairing of electrons.

To understand what phenomena are introduced from the superconductivity to a quantum dot, we consider the simple case of a quantum dot filled with one electron and there are two possible ground state energies. This ground state is two-fold degenerate due to the spin directions. Classified by the total spin, the ground state can be a spin doublet $|D\rangle$ (spin 1/2) or a spin singlet $|S\rangle$ (spin 0). If the spin doublet is the ground state, the spin singlet is the excited state, and vice versa. The possible energy excitations are depicted in Figure 2.15. When there is a magnetic field, the spin doublet splits due to the Zeeman effect. If the ground state is $|D\rangle$, there is not a measurable excitation from the extra split state. If the ground state is $|S\rangle$, excitations can be measured from both split states.

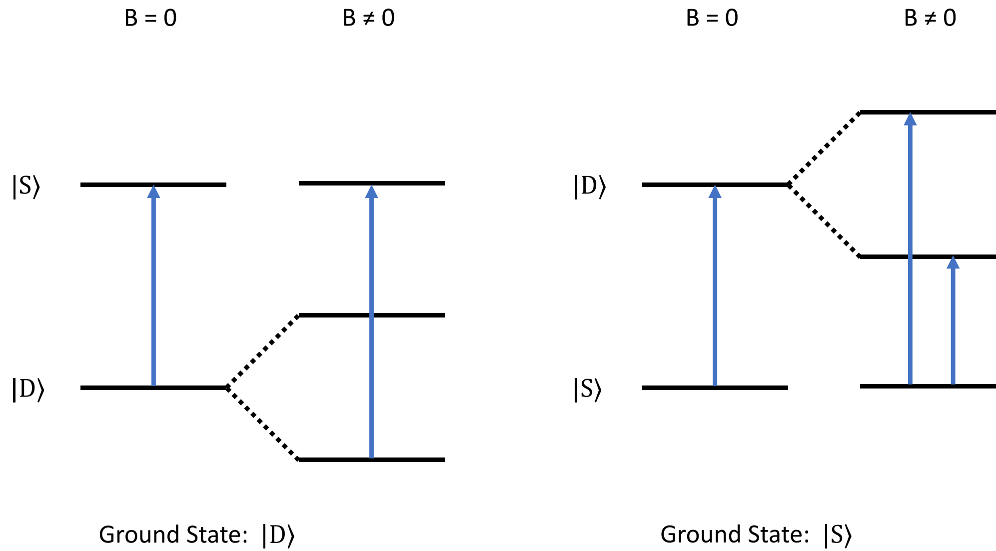

Figure 2.15. Possible energy excitations in a quantum dot coupled with a superconductor. The ground state can be a spin doublet (|D⟩) or a spin singlet (|S⟩). When there is a magnetic field, the spin doublet splits and the excitations are different depending on the ground state.

When a new electron enters the dot, excitation from the ground state to the excited state is induced. Since the quantum dot is coupled with a superconductor, the excited electron can be released by Andreev reflection such that the electron is reflected back as a hole and leaves a pair of electrons in the superconductor. This procedure enables electron transport from the dot to the superconductor at particular bias voltages in the induced superconducting gap. The corresponding energy levels inside the gap are called Andreev levels, which can be deduced from the excitation energy. The Andreev levels are depicted in Figure 2.16. More details about these Andreev levels from experiments can be found in the references [54-56].

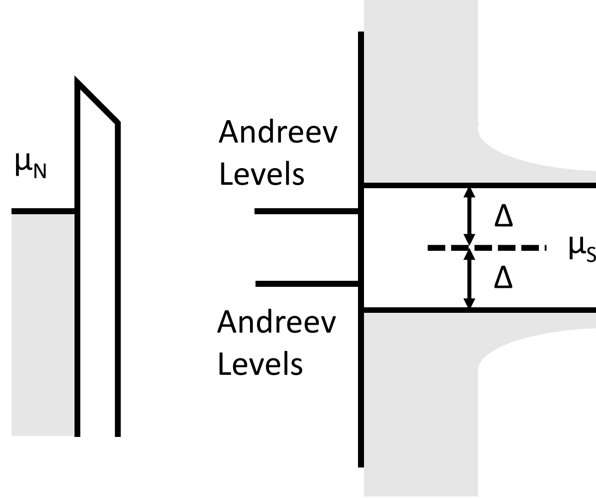

Figure 2.16. Schematic of a quantum dot coupled with a superconductor. μ_N is the chemical potential of a normal (not superconducting) lead connected to the quantum dot and μ_S is the chemical potential of the superconductor. Andreev levels exist due to Andreev reflection and when μ_N is aligned with an Andreev level, electron transport is possible from the normal lead to the superconductor.

To calculate the Andreev levels, we may consider Hamiltonians from leads (H_i), a quantum dot (H_d) and the coupling between the dot and the lead (H_{T_i}). They can be written as [57]:

$$H_i = \sum_{k,\sigma} \epsilon_k a^\dagger_{k,\sigma,i} a_{k,\sigma,i} - \sum_k \left(\Delta_i a^\dagger_{k,\uparrow,i} a^\dagger_{-k,\downarrow,i} + h.c.\right) \quad \textbf{(2.41)}$$

$$H_d = \sum_{\sigma} \epsilon_d d_k^{\dagger} d_k + U n_{\uparrow} n_{\downarrow}, \qquad n_{\sigma} = d_{\sigma}^{\dagger} d_{\sigma} \tag{2.42}$$

$$H_{T_i} = \sum_{k,\sigma} \left(t d_k^{\dagger} a_{k,\sigma,i} + h.c. \right) \tag{2.43}$$

Thus, the total Hamiltonian H is:

$$H = \sum_{i} H_i + H_d + \sum_{i} H_{T_i} \tag{2.44}$$

where d_{σ} is the electron operator with spin σ in the dot, $a_{k,\sigma,i}$ is the electron operator with spin σ, and wave vector k in the lead i, t is the coupling coefficient between the lead and the dot, U corresponds to Coulomb interaction. There is no analytical solution to the above H but an effective local Hamiltonian (H_{eff}) can be deduced by expansion around a superconducting atomic limit [57]:

$$H_{eff} = \sum_{\sigma} \xi_d d_{\sigma}^{\dagger} d_{\sigma} - |\Gamma_{\varphi}| \left(d_{\uparrow}^{\dagger} d_{\downarrow} + h.c. \right) + \frac{U}{2} \left(\sum_{\sigma} \left(d_{\sigma}^{\dagger} d_{\sigma} - 1 \right) \right)^2$$

$$\xi_d = \epsilon_d + \frac{U}{2} \tag{2.45}$$

where Γ_{φ} gives a local pairing amplitude induced by the leads on the dot. The energies corresponding to BCS-like states are solved to be [57]:

$$E_{\pm}^{0} = \frac{U}{2} \pm \sqrt{{\xi_d}^2 + {\Gamma_\varphi}^2} + \xi_d \quad \textbf{(2.46)}$$

From equation (2.46), we indeed see that there are two possible ground states since E_{-}^{0} is always smaller than E_{+}^{0}. It is the low energy BCS-like state (spin-singlet state) or the spin-doublet state. The boundary between the spin-singlet and the spin-doublet is at ${\xi_\mathrm{d}}^2 + {\Gamma_\varphi}^2 = U^2/4$. Figure 2.17 gives the corresponding phase diagram.

In literature (and this thesis), these small-bias states inside the induced gap are called Andreev bound states. The concept of ABS is also used for hybrid superconductor-semiconductor-superconductor (S-N-S) devices. In these devices, there are two N-S interfaces, and an electron pair may transport between the two superconductors by Andreev reflections. A supercurrent can be injected into these devices [58, 59] and these devices are also called Josephson junctions.

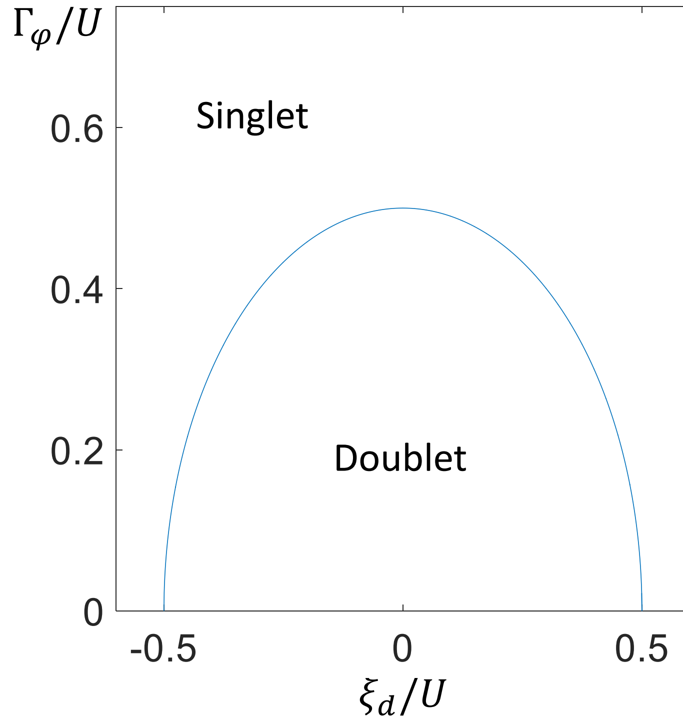

Figure 2.17. Phase diagram of a quantum dot coupled with superconductors. The transition line is from E_-^0. The ground state can be singlet or doublet based on this diagram.

2.3.3 Resonant Transmission and the Signature of Majorana Bound States

We discussed the topological phase transitions in a hybrid S-N nanowire device for MBSs. Even though a topological phase is predicated, the energy spectrum generated from the corresponding model does not give us direct information about what people expect to observe for a topological phase transition. There are other types of phase transitions in nature and some of them are easily observed. For example, for a transition from solid to liquid, we can observe the clear change from ice to water.

For quantum transport measurement of MBS devices, there is indeed a signature to be observed. Recall that MBSs exist on the two ends of the nanowire and the ends are just located at

the position of the N-S interface. Together with the Andreev reflection, there is a resonant transmission. When a voltage bias is applied on the MBS device and corresponding parameters are adjusted to meet the topological conditions, a zero-bias peak of the differential conductance will appear as the appearance of the Majorana modes. It is even predicted that this ZBP should be quantized to $2e^2/h$ [60, 61], where h is Planck's constant. This value is often referred to as the conductance quantum, G_0. This can be thought of as a resonant Andreev reflection induced by MBSs. For an Andreev reflection coefficient, a given in equation (2.37), the tunneling current at the S-N interface is:

$$I = \frac{2e}{h} \int_0^{eV} |a|^2 dE \tag{2.47}$$

where the applied voltage is smaller than the induced superconducting gap. In the discussed system of this sub-subsection, the particle-hole symmetry requires a perfect Andreev reflection [60, 61] such that $|a|^2 = 1$. The differential conductance is therefore G_0.

Even though there are experiments reporting ZBPs in the nanowire MBS devices [6-10, 62], alternative explanations other than MBSs of these ZBPs are also raised [12, 13, 63]. One possible reason for these ZBPs is the existence of ABSs. From the discussion of ABSs, there are Andreev levels which may also induce the resonant transmission. When the Andreev levels are located around zero-bias, it is possible to result in a ZBP. Unfortunately, ZBPs due to ABSs share similar features with ZBSs predicted for MBSs. Particle-hole symmetry is no-longer guaranteed and the magnitude of a ZBP from ABSs can have a variety of values including G_0. It can be larger than or smaller than G_0 as well. Unlike MBSs, ABSs are trivial states and not topologically

protected. Within my knowledge, it is difficult to distinguish ZBPs due to ABS from ZBPs due to MBSs. In Chapter 6, more details about these ZBPs will be discussed.

3.0 Methods of Device Fabrication and Experiments

In this thesis, experiments are based on narrow-gap semiconductor nanowires with strong spin-orbit interaction. Nanowires are in direct contact with normal metals or superconductors. Additionally, ferromagnetic materials may be in direct contact with a nanowire or be placed close to a nanowire. Electrostatic gates are used to adjust the chemical potential in the nanowire. Quantum transport measurements are performed at low temperature inside dilution refrigerators. In this chapter, we introduce the fabrication of these hybrid nanowire devices and setups for experiments.

3.1 InSb and InAs Nanowires

High-quality materials are an essential part of quantum transport studies. Collaborators working on materials science are able to provide semiconductor nanowires for our experimental purposes. This is not a thesis for materials science, but I would like to give a basic introduction of the materials involved in my experiments. It will be helpful for understanding device fabrication.

In general, a semiconductor nanowire is a semiconductor nanostructure with a large aspect ratio. A three-dimensional bulk semiconductor is commonly used in experiments and industries [64]; however, two-dimensional or one-dimensional materials are developed for interesting physical properties. For example, two-dimensional electron gas (2DEG) defined in the GaAs/AlGaAs structure [65] can be used to generate pure spin current or lateral devices based on Fe/GaAs heterostructures can be used to study spin transport [66]. For MBS experiments, we need

materials to physically realize a quantum wire and a semiconductor nanowire is naturally a material that satisfies the purpose for an MBS device.

The two types of semiconductor nanowires used in my experiments are InSb and InAs nanowires. First, we introduce the InSb nanowires. In Figure 3.1, SEM images of InSb nanowires grown by metal−organic vapor phase epitaxy (MOVPE) are shown. To grow these InSb nanowires, arrays of gold islands are formed on an InP substrate. InSb is grown by a process of stacking materials. We can see from Figure 3.1 (b) that an InSb nanowire has an InP-InAs stem. The length of the InSb nanowire can be longer than 3 μm and the diameter can be smaller than 200 nm, resulting in a large aspect ratio. For more details of the material, readers may check reference [67]. Efforts have been made to improve the growth of InSb nanowires. For example, the InSb nanowires can be grown without a stem and the length can be tens of microns [68].

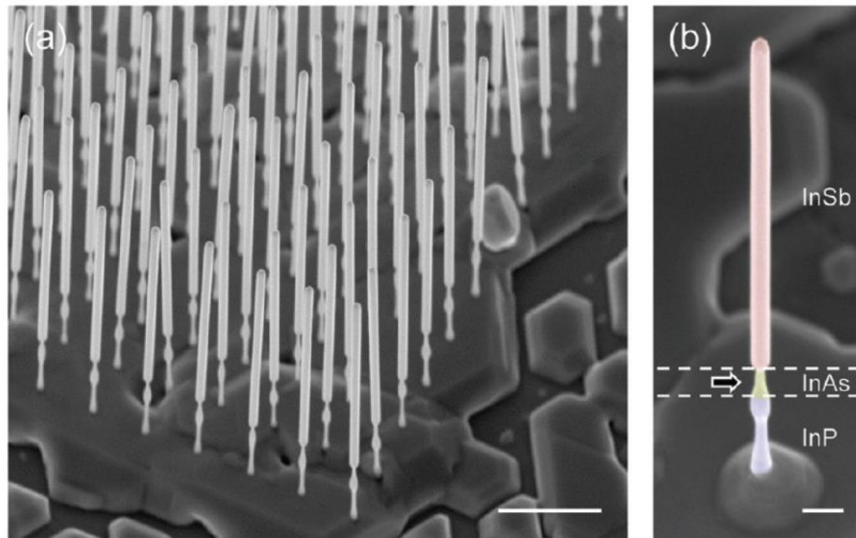

Figure 3.1. SEM images of InSb nanowires adapted with permission from [67]. Copyright {2012} American Chemical Society. (a) An array of nanowires. The scale bar represents 1 μm. (b) Image of a single nanowire. The scale bar represents 200 nm. The arrow indicates the zone of evaporated InAs stem.

Since their aspect ratio is large, InSb nanowires can be thought of as one-dimensional or quasi-one-dimensional. These nanowires also have desirable physical properties: high electron mobility, large *g* factor, strong spin-orbit interaction and small bandgap. Mobilities are reported from 2.0×10^4 to 3.5×10^4 $cm^2\ V^{-1}\ s^{-1}$ for nanowires with a stem [67] and 3.4×10^4 to 5.7×10^4 $cm^2\ V^{-1}\ s^{-1}$ for stemless nanowires [68]. Quantized conductance at finite applied magnetic fields is reported in transport measurements of InSb nanowires and the extracted Landé *g* factors are around 55 [69]. A large Rashba spin-orbit strength (α_R) of 0.5–1 $eV \cdot A$ is reported from magnetoconductance measurements [70]. The small bandgap also makes the InSb nanowires a suitable platform to define hole quantum dots [40]. The above parameters of InSb nanowires may differ or be reported in a wider range [71, 72]. Readers may be careful about the reported values based on their methods to extract corresponding parameters [73]. InAs nanowires have similar properties to InSb nanowires. They are also materials with high electron mobility, large *g* factor, strong spin-orbit interaction and small bandgap [74-78].

Efforts are made to improve the growth of InSb and InAs nanowires. Epitaxy superconductor contacts to nanowires are developed [79, 80]. More advanced techniques are developed to form shadow junctions in situ [81, 82]. S-N or S-N-S junctions are formed in situ by shadowing a section of a nanowire with a nano-flake (Figure 3.2 (a)) or with another nanowire (Figure 3.2 (b)). This shadow technique importantly reduces the effort of device fabrication in terms of forming contacts to a nanowire. We can simply deposit metal leads to the pre-formed superconductors.

Besides InSb and InAs nanowires, the search for other promising materials for MBSs or other quantum states continues to provide us insights. For those interested in the development of

nanowires, especially as platforms for quantum computation, these references may be useful: Refs. [41, 73, 83].

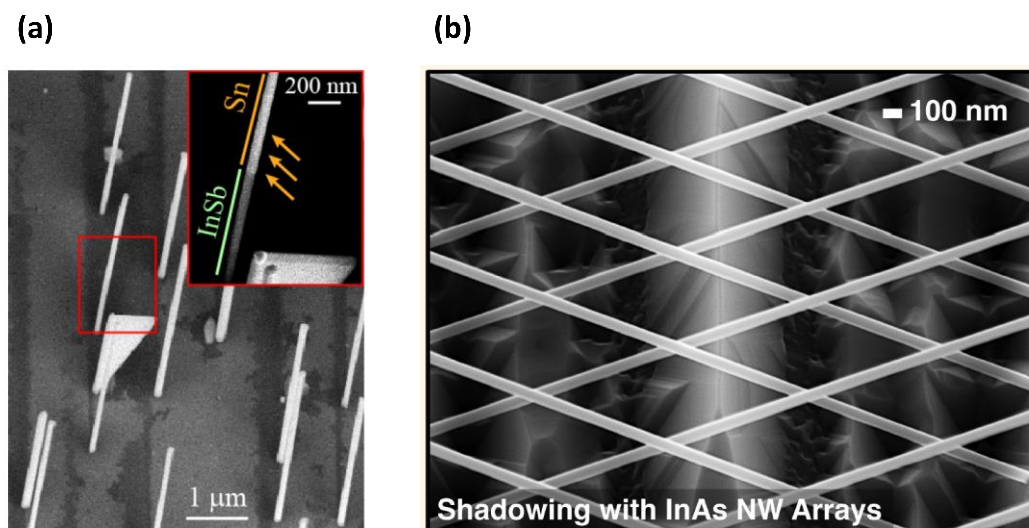

Figure 3.2. SEM images of nanowires grown with a shadow technique. (a) InSb nanowires are shadowed by nano-flakes during the deposition of Sn. A S-N junction is formed in situ. The figure is adapted from [81]. Reprinted with permission from AAAS. (b) InAs nanowire arrays for a shadow technique. Two nanowires form a cross and therefore, deposition of a superconductor can be shadowed for a proper deposition direction. S-N-S junctions are formed in situ. This figure is adapted with permission from [82]. Copyright {2020} American Chemical Society.

3.2 Device Fabrication Based on Nanowires

The fabrication of devices from nanowires requires techniques including typical nanofabrication processes in a clean room. This section is intended to give a general instruction of

my fabrication processes. The fabrication technique is not limited to devices based on InSb or InAs nanowires and the general ideas may be suitable for different types of devices. Detailed recipes are also available for some fabrication processes in Appendix A.

3.2.1 Gate Chips

In order to create a device, a nanowire is placed on a substrate. In Chapter 2, we discuss the use of electrostatic gates to control the chemical potential of a nanowire. Therefore, it is preferred to use a gate chip as the substrate. A typical electrostatic gate is a metal, or a doped semiconductor covered with a dielectric layer. In this thesis, a gate chip is a substrate which has electrostatic gates incorporated onto it. A highly doped silicon wafer with a layer of thermal SiO_2, for example, is naturally a gate chip. In my experiments, this large wafer is cut into small pieces of gate chips. This gate chip can be improved by deposition of a thin layer (about 10 nm) of HfO_x. Compared to SiO_2, HfO_x is more resistant to some chemicals used in the fabrication processes. Moreover, HfO_x has a larger dielectric constant. For the simple model of a parallel plate capacitor with an oxide insulator, the capacitance C is given by:

$$C = \frac{\kappa \varepsilon_0 A}{t} \tag{3.1}$$

where κ is the relative dielectric constant of the oxide, A the capacitor's area, ε_0 is the permittivity of free space and t is the thickness of the oxide. As a high-κ oxide insulator, HfO_x has a larger capacitance than SiO_2 of the same thickness. For the case of local gates (local gates are introduced in the next paragraph), the performance of the device can be enhanced [84, 85]. The schematics of

these two gate chips are given in Figure 3.3. I call this kind of gate chip “global back-gate chip”, since the gate is defined everywhere on the chip.

Instead of the global bake-gate chip, sometimes, a local back-gate chip may be preferred. On a local back-gate chip, gates are defined locally at some specific positions. Using these local gates may lead to better control of the chemical potential. A large local gate is shown in Figure 3.4. It has a rectangular shape and is composed of stacking layers Ti/Au and HfO_x. Only the section of a nanowire within the rectangle can be tuned by the local gate. More advanced local gates can be defined and an example of the gates is shown in Figure 3.5. This advanced gate design enables fine tuning of chemical potentials and different sections of the nanowire can have different chemical potentials. This is very useful to define quantum dots.

To prepare a back-gate chip, metals and oxide insulator layers are deposited onto either a highly doped or undoped silicon wafer with a layer of thermal SiO_2. Large leads and markers are defined on the gate chip for further device fabrication. These techniques are introduced in the following subsections.

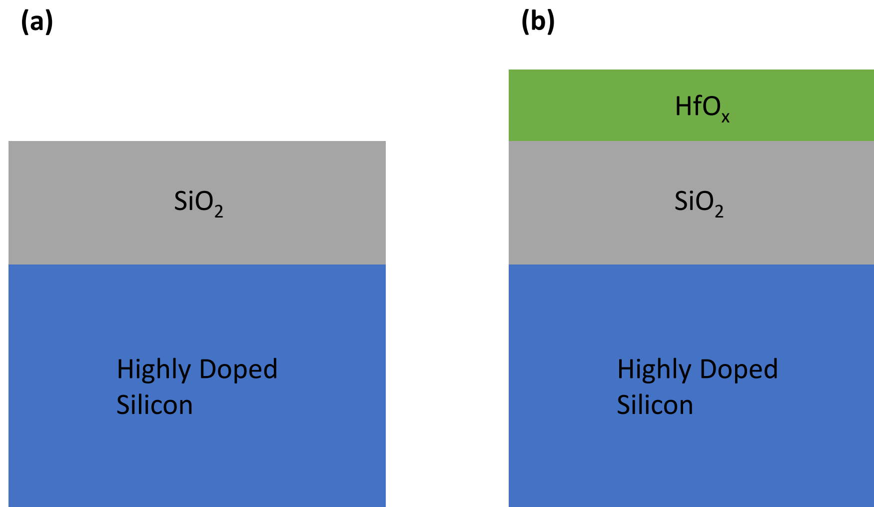

Figure 3.3. Schematic of the cross section for two types of global back-gate chip. The figures are not on scale.

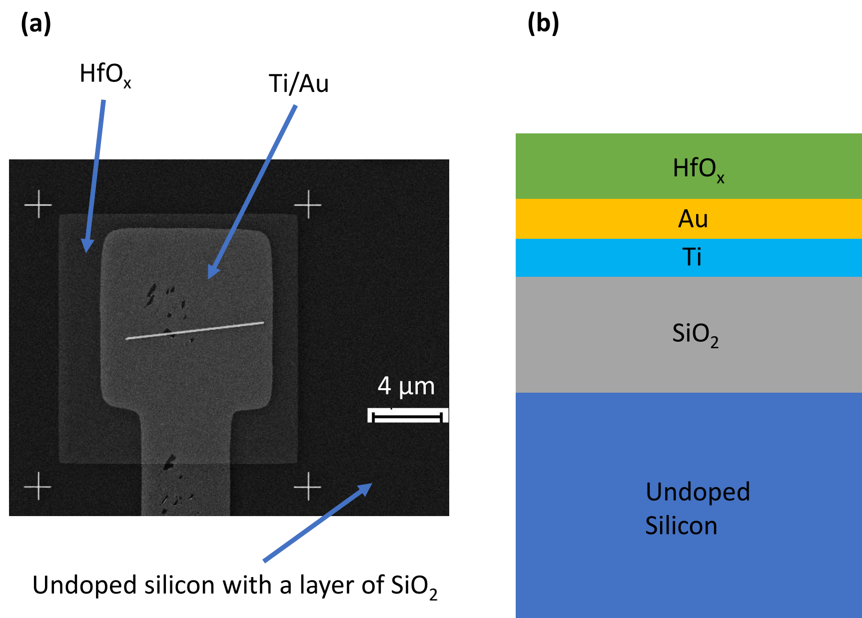

Figure 3.4. A nanowire placed on a rectangular local back gate. (a) An SEM image of the local back gate. A layer of HfO_x is covered on a layer of Ti/Au. Undoped silicon substrate with a layer of SiO_2 underneath. (b) Schematic of the cross section for the local gate. The figure is not on scale.

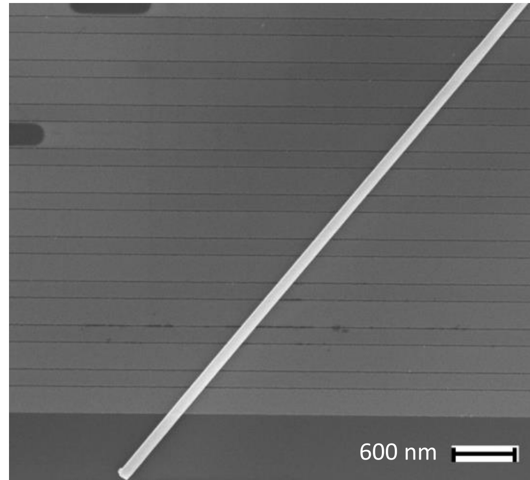

Figure 3.5. A nanowire placed on more advanced local back gates. There are alternating wide and narrow rectangular fine gates designed on the substrate.

3.2.2 Thin Film Deposition

Deposition of thin films is an important part of nanofabrication. For example, to prepare a back-gate chip, layers of Ti, Au or HfO_x need to be deposited onto a substrate. The deposition techniques differ for different materials to be deposited.

For metals like Ti an Au, they can be deposited by sputtering or electron beam (e-beam) evaporation. In our lab, sputtering or e-beam evaporation can be performed in an AJA ATC SERIES UHV HYBRID Sputter/Evaporation system or a Plassys Electron Beam Evaporation system, respectively. For sputtering, the deposition is achieved by sputtering from a material target by Ar plasma. The deposition is not directional. For e-beam evaporation, electron beam "melt" the desired material and evaporates the material to the substrate. This deposition is directional.

The common deposition direction of e-beam evaporation is perpendicular to the substrate, as shown in Figure 3.6 (a). Sometimes, a deposition direction with an angle other than 90° is

preferred. This can be done by loading the substrate with a tilt angle, as shown in Figure 3.6 (b). Thicker metal coating may cause stronger stress at the interface between the metal and the coated object. For a nanowire, the stress may peel off the nanowire from the substrate. Therefore, it may be beneficial to deposit thinner metal by using the technique of deposition with an angle. The thickness of the deposited metal needs to be larger enough to cover the nanowire. Angle deposition can reduce the required thickness. Figure 3.7 shows an example of using the technique.

To deposit thin oxide films like HfO_x, atomic layer deposition (ALD) is used. This technique allows deposition of uniform and conformal thin oxide layers [86]. In our lab, ALD processes are performed in an Ultratech Fiji Atomic Layer Deposition system.

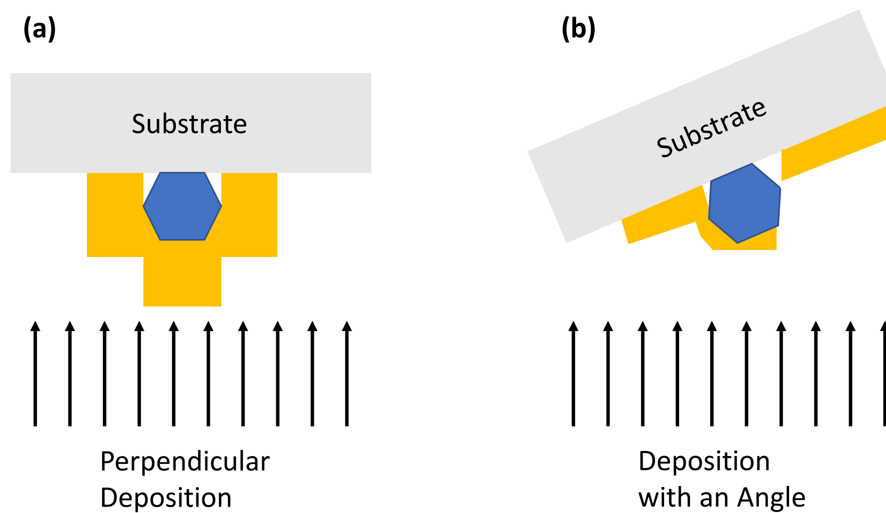

Figure 3.6. Schematics of e-beam deposition for a hexagonal nanowire. The arrows indicate the direction of the coming evaporated materials. (a) Common perpendicular deposition. (b) Deposition with an angle other than 90°.

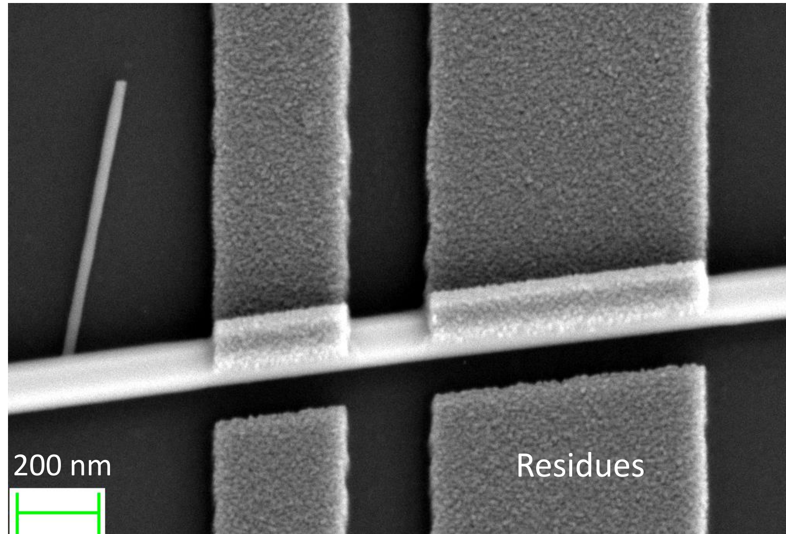

Figure 3.7. Deposition of metal onto a nanowire placed on a substrate. The technique of deposition with an angle is applied. The thickness of the metal can be smaller than the thickness of the nanowire by using this technique.

3.2.3 Lithography

In many situations, materials need to be deposited on specific locations of the substrate. To define small local windows for deposition purposes, lithography is used. There are two types of lithography techniques available in our lab: electron beam lithography and photolithography. I will introduce the procedures of the lithography technique.

In general, for lithography, a resist is coated onto a substrate. The resist can be sensitive to electron beams (electron beam resist) or UV light (photoresist). After being exposed with electron beams or light, the properties of exposed resist are changed so that it can be dissolved in specific solutions (this process is called developing). For a substrate covered with resist, by defining the windows to be exposed, we can deposit materials onto specific locations of the substrate after developing.

The process is explained in Figure 3.8. First, a resist is spin-coated onto a substrate. Sometimes, multilayers of different types of resists are spin-coated. Different resists react differently with the same dose of electron beam or light, resulting in a more complicated cross-section of the developed resist. After the spin-coating, the substrate is loaded into lithographic equipment for exposing it with electron beams or light. In our lab, a Raith e-LiNE Electron Beam Lithography system is used for e-beam exposing and a Heidelberg MLA100 Direct Write Lithographer system is used for light exposure. Both systems can locate the desired section of the substrate to write windows. The e-Line system has better locating precision and writing resolution. The MLA system has lower precision and resolution; however, the writing speed is much larger than the e-Line system. It is preferred to use photolithography for defining large windows, for example, large leads on a gate chip. For small windows requiring higher precision and resolution, for example, leads and contacts to a nanowire, e-beam lithography is necessary. For complicated designs of windows like the fine gates shown in Figure 3.5, even the e-LiNE is not capable. A better e-beam lithography system (100 kV Elionix EBL system or better ones) has to be used.

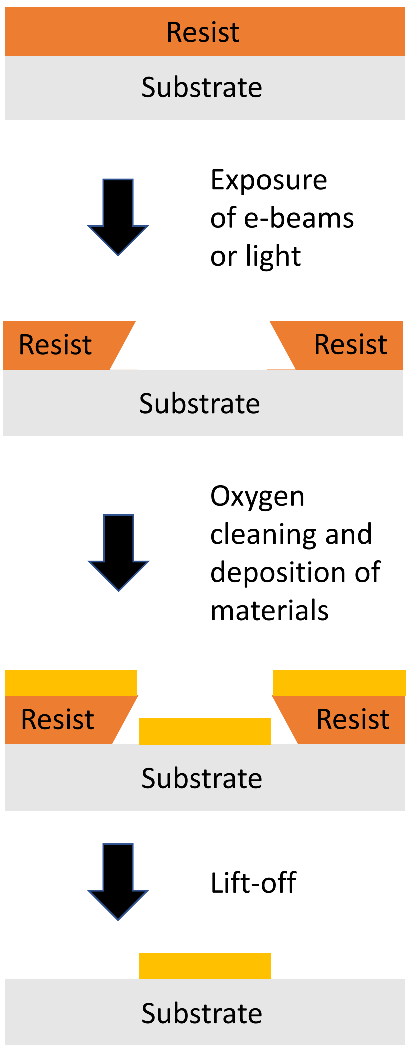

Figure 3.8. Schematic of lithography process for deposition materials on selective locations on a substrate. The figures are not on scale.

After exposure, the sample is put into specific solutions which can dissolve the exposed resists and open windows in the resist. In the windows, resists are supposed to be dissolved in the solution. However, resist or solution residues may exist and further cleaning process is followed to remove the possible residues. This further cleaning process is oxygen plasma cleaning performed in a TRION Phantom Reactive Ion Etching (RIE) Etcher system or a March PX-500

Plasma Asher system. A gentle etching using oxygen plasma may help remove residues without leaving significant damage on the sample.

Metals or other materials can be deposited onto the chip. After deposition, a lift-off process is performed where the sample is put into solvents that can dissolve resists even without exposure to e-beam or light. Deposited materials covered on the resists are peeled off from the substrate and the materials attached on the windows without resists left after developing. This finishes the overall lithography process to deposit materials onto selective locations on a substrate.

3.2.4 Processing of Nanowires

Nanowires are grown on a growth chip and they need to be transferred to a gate chip. The transfer is accomplished by using a thin probe tip under an optical microscope (OP). A nanowire can attach on the tip due to the Van der Waals force. The picked nanowire on the tip can be transferred to the substrate because the Van der Waals force can be stronger between the surface of the gate-chip and the nanowire with the wire lying flat.

A gate-chip is prepared with large leads and markers which are shown in Figure 3.9. A nanowire is placed onto locations close to markers and imaged with a SEM. Leads, contacts and other components can be designed using CAD software. With imaging of the nanowire with markers, coordinate systems can be established for alignment of the real sample with design patterns loaded into a lithography system.

Nanowires typically have a native grown oxide layer, or an oxide layer is deposited intentionally to protect the nanowire from oxidation. To make transparent ohmic contacts, metals need to be directly attached to the semiconductor without oxide. The oxide layer insulates the

nanowire from the metals and destroys the conductivity. To resolve this, this oxide layer needs to be etched away or processed.

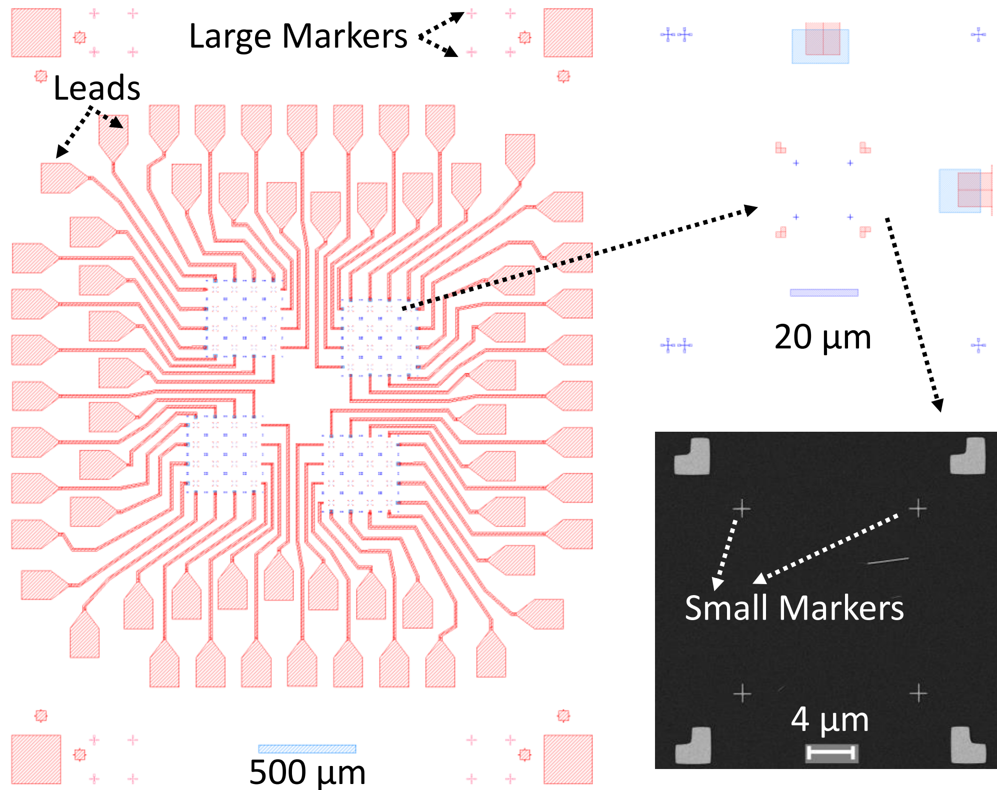

Figure 3.9. Design of gate chips with leads and markers. The upper small picture gives the enlarged format of the small area indicated by an arrow. The lower small picture gives an SEM image of the enlarged area. Leads, large and small markers are also indicated by arrows.

For InSb nanowire with a naturally grown oxide layer, a sulfur passivation process is performed to form transparent ohmic contacts. Before deposition of metals, a sample is immersed into ammonium polysulfide, $(NH_4)_2S_x$, water solution. Nanowire sections in resist windows formed after developing can be etched chemically and passivated by the solution. Outside the

windows, resist can protect the sample, including the gate oxide from etching, especially when there is a not layer of HfO_x. From my experience, HfO_x is not etched by ammonium polysulfide water solution. The sulfur passivation process also works to process InAs nanowires [87].

There are other types of etching that can be performed. The Plassys e-beam evaporation system can perform Ar etching in situ to remove oxide layers. During the etching process, Ar ions bombard the surface of a nanowire and mill oxide layers away. Compared to sulfur passivation, this Ar etching is more destructive to the material but is more universal. The sulfur passivation process does not work for many oxides other than the native oxides on InSb or InAs nanowires. In contrast, Ar etching is a physical process that can just mill material away. However, the destructive nature of Ar milling may be harmful to a device. If the purpose of the contact is for proximity of, for example, superconductivity, the proximity may be destroyed by the Ar etching. For simply creating electrodes without care for the metal-semiconductor interface, Ar etching is a convenient method to be considered.

An oxide layer is not the only segment that we may need to remove. To fabricate structures like S-N junctions, we need to remove a portion of superconductors from nanowires with superconductor shells (nanowires shown in Figure 3.2). Ar etching can mill superconductor layers away but the etching time is hard to control, since InAs itself can be milled by Ar ions. Luckily, for InAs nanowire grown with a superconducting Al layer, the Al layer (also AlO_x) can be dissolved in an alkaline solution commonly used for developing photoresists, without observable destruction to InAs or gate-chips.

3.3 Measurement Setups

3.3.1 Dilution Refrigerators

A common superconductor needs a low temperature to be superconducting. For Al, transition temperature lower than 1.2 K is recorded and for Sn, transition temperature lower than 3.72 K is recorded [88]. Since experiments discussed in this thesis need superconducting proximity effects, devices need to be studied at low temperature. For the theoretical models introduced above, temperature considered is typically zero. Furthermore, at finite temperature, a system may go into an excited state or occupy a thermal mixture of states. Thanks to the technologies developed, we may perform experiments at very low temperature.

In this thesis, data are acquired using two Leiden Cryogenics dilution refrigerators. A dilution refrigerator is a system that can support a very low temperature (tens of mK) environment. After condensation of mixture of ^{3}He and ^{4}He and several hours of circulation, the base temperature of the dilution refrigerators can reach lower than 50 mK with devices inside. One of the refrigerators is installed with 2D superconducting magnets so that two-dimensional magnetic fields can be applied. Another refrigerator is installed with 3D superconducting magnets and three-dimensional magnetic fields are applicable. For sweeping to finite magnetic fields, the temperature inside the fridge may increase. In my experiments, typical magnetic fields are less than 0.2 T, where the increment of temperature is typically within 10 mK.

For loading devices, a chip with devices is pasted onto a chip carrier by silver paste. The chip carrier has pins bonded with leads of the devices using a wire bonder. The chip carrier is loaded onto a probe which can be inserted into the dilution refrigerators. The probe has cables

which can be connected outside the refrigerators to send out signals from devices or receive signals from outside sources. A dilution refrigerator and a probe are shown in Figure 3.10.

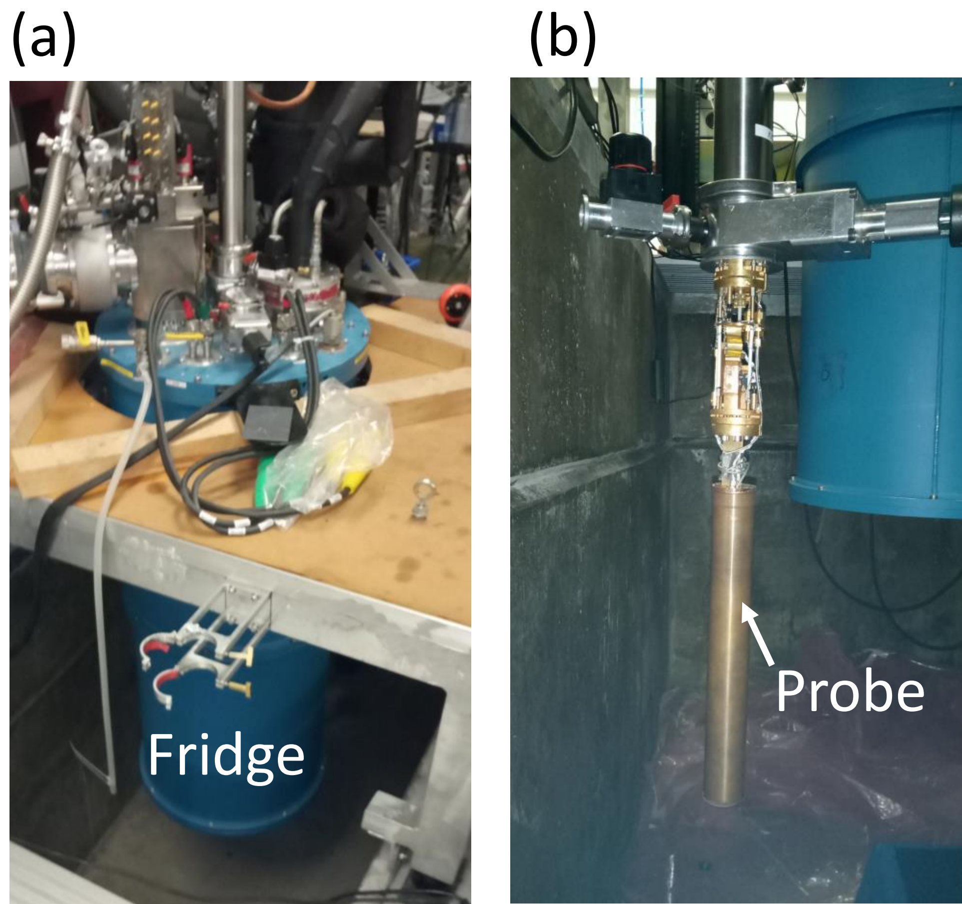

Figure 3.10. (a) A dilution refrigerator. (b) A probe used to load a chip with devices.

3.3.2 Measurement System

Electrical signals are applied and measured by a measurement system built at the Delft University of Technology [89]. The system has a Matrix rack and an IVVI rack, as shown in Figure 3.11. The Matrix rack has pins connected to the probe for circuit wiring. The IVVI rack provides different electric sources and measurement modules providing different amplifications. The IVVI

rack is powered by batteries and controlled by a computer via optical fiber. This highly reduces the influence from the outside environment, for example, possible noise from a common electrical outlet. An output bias from the IVVI is direct current (DC) or alternating current (AC) if an AC lock-in signal is added. Sometimes, AC bias is used by connecting the IVVI rack with a lock-in amplifier. The lock-in technique can be considered as an amplifier with a notch filter around the lock-in frequency, which picks out signals from noisy backgrounds. A Python-based measurement software, QTLab [90], is used to send measurement commands and collect data from a PC.

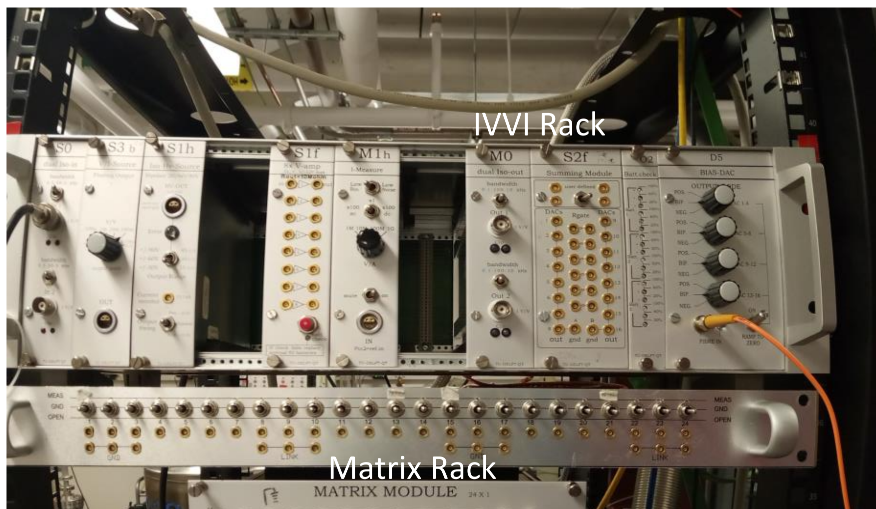

Figure 3.11. Racks of the measurement system: matrix rack and IVVI rack

3.3.3 More about Measurement Setup

The conductance or resistance of a device can be measured by appropriate circuit wiring of a voltage/current source and current/voltage measurement instruments. The detection of quantum states in hybrid semiconductor nanowire devices or quantum dots can be achieved by acquiring the differential conductance or resistance of a device. For example, a metal lead weakly

coupled to a quantum dot has a density of states (DOS). The DOS of a metal lead can be considered as a constant since there are a huge number of electrons on the lead compared to a quantum dot. Therefore, the change of detected signals should mainly come from the change of the DOS on the quantum dot. We visualize this change by acquiring the differential conductance or resistance to present quantum states inside a device.

It should be noticed that the conductance or resistance of a device does not contribute to the total impedance or admittance of a measurement circuit. Therefore, it is important to realize the impedance or admittance of components other than the desired object to be measured. This additional impedance or admittance may come from different origins. The wires for bonding a chip onto a chip carrier or cables for wiring the measurement circuit can have finite resistance. Metal contacts themselves may have finite resistance. The amplifiers of the IVVI may have finite resistance. Additionally, for reducing noises, RC filters with finite resistance may be installed on the probe. To determine the input resistance, we may short two pins of a device inside a refrigerator from the Matrix rack and measure the resistance. This measured resistance is about the overall input resistance but the contact resistance is not included. Unfortunately, contact resistance highly depends on different devices and it is difficult to determine. For a particular device, if there is measured quantized conductance, people may be able to extract the contact resistance by correction from the quantized plateaus [69].

With the knowledge of input resistance, the conductance or resistance of a device can be extracted. As an example, a setup of simple two-terminal measurement is shown in Figure 3.12. A voltage source is connected to the device and a current-measure (I-measure) is connected in series with device resistance (R_{device}) and input resistance (R_{in}). Suppose the amplification of voltage source is a_V and the amplification of the ammeter is a_I, then it is clear that:

$$a_V V = a_I I R_{device} + a_I I R_{in} \tag{3.2}$$

where V is voltage applied by the voltage source, I the current measured by the ammeter. If we take the differential conductance, the conductance of the device, G_{device}, is:

$$G_{device} = \frac{G}{a - G R_{in}}, \qquad a = \frac{a_V}{a_I}, \qquad G = \frac{dI}{dV} \tag{3.3}$$

Experimentally, for this setup, we set the values of V and measure the values of I. For a DC voltage source, we acquire G by taking a numerical derivative of measured currents. By extracting the input resistance using equation (3.2), the value of the device conductance is determined. Notice that if we use the lock-in technique, the measured value from the lock-in is already conductance. Similarly, if we adjust the setup in Figure 3.12 and apply current bias, we can extract the resistance of the device by taking the differential resistance:

$$R_{device} = aR - R_{in}, \qquad R = \frac{dV}{dI} \tag{3.4}$$

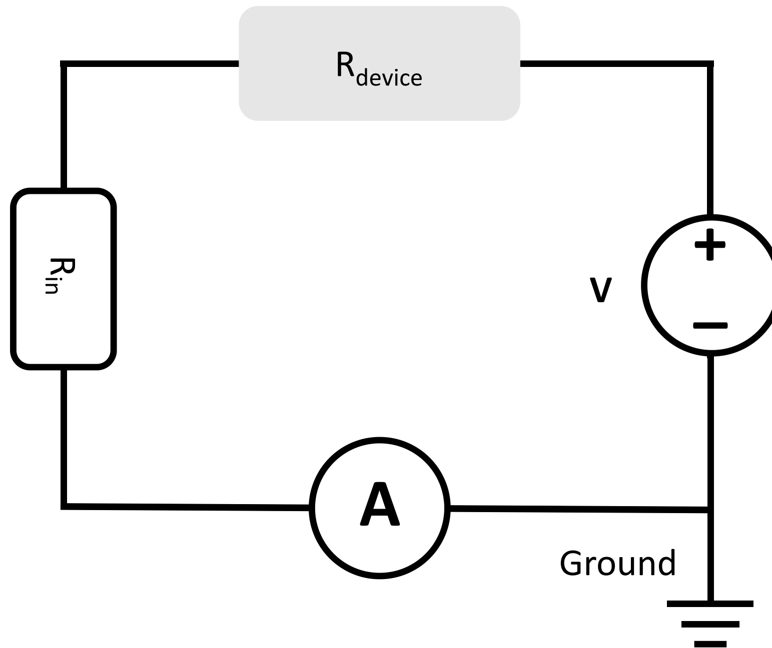

Figure 3.12. A two-terminal measurement circuit. Voltage *V* is applied to the device, R_{device}, by a voltage source. An ammeter (I-measure) is connected in series. R_{in} represents the overall input resistance.

Sometimes, we may use a four-terminal setup as described in Figure 3.13 for measurement of nanowire devices. In this measurement setup, for the left segment of the nanowire, a voltage source is used to apply voltage to the nanowire and an ammeter is used to measure the current as the two-terminal case. For this part, we call it local measurement. Additionally, we also monitor the voltage across the right segment of the nanowire and we call this non-local measurement. The purpose of this four-terminal setup will be discussed in Chapter 4.

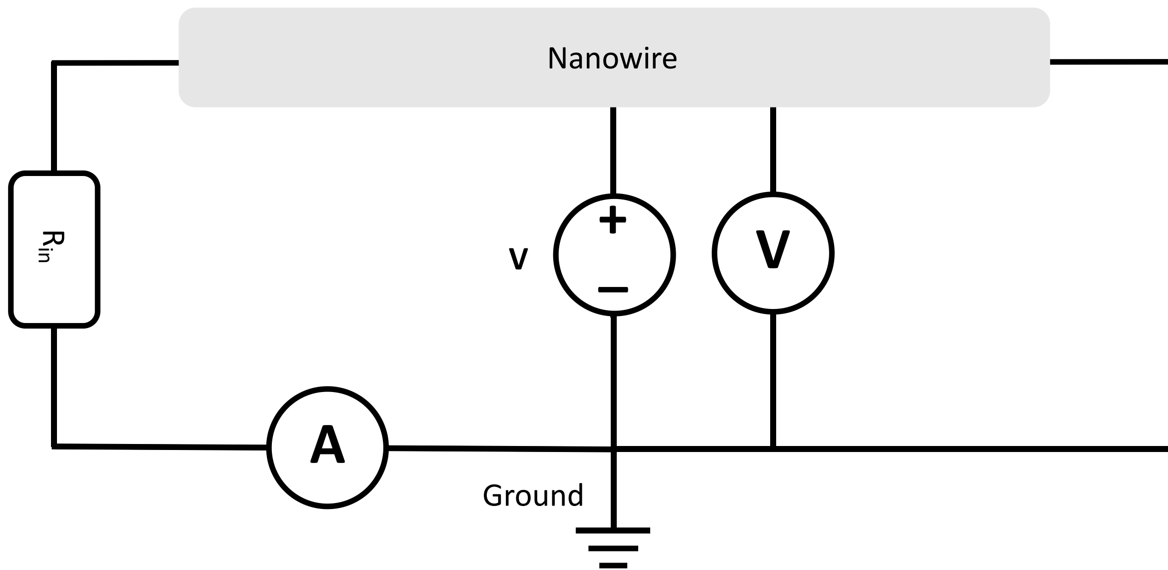

Figure 3.13. A four-terminal measurement circuit. *V* is applied to the left section of a nanowire by a voltage source. An ammeter is connected in series. R_{in} represents the overall input resistance. Additionally, a voltmeter is connected across the right section of the nanowire to monitor the corresponding voltage.

4.0 Local Magnetic Field Effect in InSb Nanowire Devices

Ferromagnetic components can be integrated into a semiconductor nanowire device with different methods. Ferromagnetic contacts can be formed to semiconductors. In this case, ferromagnetic contacts may inject spin-polarized current into a semiconductor and spin transport may be studied in this platform [15, 66, 91-96]. On the other hand, without forming contacts, ferromagnetic components can be used as magnets which provide stray fields for a semiconductor device [97-103]. In this chapter, we discuss experiments for understanding the effect from ferromagnetic components in InSb or InAs nanowire devices. The main topic of this chapter has been published [104] and the corresponding authors are Y. Jiang, E.J. de Jong, V. van de Sande, S. Gazibegovic, G. Badawy, E.P.A.M. Bakkers, S.M. Frolov. © IOP Publishing. Reproduced with permission. All rights reserved.

4.1 Ferromagnetic Materials

Ferromagnetic materials have interesting properties under magnetic fields. A prominent property is magnetization of ferromagnets under applied magnetic fields. The magnetization of a ferromagnet, m_h, depends on the history of how the magnetic field is applied. This results in a hysteresis loop conceptually shown in Figure 4.1. The magnetization direction of a ferromagnet does not switch immediately by the change of the direction of the applied magnetic field. A coercive field needs to be reached for switching of magnetization direction due to the hysteresis.

Magnetized ferromagnetic materials are magnets, which can produce magnetic fields. We call these generated magnetic fields stray fields. Magnetization determines the profile of stray fields. For a ferromagnetic material under external magnetic fields, the produced stray fields may switch their direction if the magnetization is switched due to change of external magnetic fields. The switch can be sharp due to the coercive field from the hysteresis. The profile of stray fields is not homogenous in space. In general, we can expect that an object may feel stronger stray fields if it is placed closer to a magnetized ferromagnet (not always, of course). For a uniaxial bar magnet, there is an analytical solution that the stray fields can be deduced from the Maxwell equations [105]. Unfortunately, in the corners of the cuboid the analytical solution is not defined. Common ferromagnetic materials include Ni, Fe, Co, and their alloys; for more properties about ferromagnets, readers may check this reference [106].

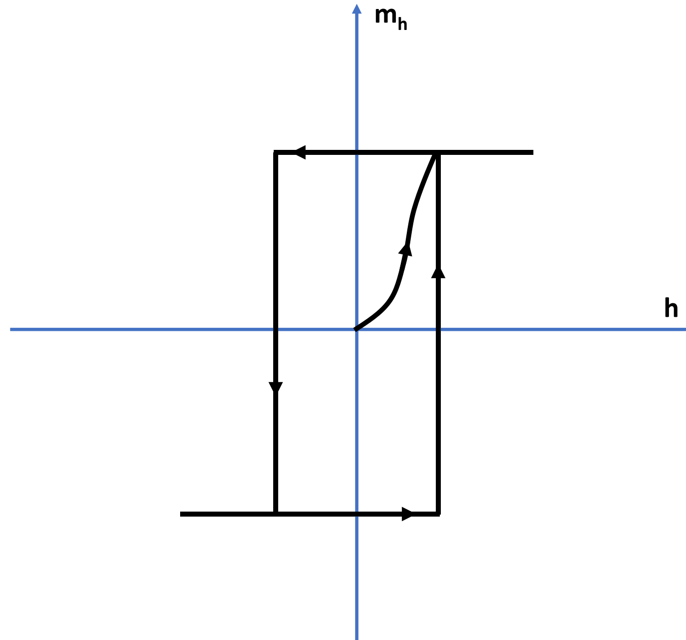

Figure 4.1. Hysteresis loop of a ferromagnetic material. *h* is the applied magnetic field and m_h is the magnetization of the material. The schematic is conceptual and for a real material, the loop may be different.

Ferromagnetic contacts may introduce novel properties to a semiconductor device. The relevant property in this thesis is spin injection from ferromagnetic contacts. Spin injection is not limited to semiconductors, but it is a common mechanism when a ferromagnetic contact forms to a non-ferromagnetic material. After magnetization, the ferromagnetic contacts can be considered as spin injectors and spin filters. Free electrons can be spin-up or spin-down at the same energy but for a magnetized ferromagnet, specific spin direction is preferred. This allows injection and detection of spin-polarized current. Electrical spin injection and detection in a spin-valve device where spin-polarized current is developed are based on this property [107].

A spin-valve is described in Figure 4.2. For a two-terminal setup shown in Figure 3.12, a non-ferromagnetic material has two ferromagnetic contacts. The dimensions of these two

ferromagnetic contacts are different for having different coercivity. By sweeping the magnetic field, the magnetization directions of the two ferromagnetic contacts can have two different states. The first state is that the two contacts are magnetized in the same direction (in-parallel) and for the second state, the two contacts have antiparallel magnetization directions. For the in-parallel state, a contact injects spin-polarized current while the second contact prefers this spin-polarization. If the device is in the antiparallel state, the second contact prefers the reversed spin-polarization of the injected spin-polarized current. Thus, at the antiparallel state, the measured resistance should be higher than the measured resistance in the in-parallel state. When the applied magnetic field is larger than the coercive field of one contact but is still smaller than the conceive field of another contact, the antiparallel state is accessible. It is also possible to fabricate a four-terminal spin valve device with two ferromagnetic contacts and two normal metal contacts. The two normal contacts are located at the two ends of the device and the two ferromagnetic contacts are located in the middle. Spin-polarized current is injected through one of the ferromagnetic contacts and another ferromagnetic contact can be used to monitor spin-polarized current non-locally. We will see this four-terminal measurement later in this chapter.

A spin-valve enables electrical injection and detection of spin-polarized current and becomes an important concept in the field of spintronics [108, 109]. InSb and InAs nanowires have strong spin-orbit interaction which is beneficial for modulation of spins. They are candidates for spin-based devices like modulators [110] but within my knowledge, it is still difficult to successfully demonstrate spin injection into an InSb or InAs nanowire up till now. Efforts can be found in [111, 112]

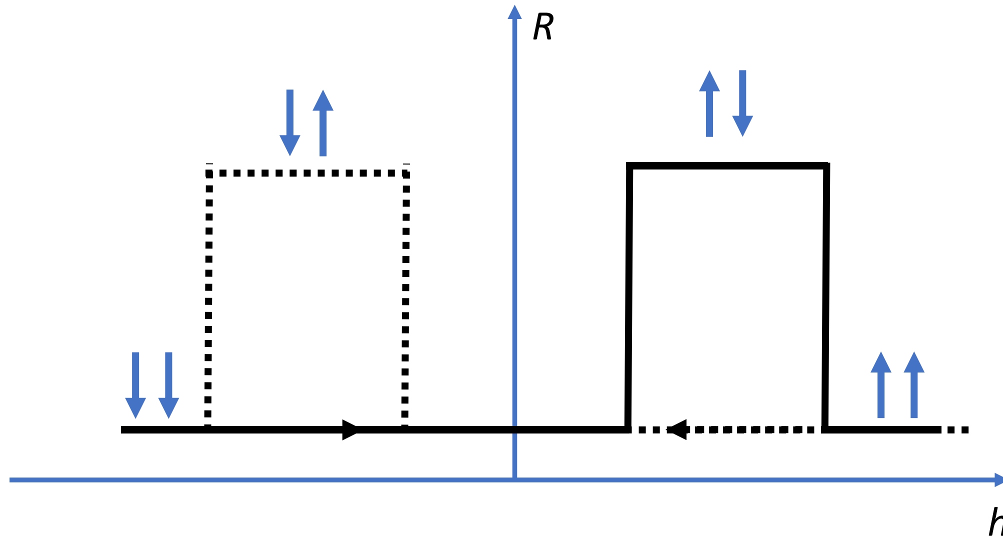

Figure 4.2. Schematic of spin-valve. *h* is a magnetic field and *R* is the resistance of the spin-valve device. The arrows indicate the magnetization directions of two ferromagnetic contacts of the device.

4.2 Ferromagnetic Contacts to InSb Nanowires

A simple InSb nanowire device can be fabricated by deposition of two ferromagnetic contacts with different dimensions. This two-terminal device has the structure of a spin-valve device and therefore we may expect spin-polarized current observed in this kind of device. The first effort is to fabricate conducting ferromagnetic contacts to an InSb nanowire.

In our lab, available ferromagnetic materials for deposition are Ni, Co and CoFeB (atomic ratio: 30/55/15 before deposition). For my experiments, CoFeB is mainly used since we believe that it is a stronger ferromagnet and has a better switching of magnetization. These metals are

deposited using e-beam evaporation. The atomic ratio of CoFeB cannot be preserved during the evaporation process and the deposited metal is expected to be only CoFe [113].

To fabricate a device, an InSb nanowire is transferred to a back-gate chip. Contacts with different dimensions are designed and written by e-beam lithography. After developing, oxygen plasma cleaning is performed to clean possible residues of e-beam resists or undesired solutions. Before deposition of metals, sulfur passivation is performed to passivate the naturally formed oxide layer covered on the nanowire. The thickness of an InSb nanowire can be more than 100 nm and if we use a common deposition technique, the thickness of deposited CoFe should be larger than 100 nm. Tension from a thick CoFe layer covered on an InSb nanowire causes a trend to peel off the nanowire from the gate chip. To deal with this issue, we use the technique of deposition with an angle. The value of the deposition angle can be adjusted to achieve a good deposition outcome. The common angle I use is about 50° with respect to the chip surface. By this technique, a CoFe layer of 40 nm can be deposited to form contacts and the InSb nanowire remains attached to the gate chip. At this step, two CoFe strips with different dimensions are deposited to a chip without any deposition of leads. Even though it is possible to write windows for CoFe strips and leads together, serious lift-off issues will damage the device due to the technique of angle deposition. Angle deposition is good to use for deposition of metals to small windows of nanowires arranged in specific orientations. Otherwise, metals are deposited to e-beam resists' window walls for large leads and it becomes difficult to lift-off metals after deposition. A thin layer of Au is deposited after deposition of CoFe to protect CoFe from oxidation. After lift-off, another process of e-beam lithography is performed to write windows for leads connecting the small ferromagnetic contacts. Metals of Ti/Au are deposited for the leads. A typical InSb nanowire after deposition of two CoFe contacts is shown in Figure 4.3.

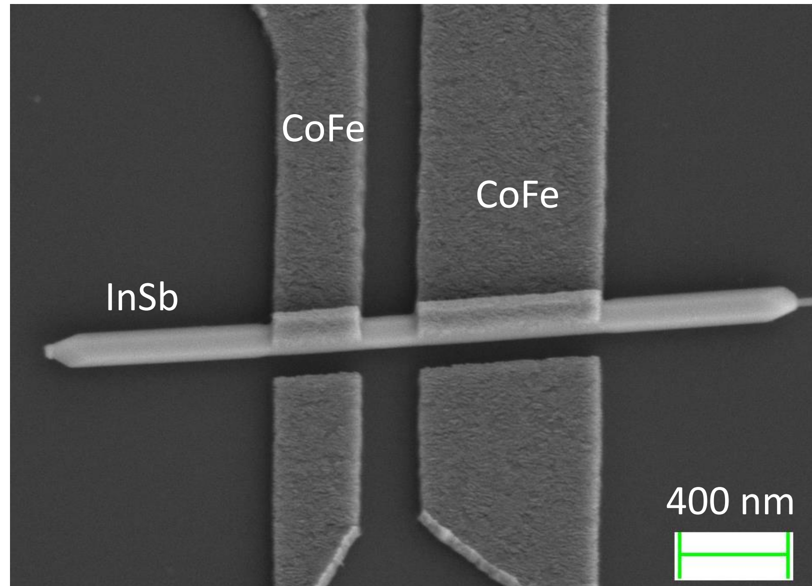

Figure 4.3. An InSb nanowire with two CoFe contacts fabricated by angle deposition. There are residues of CoFe because during the angle deposition, the InSb nanowire can shadow the deposition.

The characterization of an InSb nanowire device is performed at low temperature inside a dilution refrigerator. Without adding any gate voltages, an InSb nanowire device may be conducting or not conducting. If the device is functional, a gate voltage can turn off or turn on a device. By adding a specific bias voltage and sweeping gate, a plot of gate dependence curve is acquired. We call this plot pinch-off curve of a semiconductor device and it is the very first measurement of my experiments discussed in this thesis. A typical pinch-off curve is given in Figure 4.4 (a). Close to pinch-off voltage, the conductance of the device increases suddenly with respect to larger gate voltage. At a gate voltage that the device is conducting and far away from the pinch-off voltage, it is a good practice to sweep bias voltage and check the current's response with voltage bias. This gives an I-V curve as shown in Figure 4.4 (b). In this I-V curve, the relation

between voltage bias and measured current is linear, just like the I-V for a standard resistor. From the I-V curve, we know that the ferromagnetic contacts in the measured device are ohmic, which is desired for my experiments. Ohmic contacts indicate that between the contacts and the nanowire, the transport of electrons is relatively easy. However, even ohmic contacts cannot guarantee the preservation of electron properties from the ferromagnetic contacts to a nanowire. Especially for spin injection, the electron spins from ferromagnetic contacts need to be preserved after transporting into the nanowire. The interface between the ferromagnets and the nanowire may change spin direction of coming electrons. The interface can be an important issue for quantum transport measurement. We believe the sulfur passivation results in the best interface in our experiments on InSb nanowires, unless a contact is grown in situ, which was introduced in section 3.1.

Four-terminal devices are also fabricated. Before deposition of Ti/Au contacts, instead of using sulfur passivation, Ar etching is performed in situ using the Plassys e-beam evaporation system. Ohmic contacts are also preferred for Ti/Au. Ar etching may cause larger damage to the interface between Ti and InSb. Nevertheless, Ti/Au contacts work as leads and the interface is not so important as the case for CoFe contacts.

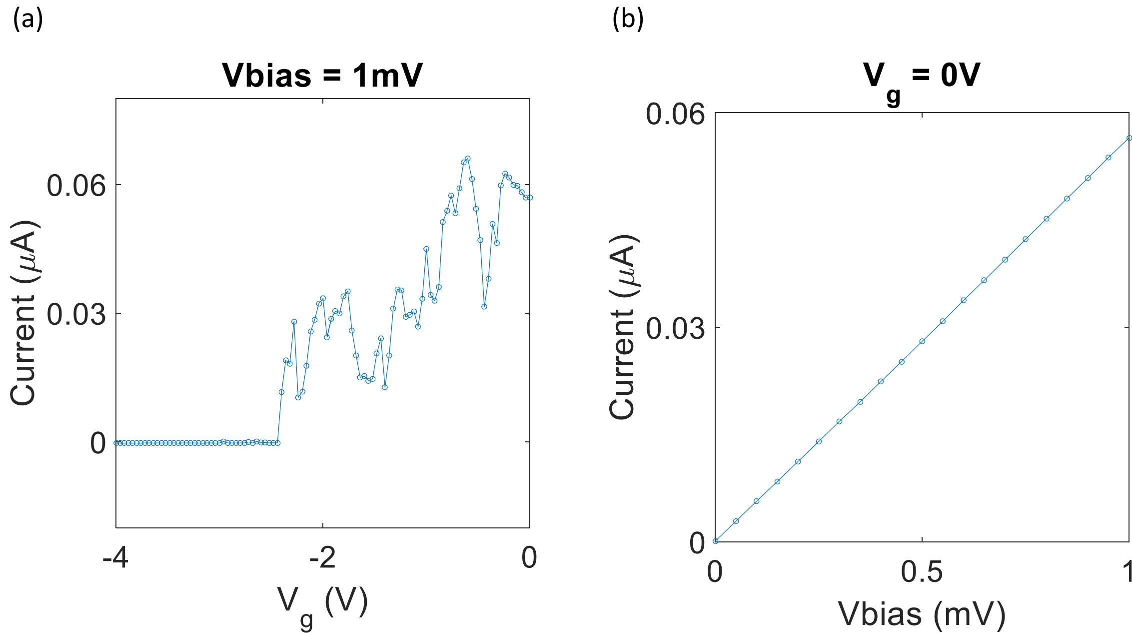

Figure 4.4. Measurement on a two-terminal device. Vbias is the applied bias voltage. V_g is the applied back-gate voltage. Current is measured through a device. (a) Pinch-off curve of an InSb nanowire device with two ferromagnetic contacts. (b) I-V curve of an InSb nanowire device with two ferromagnetic contacts.

4.3 Hysteretic Magnetoresistance in a Device with Ferromagnetic Contacts

We first discuss the situation where ferromagnetic contacts are formed to an InSb nanowire. In this case, we need to consider both spin-injection and stray fields from the ferromagnetic components.

4.3.1 Two-terminal Device without Ferromagnetic Components

Before discussion of hysteretic magnetoresistance in an InSb nanowire device with ferromagnetic contacts, it will be useful to have knowledge on the magnetoresistance of an InSb nanowire without any ferromagnetic components involved. This magnetoresistance can be considered as a "background" for an InSb nanowire device for further experiments.

To measure the background magnetoresistance of an InSb nanowire, a two-terminal device is fabricated as shown in Figure 4.5 (a). An InSb nanowire is placed on a back-gate chip and two Ti/Au contacts are formed to an InSb nanowire. Ti and Au are normal metals (not ferromagnetic), and we call this two-terminal device N-N device. DC measurement is performed at the base temperature inside a dilution refrigerator. Figure 4.5 (b) shows the magnetoresistance of the N-N device in Figure 4.5 (a). The magnetoresistance is basically the same for sweeping magnetic field from -0.2 T to 0.2 T or from 0.2 T to -0.2 T. At zero magnetic field, there is a peak of the measured current, indicating a local minimum of magnetoresistance. It is also possible for a local maximum of magnetoresistance measured at zero magnetic field by adjusting the gate voltage. The magnetoresistance of an InSb nanowire is not flat and may have a variety of features. This is from the strong spin-orbit coupling of InSb which has been studied in other papers [70, 114].

Additionally, the gate dependence and the I-V curve is given in Figure 4.6. Compared to Figure 4.4 (a), this device does not conduct at zero gate voltage, V_g, and the pinch-off voltage is positive. For large positive gate voltage, the measured current does not keep increasing and that seems to be at the saturation region for back-gate tuning. I-V curve is taken at large V_g and it is linear, indicating that the Ti/Au contacts are ohmic.

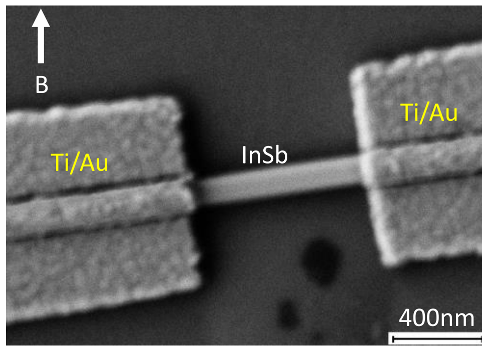

(a)

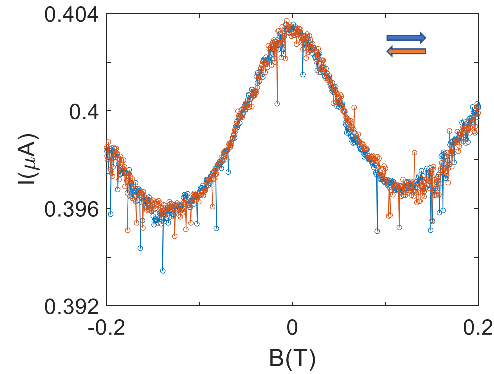

(b)

Figure 4.5. Measurement on an N-N device. (a) Scanning electron microscope image of a device without any ferromagnetic components. (b) Representative magnetic field scan taken at V_{sd} = 5 mV and V_g = 1 V. V_{sd} is the applied bias voltage and V_g is the applied back-gate voltage. Data are acquired by DC measurement. There is no observable hysteresis and the signal is peaked at zero field. The peak width is of order 100 mT. This figure is adapted from [104].

(a)

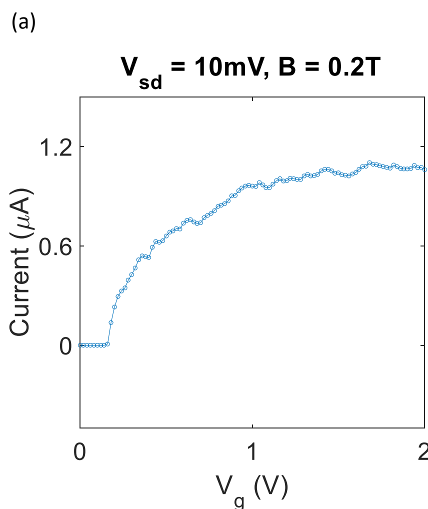

(b)

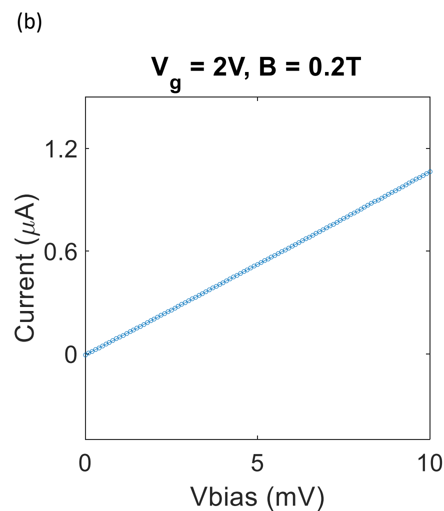

Figure 4.6. Measurement on an N-N device. V_{sd} is the applied bias voltage. V_g is the applied back-gate voltage. *B* is the applied magnetic field. (a) Pinch-off curve. (b) I-V curve.

4.3.2 Two-terminal Device with Ferromagnetic Contacts

A two-terminal device with ferromagnetic contacts is shown in Figure 4.7 (a). An InSb nanowire is placed on a back-gate chip and deposition of CoFe contacts is performed by the angle deposition technique. We call this type of device F-F device. Measurement is performed at the base temperature inside a dilution refrigerator. Figure 4.7 (b) gives the measurement setup.

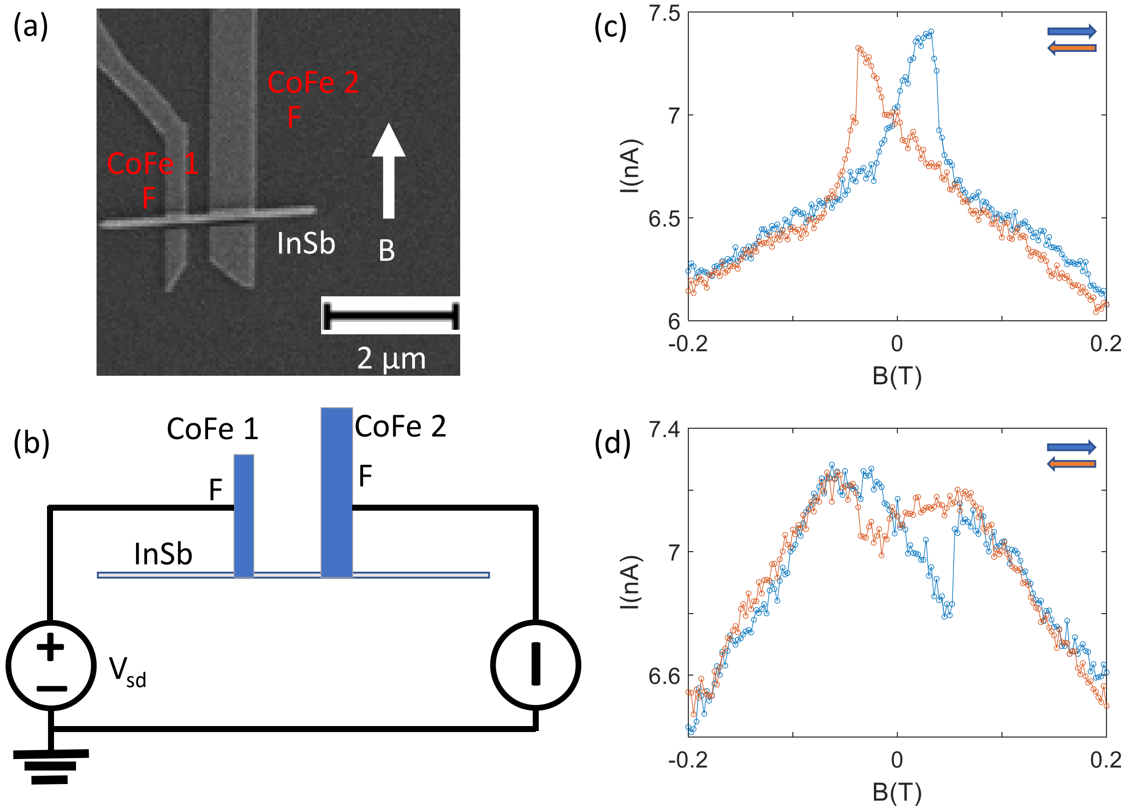

Figure 4.7. (a) Scanning electron microscope (SEM) image of an F-F device. The direction of the applied magnetic field *B* is indicated by arrow. (b) Schematic of measurement setup. All data shown in this figure are acquired by DC measurement. (c) Current as a function of magnetic field taken at V_{sd} = 0.1 mV and V_g = 0 V. (d) Magnetic field scan taken at V_{sd} = 0.1 mV and V_g = 0.08 V. The sign of the hysteresis is reversed compared to panel (c). This figure is adapted from [104].

Magnetoresistance measurement of the F-F device is presented in Figure 4.7 (c) and (d). In Figure 4.7 (c), a magnetic field is swept from -0.2 T to 0.2 T and then back from -0.2 T and 0.2 T. Current through the nanowire is monitored and the corresponding magnetoresistance is easily inferred. Compared to Figure 4.5 (b), the magnetoresistance of an InSb nanowire device with two CoFe contacts is hysteretic, indicating the function from ferromagnetic contacts. Around zero magnetic field, there are two local minimums of magnetoresistance. For a different back-gate voltage as shown in Figure 4.7 (d), the two local minimums are reversed to two local maximums. Recall the spin-valve from section 4.1, magnetoresistance measurement on a F-F device visually demonstrates the feature of spin-injection. Especially for Figure 4.7 (d), the plot shares similar features with Figure 4.2.

Hysteretic magnetoresistance can come from other mechanisms [18, 115]. For further investigation on the possibility of spin-injection into an InSb nanowire, a four-terminal measurement is preferred to isolate spin current from electrical current. This is to be discussed in the following subsection.

4.3.3 Four-terminal Device with Ferromagnetic Contacts

A four-terminal device with ferromagnetic contacts is shown in Figure 4.8 (a) and (b). An InSb nanowire is on a back-gate chip with two ferromagnetic contacts and two normal contacts. Ferromagnetic contacts and normal contacts are all ohmic. We call this type of device N-F-F-N device. This four-terminal setup enables monitoring of local and non-local signals simultaneously. Lock-in technique is used for filtering noises by applying a small AC signal.

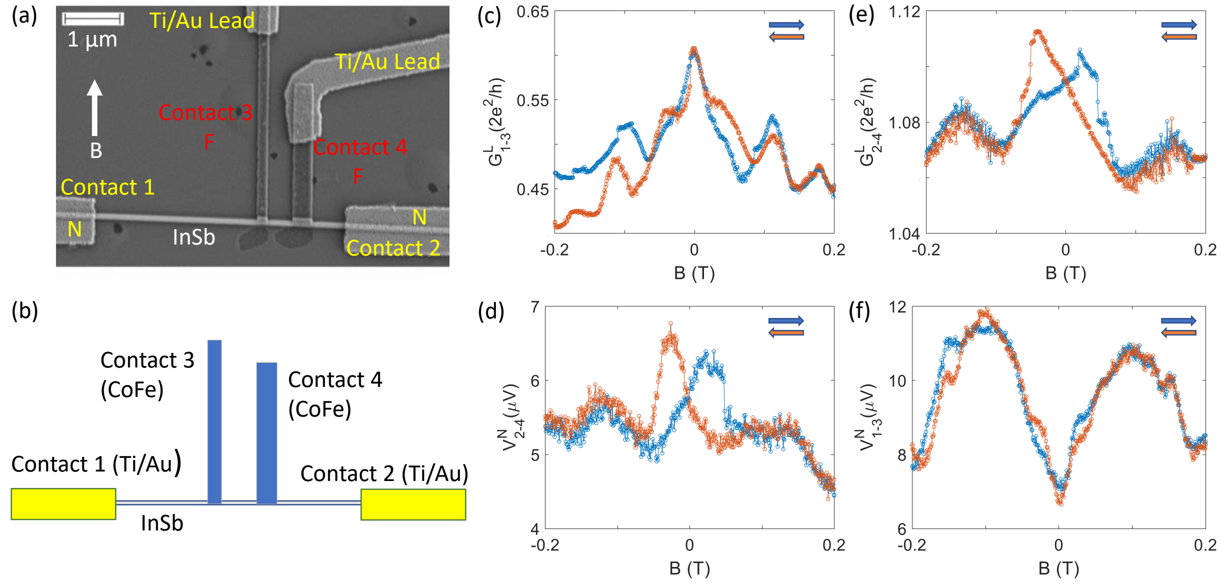

Figure 4.8. (a) Scanning electron microscope (SEM) image of a N-F-F-N device. The direction of the applied magnetic field *B* is indicated by arrow. (b) Schematic of the device. Data shown in this figure are acquired by a lock-in. (c, d) Local and non-local signals from magnetic field scan taken at 0.1 mV AC voltage bias, zero DC voltage bias and V_g = 1.2 V in configuration 1. (e, f) Local and non-local signals from magnetic field scan in configuration 2 taken at 0.1 mV AC voltage bias, 1 mV DC voltage bias and V_g = 1.35 V. For (c) and (e), the resistance of the measurement circuit is not subtracted (around 4.5 kΩ). For (d) and (f), the voltage is the AC voltage measured by lock-in. This figure is adapted from [104].

Similar to a F-F device, plots under magnetic field scans are generated for studying an N-F-F-N device. There are two configurations used for the measurement. For the first configuration, a voltage bias is applied across contact 1 and contact 3 with an ammeter connected in series. Non-local voltage is monitored simultaneously by a voltmeter connected across contact 2 and contact 4. The local conductance under magnetic field scan is shown in Figure 4.8 (c). It can be inferred that there is no clear hysteresis of the magnetoresistance and the local minimums of

magnetoresistance are located at zero magnetic field. On the other hand, the non-local voltage shown in Figure 4.8 (d) is hysteretic with local maximums located symmetrically around zero magnetic field. Data from Figure 4.8 (c) and (d) present the feature expected for the picture of non-local spin valve. However, for the second configuration where the voltage bias is connected across contact 2 and 4 with non-local signals monitored across contact 1 and 3, the local conductance is clearly hysteretic. For the non-local signal, the local minimums are centered at zero field. Small hysteretic loops around the zero field are observable. For hysteresis in non-local signals, the basic picture of non-local spin-valve can be applied. However, hysteresis in local signals cannot be explained by spin-injection.

For better understanding of the signals measured in this N-F-F-N device, more data from magnetic field scans at different back-gate voltages are shown in Figure 4.9 and Figure 4.10. We can observe that hysteresis can be observed locally or non-locally. In a N-F-F-N device, signals without clear hysteresis are also very common, which can be explained by charge jumps and less sharp magnetization switching of CoFe contacts. Moreover, the features of signals are highly adjustable by the back-gate. These observations do not always agree with the picture of spin-valve and the demonstration of spin injection into an InSb nanowire is questionable. In the next section, we will discuss another simple mechanism which may bring hysteresis to an InSb nanowire device.

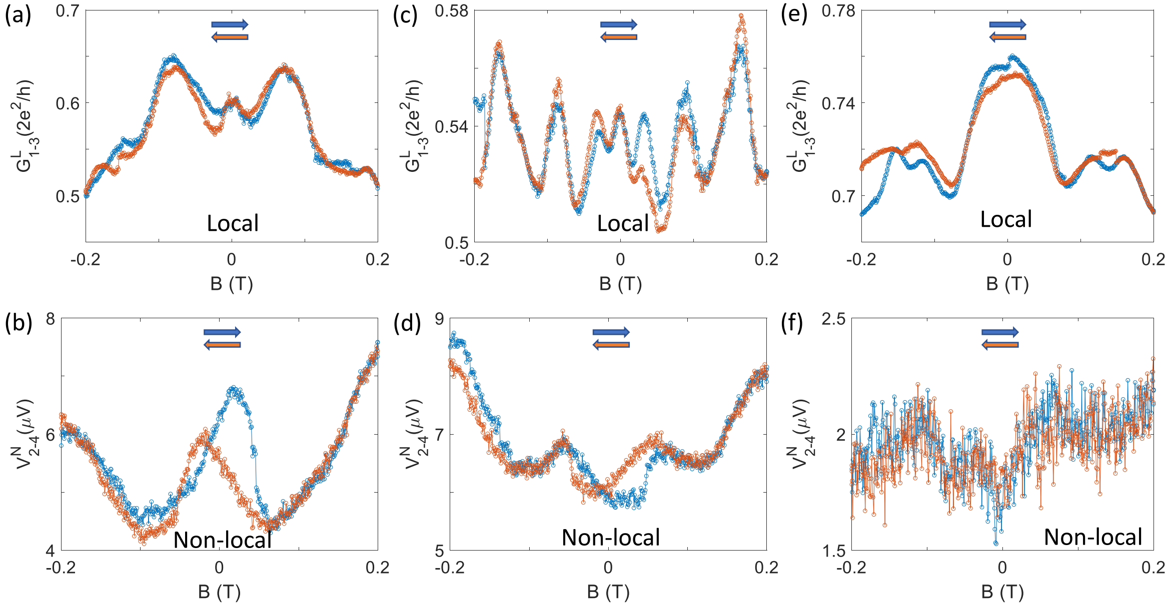

Figure 4.9. Additional data from N-F-F-N device. Magnetic field scan measured from the device shown in Figure 4.8 (a). Voltage is applied across contacts 1 and 3. Non-local signal is the voltage across contacts 2 and 4. (a,b) Local and non-local magneto-conductance measured at 0.1 mV AC bias and 1.2 V gate voltage. (c,d) Local and non-local magneto-conductance measured at the same bias and gate setting as in (a,b), but at a different time. (e,f) Local and non-local magneto-conductance measured at 0.1 mV AC bias and 2.85 V gate voltage. This figure is adapted from [104].

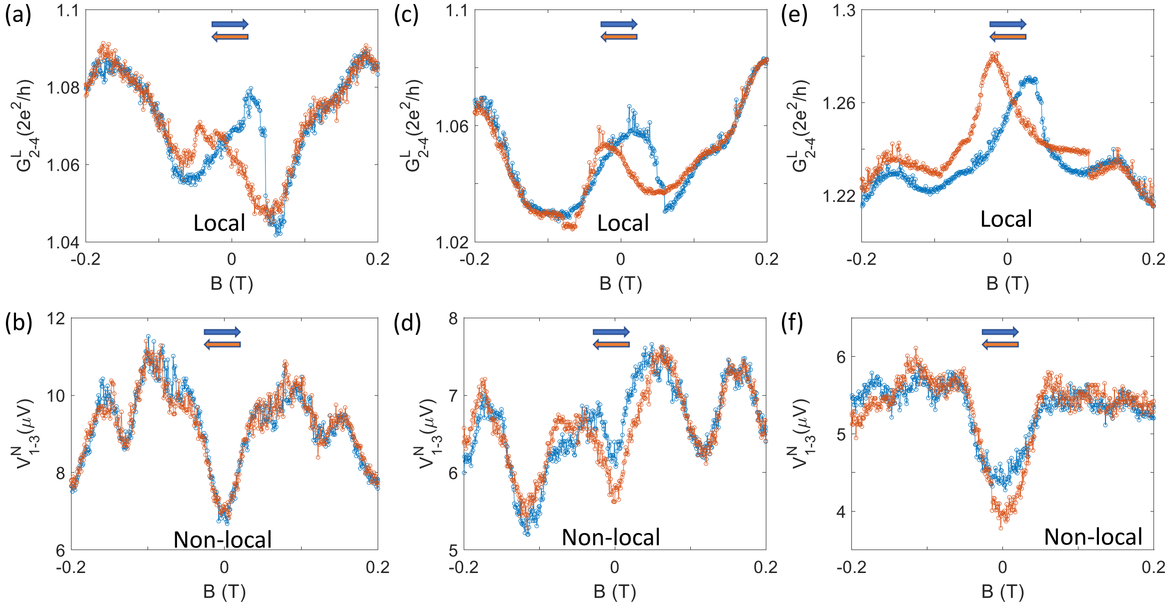

Figure 4.10. More data from N-F-F-N device shown in Figure 4.8 (a). Voltage is applied across contacts 2 and 4. Non-local signal is the voltage across contacts 1 and 3. (a,b) Local and non-local magneto-conductance measured at 1mV DC bias, 0.1 mV AC bias and 1.35 V gate voltage. (c,d) Local and non-local magneto-conductance measured at 1mV DC bias, 0.1 mV AC bias and 1.5 V gate voltage. (e,f) Local and non-local magneto-conductance measured at 1mV DC bias, 0.1 mV AV bias and 2.7 V gate voltage. This figure is adapted from [104].

4.4 Hysteretic Magnetoresistance in a Device without Ferromagnetic Contacts

The discussion in section 4.3 tells us that ferromagnetic contacts may result in hysteretic signals in an InSb nanowire device under magnetic field scans. The origin of the hysteresis is not confirmed. In this section, we discuss InSb nanowire devices without ferromagnetic contacts. In this case, mechanisms involving electrons transport from a ferromagnet like spin-injection are forbidden. The origin of hysteresis is confirmed and we call it the local magnetic field effect.

4.4.1 Local Magnetic Field Effect in InSb Nanowire Devices

A device used to bring hysteresis to an InSb nanowire device without ferromagnetic contacts is shown in Figure 4.11 (a). An InSb nanowire is placed on a back-gate chip and two Ti/Au contacts are deposited to the nanowire, just as the device shown in Figure 4.5 (a). Additionally, two CoFe strips with different dimensions are deposited intentionally beside the nanowire without forming any contacts. In case CoFe is on top of the nanowire, the naturally formed oxide layer of InSb will protect any formation of contacts. We emphasize that only Ti/Au ohmic contacts are formed in this device. We call this type of device N-(F,F)-N device.

The measurement setup for an N-(F,F)-N device is shown in Figure 4.11 (b). A voltage source is connected across the two Ti/Au contacts and current through the nanowire is measured. It is clear that for an N-(F,F)-N device, no electrons coming from ferromagnets can transport into the nanowire and there is no possibility of common electrical injection of spin-polarized current. Nevertheless, under magnetic field scans, the magnetoresistance of the device can still be hysteretic, as shown in Figure 4.11 (c) and (d). In Figure 4.11 (c), when the magnetic field is swept from -0.2 T to 0.2 T, there are two clear sharp switches of the measured current located at about 43 mT, and 53 mT. These switches correspond to the different coercive fields of the two CoFe strips. A local maximum of current (minimum of magnetoresistance) is located at about 35 mT. When the applied magnetic field is swept from 0.2 T to -0.2 T, the switches are at about -42 mT and -63 mT. A maximum of current is at about -25 mT. The hysteresis of this device comes from the local magnetic fields generated from magnetized CoFe strips. The local maximum or local minimum of magnetoresistance around zero field from the background shown in Figure 4.5 (b) is shifted away from zero field by the local magnetic fields. The magnitude of the local magnetic

fields is on the order of 30 mT based on the local maximums read from Figure 4.11 (c). The error of reading the fields is ± 1 mT from scan resolution.

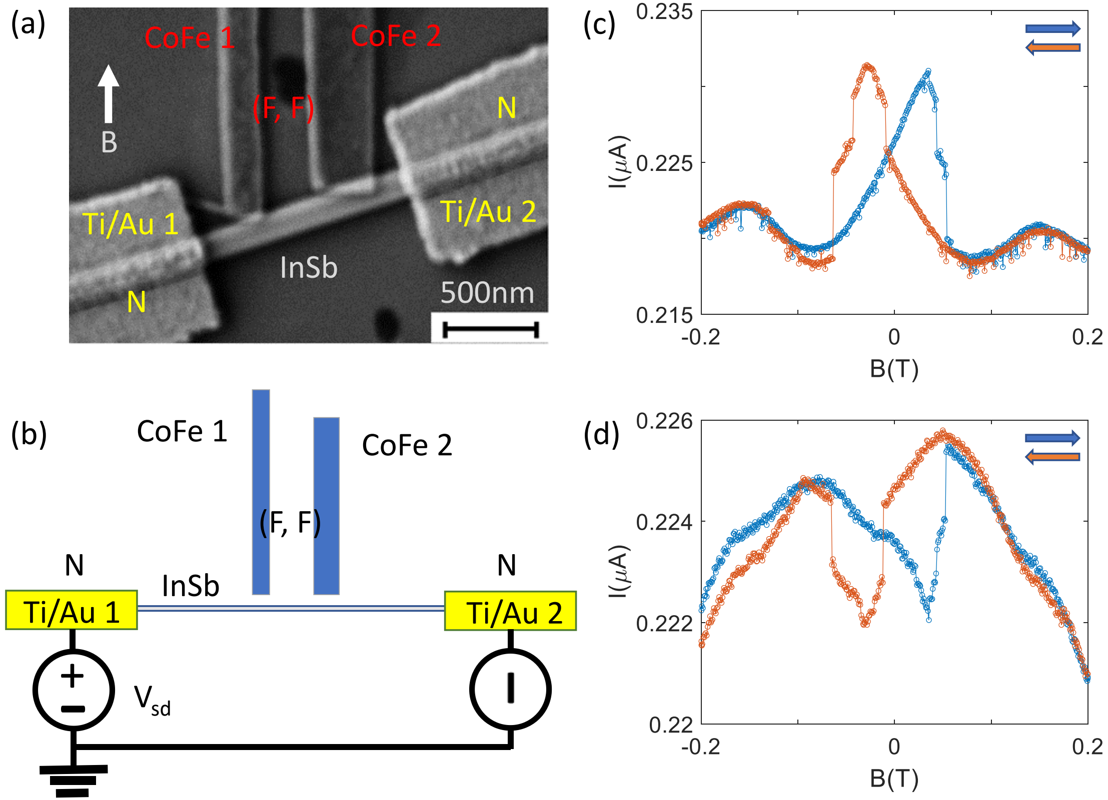

Figure 4.11. (a) Scanning electron microscope image of a N-(F,F)-N device. The two CoFe strips are insulated from the nanowire by native oxide. The direction of the external magnetic field *B* is indicated by arrow. (b) Schematic of measurement setup. (c) Current as function of external magnetic field using the source-drain bias voltage V_{sd} = 2 mV and gate voltage V_g = 1.05 V. Directions of magnetic field sweeps are indicated by arrows. (d) Magnetic field scan taken at V_{sd} = 2 mV and V_g = 1.1 V. This figure is adapted from [104].

Same as the devices with ferromagnetic contacts, the features of measured magnetoresistance in an N-(F,F)-N device can be adjusted by back-gate voltage. In Figure 4.11

(d), by adjusting the back-gate voltage, instead of local maximums, local minimums of measured current are observed. This shares very similar features with the simple picture of a spin-valve. We may notice that the curves at negative field do not overlap in the range from -0.2 T to -0.1 T, while at positive field, they do basically overlap. This may come from irreproducible charge jumps due to local charge rearrangement. In fact, charge jump is a common phenomenon in our devices discussed in this thesis. The data shown in the above section may also experience charge jumps. To distinguish magnetization switching from charge jumps, we perform more magnetic scans to check the reproductivity of the switching positions. Here, we provide more scans shown in Figure 4.12. It can be justified that switching positions are consistent. Sometimes the switching is less prominent as shown in Figure 4.12 (c) and (e). This may come from the nature of the magnetoresistance background. If the background magnetoresistance is flat all over the applied magnetic field range, there is no clear hysteresis expected to be observed.

With the data shown in Figure 4.11 and 4.12, we know why demonstration of spin injection in the devices shown in section 4.3 is questionable. In an InSb nanowire device with ferromagnetic contacts, local magnetic fields are generated from magnetized CoFe contacts. It is difficult to rule out the local magnetic field effect for observed hysteresis. The observed hysteretic signals from section 4.3 and section 4.4 are visually the same in terms of their extent in magnetic fields. Since there are also features not explained by the simple picture of spin injection, for example, smaller magnetoresistance at anti-parallel CoFe magnetization, we may conclude that hysteresis in devices with ferromagnetic contacts are also likely from the local magnetic field effect.

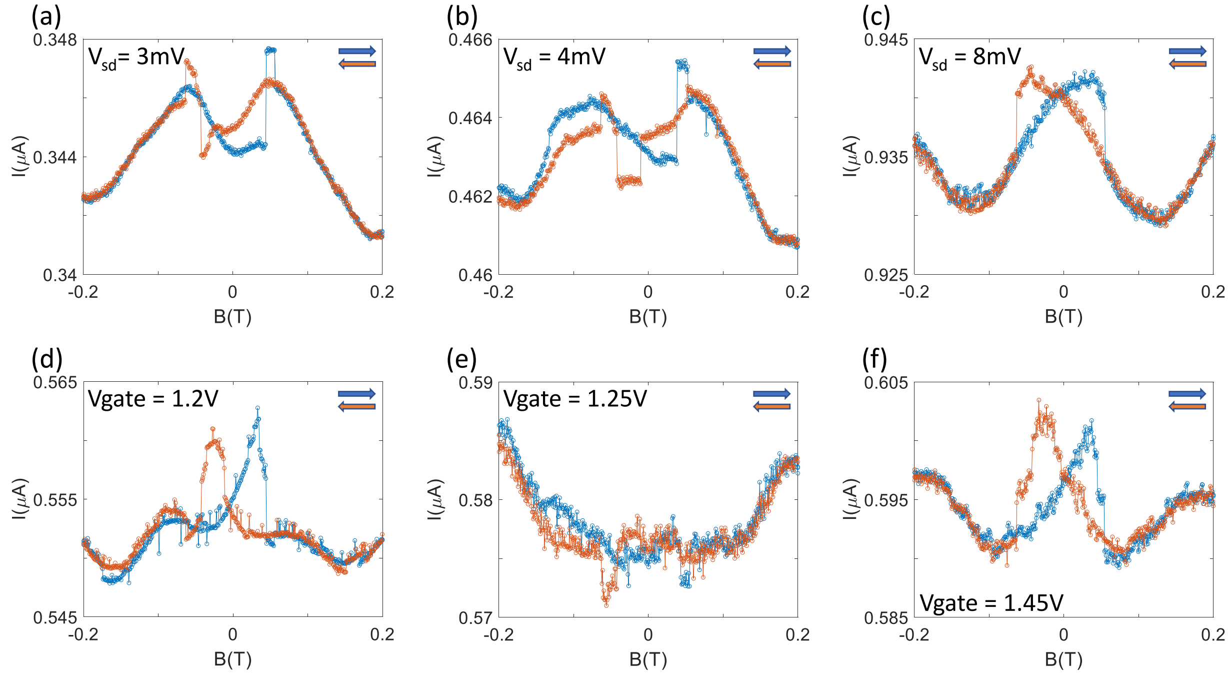

Figure 4.12. Additional magnetic field scans measured in the N-(F,F)-N device shown in Figure 4.11. We observe that the response can be modulated by gate voltage and bias voltage. Current vs. magnetic field measured at different gate and bias settings. Data are acquired by DC measurement. (a-c) at V_g = 1.1 V. (d-e) at V_{sd} = 5 mV. This figure is adapted from [104].

The magnetization of CoFe strips is resistant to external fields applied in different directions. In Figure 4.13, magnetic field scans are performed under an additional finite magnetic field perpendicular to the long axis of CoFe strips. When the additional field is not too large, the measured current can still be hysteretic. It is interesting that the visual features of Figure 4.13 (a) and (b) are similar to a claimed spin-filtering feature demonstrated in a device with ferromagnetic contacts [111]. Again, we emphasize that in our devices without ferromagnetic contacts, there should not be any features explained by electron transport from ferromagnets.

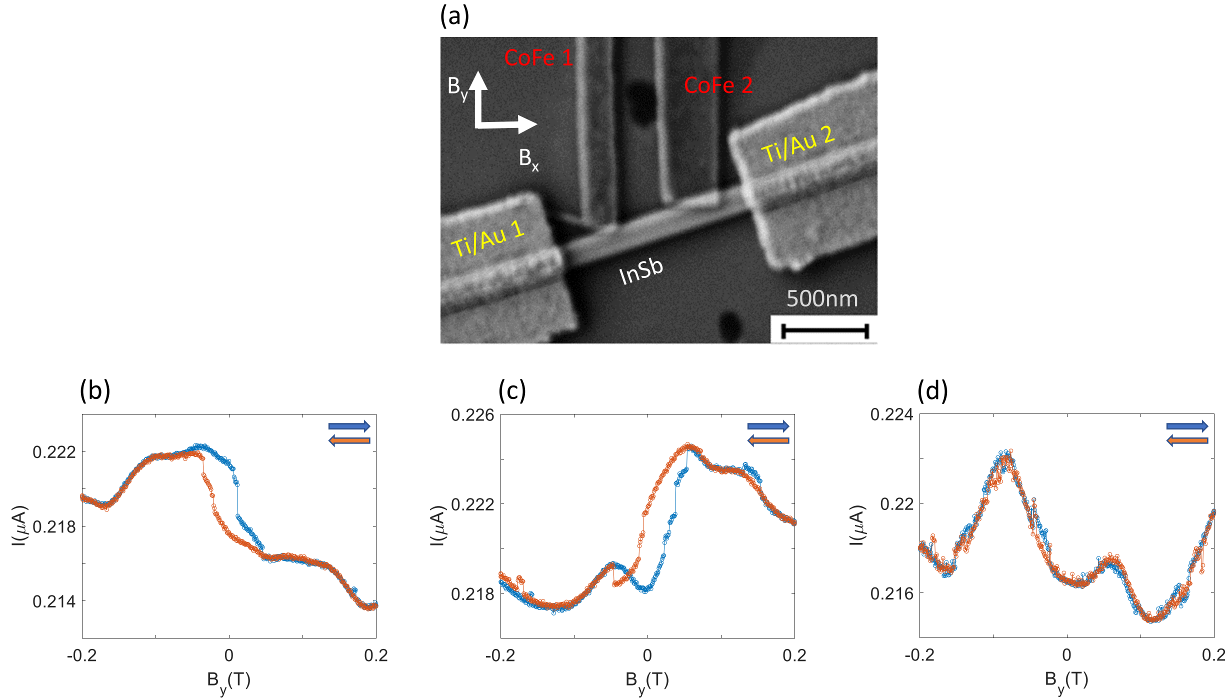

Figure 4.13. Measurements in a finite B_x. (a) SEM image of the device also shown in Figure 4.11 with field directions indicated. (b-c) B_y magnetic field scan with B_x = -0.2 T and B_x = 0.2 T respectively. Data are acquired by DC measurement. Both plots are measured at V_{sd} = 2 mV and V_g = 1.05 V. Magnetoresistance is not symmetric, but hysteresis is observable. (d) B_y magnetic field scan with B_x = -1 T. The measurement is performed at V_{sd} = 2 mV and V_g = 1 V. At this large B_x field, there is no observable hysteresis as the magnetization of CoFe strips is pinned by B_x. Measurements are performed using a 2D vector magnet with sample plane aligned with magnetic field plane. This figure is adapted from [104].

4.4.2 Numerical Simulations of Ferromagnets

We perform numerical simulations of stray fields from ferromagnets to compare with the data from experiments. Simulations are based on the geometry of the device shown in Figure 4.11. The orientation of the InSb nanowire is included. The two CoFe trips have the dimensions of 150

nm × 4500 nm × 40 nm and 300 nm × 3000 nm × 40 nm respectively. By taking the intersection of two strips and the nanowire and lifting this intersection, the small CoFe overlap on top of the nanowire is also included. The magnetic parameters of the CoFe strips are not known since these parameters vary in a broad range [116-119]. Instead, we use parameters of Co since we expect Co can give close results to CoFe. The simulations are performed using a GPU-accelerated program, MuMax3 [120, 121] and setting the magnetic saturation to be 1.44×10^6 A/m, the first order uniaxial anisotropy constant to be 4.1×10^{-1} J/m^3, the second order uniaxial anisotropy constant to be 1.4×10^{-1} J/m^3, the exchange constant to be 3×10^{-11} J/m, and the phenomenological damping constant to be 0.01. 10 nm cubic cell is used to reduce computation time but the exchange length of CoFe is likely smaller than 10 nm.

Simulation results are presented in Figure 4.14. The coordinates are defined in Figure 4.14 (a) where the *u* axis is along the nanowire and *v* axis is perpendicular to the nanowire. The hysteretic loop under magnetic field scan in the *y* direction is shown in Figure 4.14 (b), which simulates the experiments shown in section 4.4.1. We observe platforms like features around ±50 mT, which is consistent with the experimentally observed anti-parallel magnetization configuration. The asymmetry of the loop indicates possible influence on magnetization from local magnetic fields. Small switching exists close to zero field which is likely from the small CoFe overlap. For quantitative characterization of local magnetic fields, stray fields are acquired and averaged inside the hexagonal nanowire cross section with the size of 100 nm (the thickness of the nanowire). The stray fields profile along the nanowire when the strips are magnetized in parallel (+*y* direction) is plotted and shown in Figure 4.14 (c). The main component of the stray field, B_v, is perpendicular to the nanowire as expected. Though, other components are not small. The local field profile is not symmetric since the two strips lack symmetry. From the simulation, the largest

local field is larger than 100 mT. It is likely that the set saturation magnetization is too large compared to the real CoFo strips used in experiments.

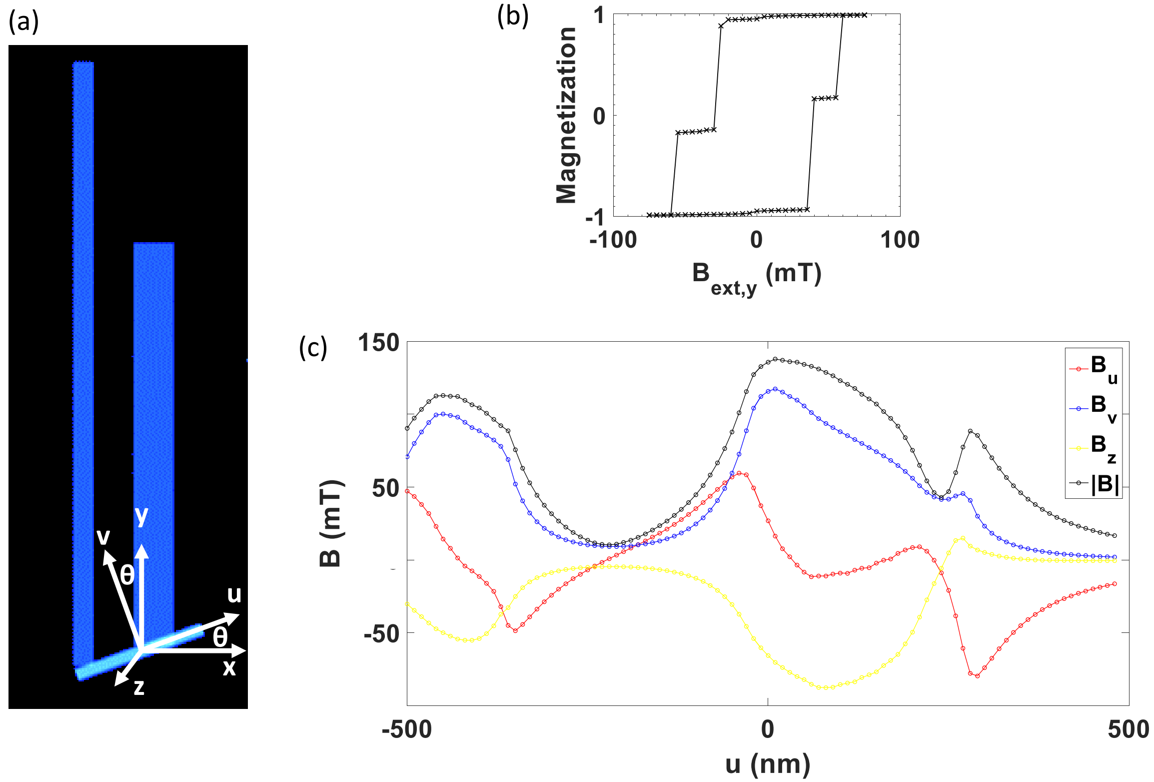

Figure 4.14. (a) The numerical simulation geometry and the coordinate system. The origin of the coordinates is located at the center of the nanowire segment. *u* axis is along the nanowire. The angle *θ* between *x* and *u* is 20º. (b) Average normalized magnetization in *y* direction of the two strips. (c) The stray field in the nanowire for parallel up magnetization (achieved when $B_{ext,y}$ = 75 mT) as function of *u*. This figure is adapted from [104].

The averaged local magnetic fields for other configurations of magnetization are given in Figure 4.15, Figure 4.16 and Figure 4.17. Overall, numerical simulations of the local magnetic fields generated from the ferromagnetic strips are consistent with experimental data acquired in

section 4.4.1. We further confirm the local magnetic field effect in InSb nanowire devices with ferromagnetic components.

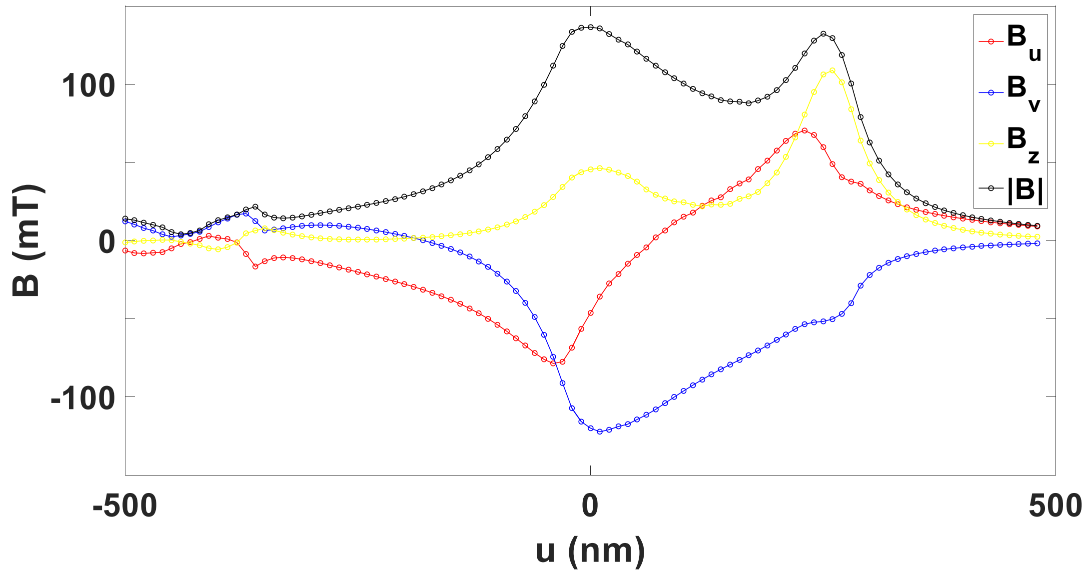

Figure 4.15. The averaged stray field in the nanowire for anti-parallel up-down magnetization ($B_{ext,y}$ = -50 mT) as function of the nanowire coordinate u. This figure is adapted from [104].

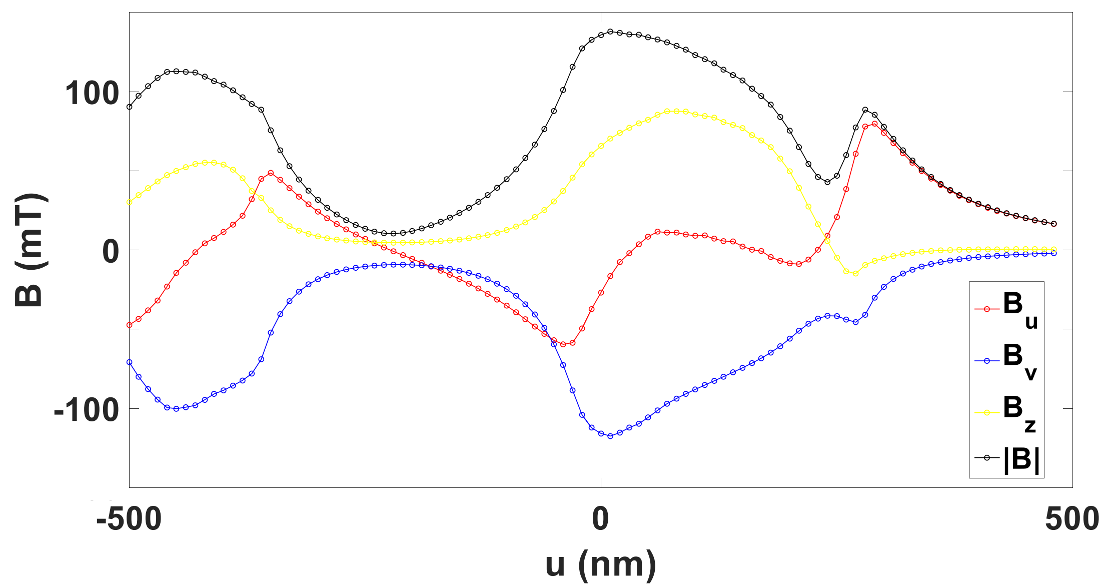

Figure 4.16. The averaged stray field calculated in the nanowire for parallel down magnetization ($B_{ext,y}$ = -75 mT) as function of the nanowire coordinate *u*. This figure is adapted from [104].

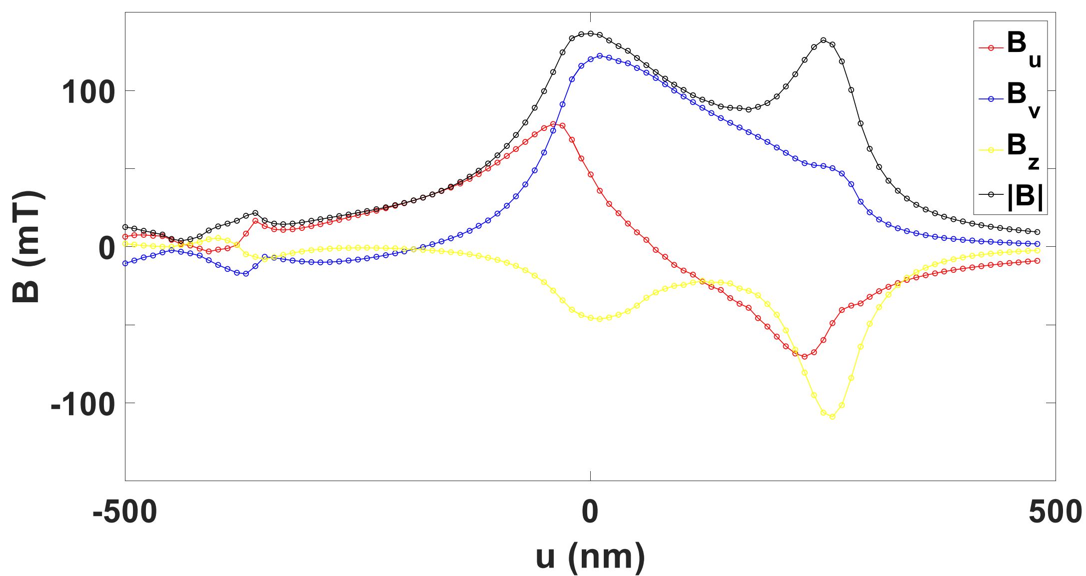

Figure 4.17. The averaged stray field in the nanowire for anti-parallel down-up magnetization ($B_{ext,y}$ = 50 mT) as function of the nanowire coordinate *u*. This figure is adapted from [104].

5.0 Local Magnetic Field Effect for Majorana Bound States

As discussed in Chapter 2, MBSs can be found in a hybrid nanowire device with Zeeman field. Besides applying magnetic fields externally from an electromagnet, alternative methods for providing the Zeeman field have been proposed. A magnetic insulator covered on a semiconductor nanowire is an option by providing an effective Zeeman field from exchange coupling [20, 21]. Another option is arrangement of micromagnets and by this option, even martials without strong spin-orbit coupling may become candidates for searching MBSs [24, 25, 122-125].

From Chapter 4, we confirm that local magnetic fields can be generated from ferromagnetic micro-strips and an InSb nanowire responds to these fields, resulting in observable hysteresis under magnetic field scans. Since an InSb nanowire is a promising platform for MBSs, we raise the idea of using local magnetic fields from micromagnets to realize MBSs at zero applied external magnetic field. To study the feasibility of this idea, we perform numerical simulations of micromagnets to understand the generated local magnetic field profiles. A theoretical model of MBSs with the local magnetic field profiles simulates possible topological states appearing in a nanowire. As preliminary experimental studies, we also image the local magnetic fields of fabricated micromagnet patterns through magnetic force microscopy (MFM). The experimental results demonstrate difficulties for arranging proper magnetizations of micromagnets, especially when a micromagnet pattern is complicated. This chapter is adapted from [126] and authors are M. Jardine, J. Stenger, Y. Jiang, E.J. de Jong, W. Wang, A.C. Bleszynski Jayich, S. Frolov.

5.1 Method of Simulation

The simulation of MBSs with local magnetic profiles consists of two parts. The first part is to simulate local magnetic field profiles from different arrangements of micromagnets. The second part is to utilize the simulated local magnetic fields to simulate MBSs in a nanowire.

Simulations of stray fields are discussed in section 4.4.2. In this chapter, we still use MuMax3 as the simulation program and magnetic parameters for Co. The saturation magnetization and exchange constant are the same as section 4.4.2. Anisotropy constant K_1 is set to 4.5×10^5 and anisotropy constant K_2 is set to 1.5×10^5. There are mainly two types of micromagnet geometries used in the simulation. They are cuboids with dimensions of 130 × 1000 × 100 nm (thin magnet) and 250 × 1000 × 100 nm (thick magnet). Complicated magnetic patterns are designed by arrangement of the two types of magnets. The local magnetic fields can theoretically extend to infinity. For simulations, we use a nanowire with finite length and monitor the local magnetic field profiles around the nanowire.

To calculate energy spectrums and wave functions of MBSs, a one-dimensional Majorana nanowire model [127] is utilized. The parameters are set as following: induced gap, $\Delta = 0.08$ meV; spin-orbit coupling, $\alpha_R = 20$ meV·nm; effective electron mass is 0.04 m_e; g factor of InSb, $g_{eff} = 50$. Simulated local magnetic field profiles are input into the model as the Hamiltonian for Zeeman energy. Energy spectrums and wave functions are calculated by exact diagonalization of the Hamiltonian of the Majorana nanowire model. The lowest energy states correspond to the pair of Majorana zero modes (MZMs).

5.2 Numerical Results

To obtain a desired local magnet field profile for MBSs, careful design of micromagnets can be helpful to approach our goals. Recall from chapter 2, for the purpose of supporting MBSs, the magnetic field profile in a nanowire is preferred to be along the nanowire, since this magnetic field direction is mostly perpendicular to the effective spin-orbit field. We found that designs based on a “Dragonfly setup” can support MBSs appearing in a Majorana nanowire. With sophisticated arrangement of dragonfly setups, we propose a possible geometry for braiding MBSs in a T-junction.

5.2.1 Stray Fields of a Bar Magnet

Before going to more complicated designs of micromagnets, it is useful to have the knowledge of stray fields from a simple bar magnet. The stray field of a micromagnet with the dimension of $230 \times 1000 \times 100$ nm is shown in Figure 5.1.

The stray field from a bar magnet is large close to the magnet. However, this stray field attenuates quickly and the field far away from the magnet is quite weak. To have enough large effective magnetic field inside a nanowire, a bar magnet needs to be placed close to the nanowire. Additionally, proper arrangement of multiple magnets may enhance the magnetic field inside a nanowire. In Figure 5.2, we show a field profile between two magnets. A nanowire placed in the middle of the two magnets can feel an enhanced field.

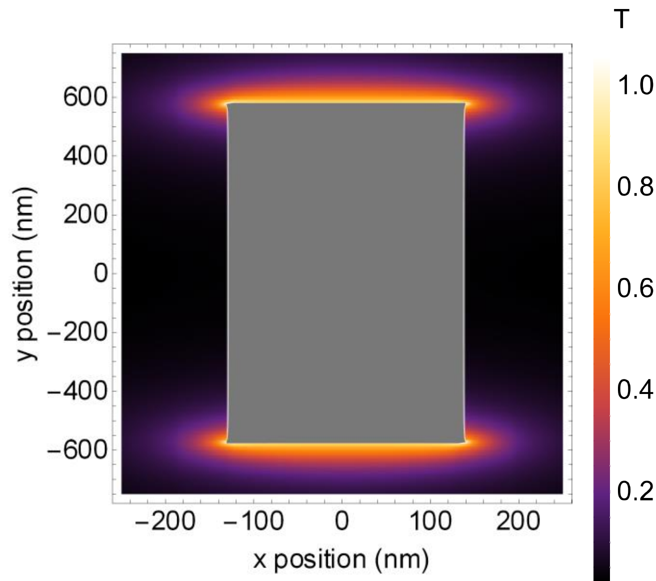

Figure 5.1. A heat map for magnetic field magnitude for a micromagnet of dimensions 230 × 1000 × 100 nm. This is shown for a 2D X-Y plane slice through the middle of the micromagnet (50 nm), the magnet is shown as grey. Note the field is very weak away from the micromagnet ends.

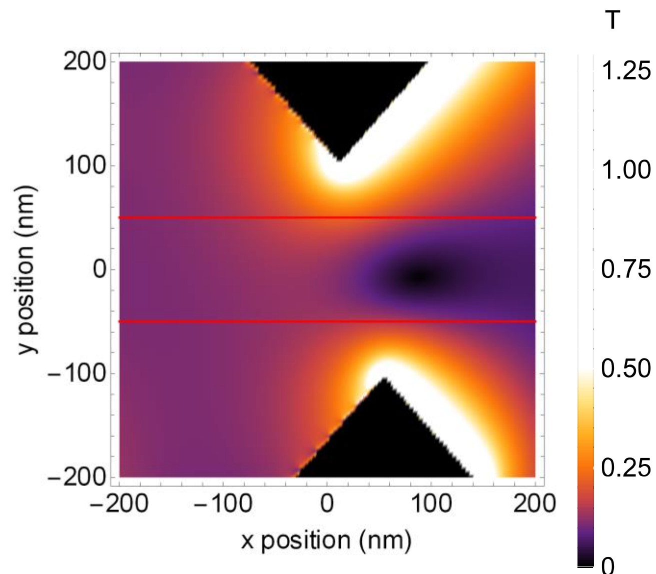

Figure 5.2. A X-Y plane heat map for magnetic field magnitude in a small region near the nanowire, the magnet areas have been set to 0 field (black triangular regions). This is for a 5 nm thick slice in the middle where the nanowire is (marked by red lines).

5.2.2 Dragonfly Setup

It is not so hard to come up with an arrangement of micromagnets which provides a local magnetic field profile basically along a nanowire. A straightforward method is to arrange four bar magnets with the locations and magnetizations shown in Figure 5.3. Bar magnets with different dimensions can have different magnetizations due to their different coercivities, as discussed in chapter 4. It is found that for further complicated designs, the bar magnets can be rotated by 45 degrees and it is the easier arrangement to realize desired magnetization directions. When the magnetization direction is perpendicular to the applied magnetic field, the magnetization is more resistant compared to the case of applied field along the magnetization direction. This can be inferred from Figure 4.13.

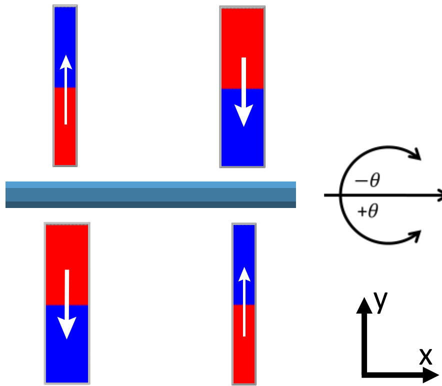

Figure 5.3. A simple configuration that generates magnetic field along a nanowire. Magnetization directions are represented by arrows.

The configuration with 45-degree angling of bar magnets is shown in Figure 5.4. This is the basic component of our designs and we call this configuration “Dragonfly setup”. In Figure 5.5, the magnetic field profile of the dragonfly setup is presented. Along the *x* axis, there is a

segment of the field basically along the x direction. The magnitude is on the order of 100 mT. For the MBSs simulation, we set a relatively small critical field for topological phase transition indicated by the horizontal dashed line. In this case, the field segment along the x direction is larger than the critical field. A Majorana nanowire located at a proper location under this local magnetic field profile can reach the topological regime. The magnetic field in the z direction is not presented since this field component is not relevant.

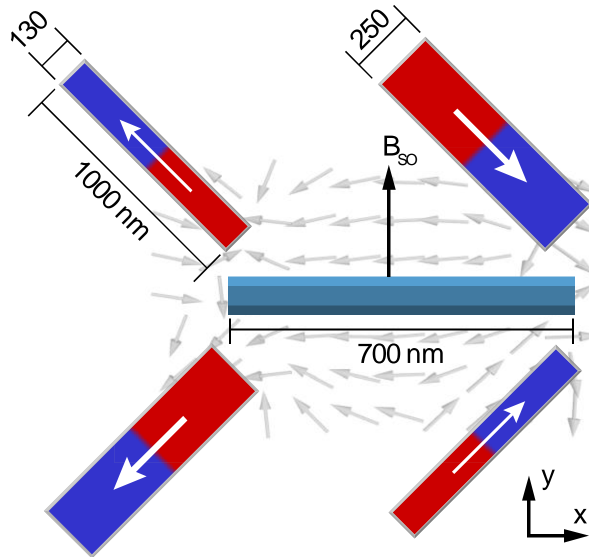

Figure 5.4. The Dragonfly setup with four micromagnets (blue/red) and an overlay of the magnetic field calculated with MuMax3 (gray arrows). The nanowire runs horizontally with the spin-orbit axis vertical, indicated by B_{so}.

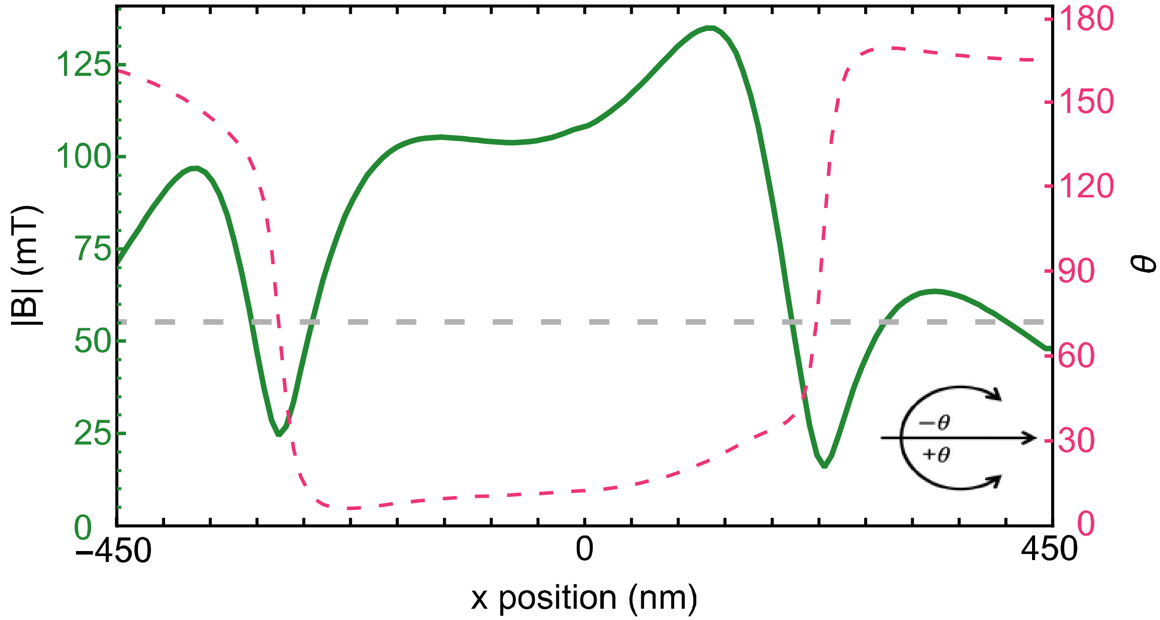

Figure 5.5. Magnetic field profile, as a function of position, of the four magnet Dragonfly setup. Solid line is field amplitude and dashed line is field angle *θ* relative to negative x-axis (inset). The field is averaged over a hexagonal cross-section of the nanowire with a characteristic dimension of 100 nm. In this figure only, the reader is invited to imagine an infinitely long nanowire without ends and consider what field profile would be created along such a nanowire. The horizontal dashed gray line indicates a uniform field for entering the topological regime in an infinite nanowire.

The configuration shown in Figure 5.3 can produce a similar field profile as the Dragonfly configuration with 45-degree rotation. The magnitude of the field is even larger, as shown in Figure 5.6. Larger field magnitude is preferred based on the criteria in equation (2.24). A large induced superconducting gap may result in a more robust topological state. However, that requires a larger Zeeman field. The dragonfly setup with 45-degree rotation gives a tradeoff between field magnitude and stability of magnetization.

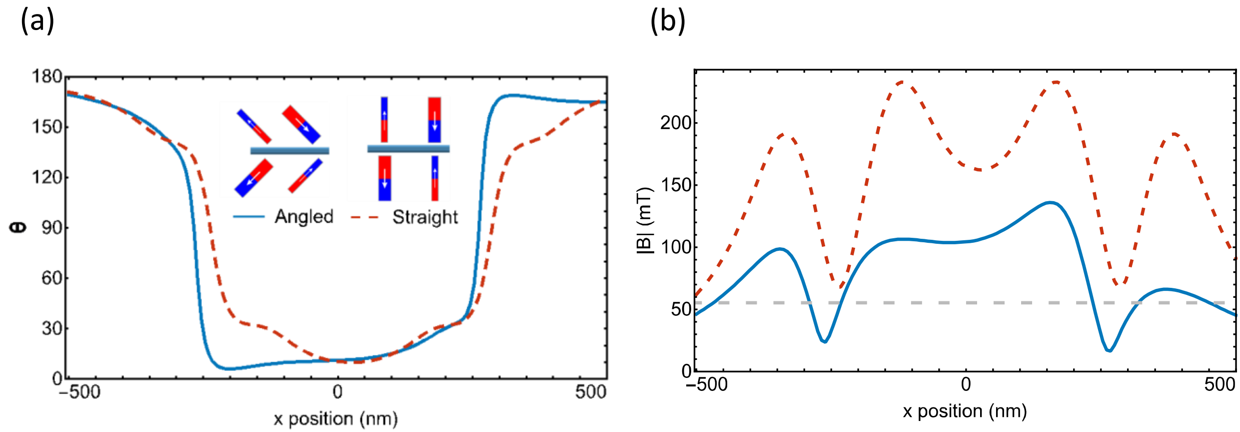

Figure 5.6. This compares the rotated and un-rotated Dragonfly configuration. The solid line is the rotated set-up and the dashed line is the straight set-up. Rotating the magnets makes them easier to magnetize through hysteresis. This figure is for a 1000 nm nanowire segment.

To learn about the uniformity of the local magnetic field inside the nanowire, we plot the standard deviation of the field magnitude over the cross section of the nanowire in Figure 5.7. In the middle section, the deviation of the field is low. More prominent deviation appears at the two ends of the regions. This larger deviation comes from the non-uniform field close to the tips of magnets.

With the magnetic field profile, the probability distribution of two MBSs along a 700 nm nanowire under the Dragonfly setup is plotted in Figure 5.8. The MBSs are not well separated since the two wave functions highly overlap. For more robust realization of MBSs, we need less overlapping of wavefunctions, requiring better design of magnetic patterns.

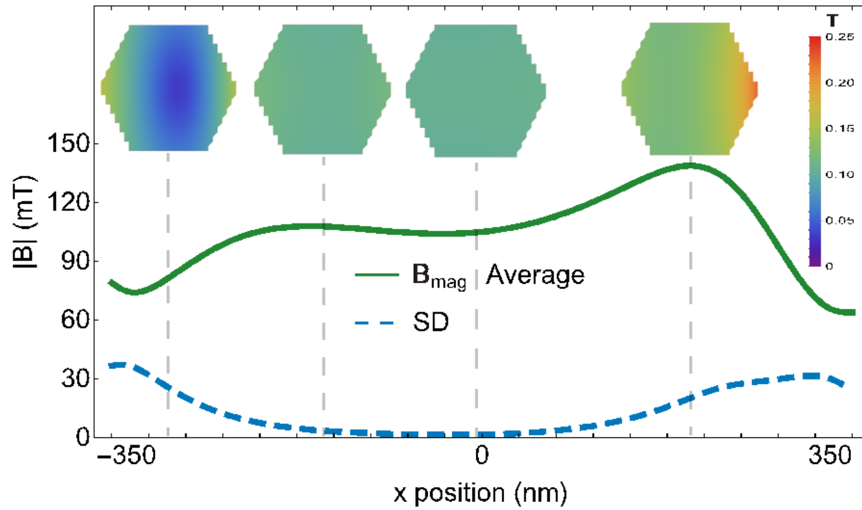

Figure 5.7. Shows the magnetic field magnitude's standard deviation (dashed) across the hexagonal cross-section and mean value over the nanowire region for the single Dragonfly set-up. The insets are field magnitude cross sections of the nanowire at different positions.

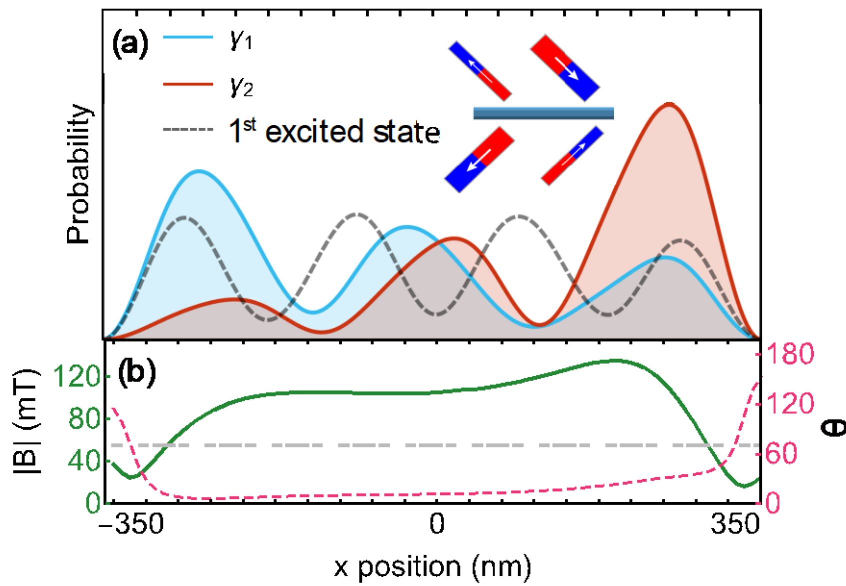

Figure 5.8. (a) Probability distributions for two Majorana wavefunctions γ_1 and γ_2. The first excited state (dashed line) is a bulk nanowire state. (b) Magnetic field profile reproduced from Figure 5.5 over a smaller range. Hard boundaries are introduced at ±350 nm to calculate the wavefunctions. There is no applied external field.

5.2.3 Double Dragonfly Setup

To separate MBSs, a more advanced local magnetic field profile can be achieved by a combination of two Dragonfly setups. A preliminary double Dragonfly setup is given in Figure 5.9. With an additional applied external magnetic field of 40 mT in the positive *y*-direction, the generated magnetic field profile is weak at the middle section but has two plateaus with the order of 100 mT at the two ends of the section. By this profile, we expect that for each plateau, the critical field requirement is satisfied and a pair of MBSs appear. This results in two pairs of the MBSs along the nanowire section. From the probability distribution, the two pairs MBSs are located on each side of the nanowire and are not coupled. The magnetic field profile at the right and left side have reverse signs, indicating MBSs with different spins. Superficially MBSs with opposite spins cannot couple [128].

By adding a vertical bar magnet shown in Figure 5.10 and Figure 5.11, we can couple the left and right MBSs in a simple double Dragonfly setup. The central vertical magnet provides a field rotation to MBSs close to it. From the probability distribution, wavefunctions are separated and there is more robust MBS polarization of the ground state, E_0. A longer nanowire helps the reduction of overlapping. The probability distribution can be tuned by external magnetic fields, which is shown in Figure 5.12.

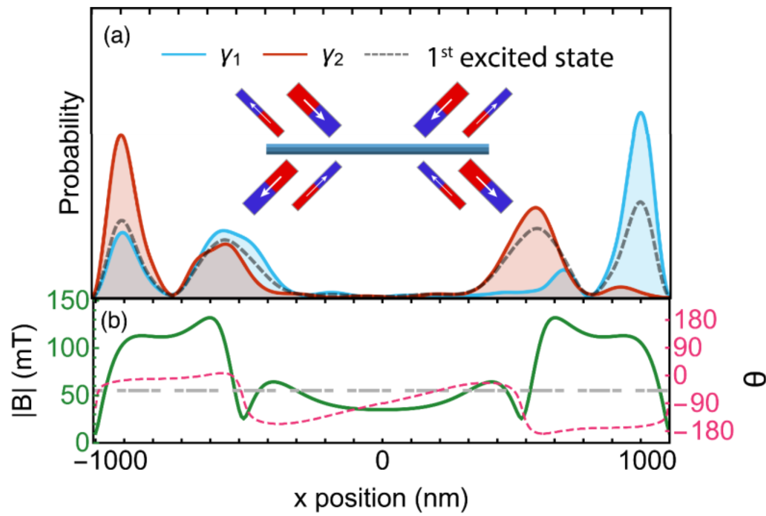

Figure 5.9. (a) Probability distributions for two lowest energy states, this system shows two overlapping and degenerate states with no clear Majorana polarization and no higher energy state being gapped out. The energies of both states $E_1/\Delta = 3.9 \times 10^{-2}$ and $E_2/\Delta = 4.6 \times 10^{-2}$. (b) Field profile along wire. External field is 40 mT in positive y-direction.

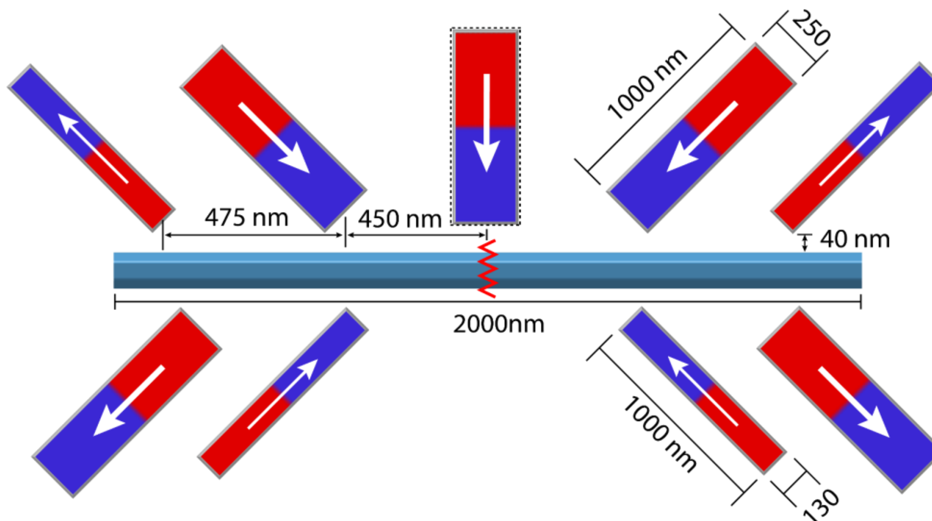

Figure 5.10. The double Dragonfly setup with the magnet in the middle and a potential gate, dimensions given. Toggling this gate allows the left and right side of the wire to be coupled or uncoupled.

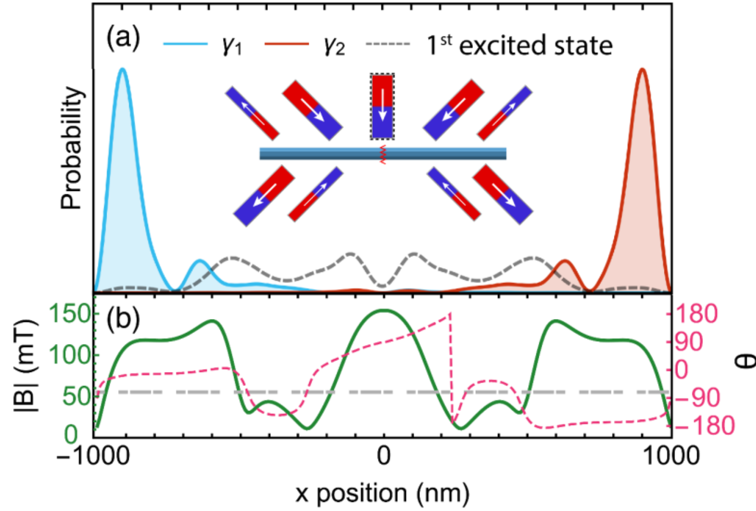

Figure 5.11. (a) Probability distributions of two lowest energy states for double Dragonfly setup with gate open (shown in inset). MZM (red/blue) with $E_0/\Delta = 5.1 \times 10^{-4}$. The first excited state (grey dashed) with $E_1/\Delta = 1.6 \times 10^{-1}$. External field of 40 mT is applied in positive y-direction. Inset: two dragonfly configurations, with zigzag indicating an electrostatic gate capable of dividing the nanowire in two parts. (b) Magnetic field profile along the wire, showing amplitude (solid) and angle (dashed).

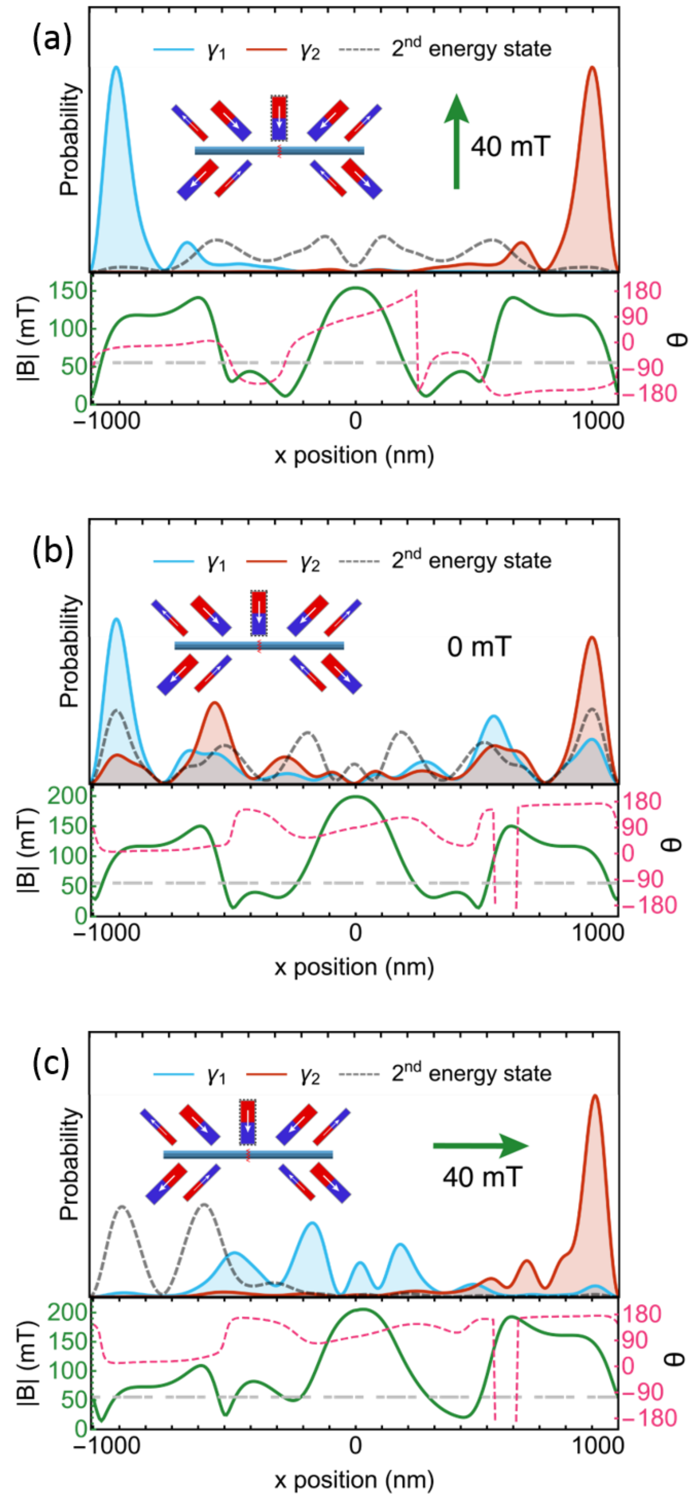

Figure 5.12. Comparing the double Dragonfly with different external fields. (a) 40 mT in the positive y direction (b) no field and (c) 40 mT in the positive x direction.

Micromagnets are metals. Besides proving stray fields, a bar magnet can also be used as a side gate. A double Dragonfly setup with a central vertical magnet indicated in Figure 5.10 provides a method to divide the nanowire section into two shorter Majorana nanowire sections. The central magnet can be used as a side gate to tune the chemical potential at the middle of the nanowire section. A side-gate voltage can pinch-off the nanowire portion to decouple the right side and left side of the nanowire. In this case, there is one pair of MBSs on each side. This is demonstrated in Figure 5.13.

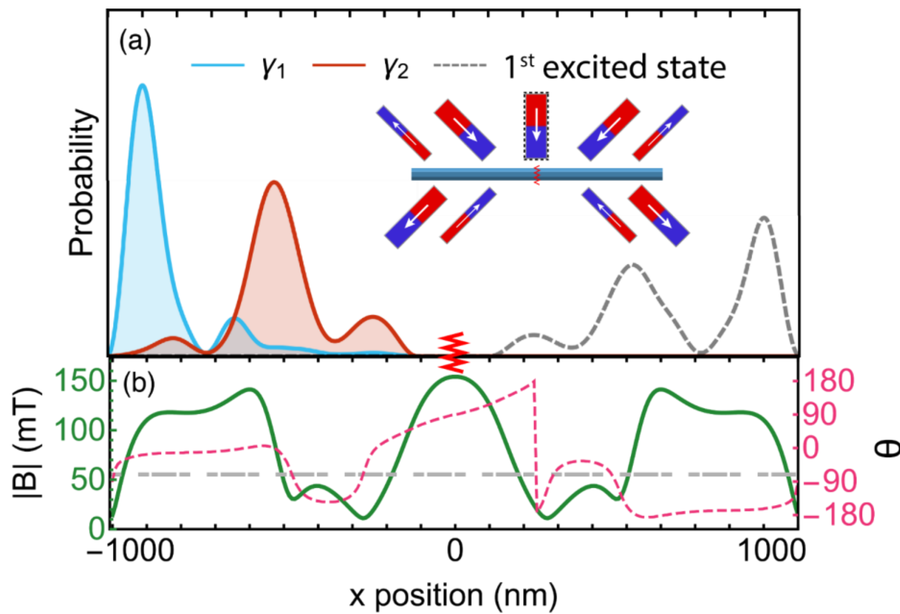

Figure 5.13. (a) Probability distributions for two lowest energy states for double Dragonfly setup with the central vertical magnet and the gate closed (inset). The probability distributions shows two separate pairs of MZMs in each section of the wire, the left is shown in the Majorana basis with energy $E_1/\Delta = 3.1 \times 10^{-2}$ (red and cyan), the other pair in the right section is in the electronic state basis with energy $E_2/\Delta = 3.1 \times 10^{-2}$ (black- dashed line). The third state is well separated at $E_3/\Delta = 8.9 \times 10^{-1}$. (b) Field profile along wire. External field is 40 mT in positive y-direction.

The local magnetic field in the z direction from micromagnets for the double Dragonfly setup is small and not relevant for discussions. This is shown in Figure 5.14.

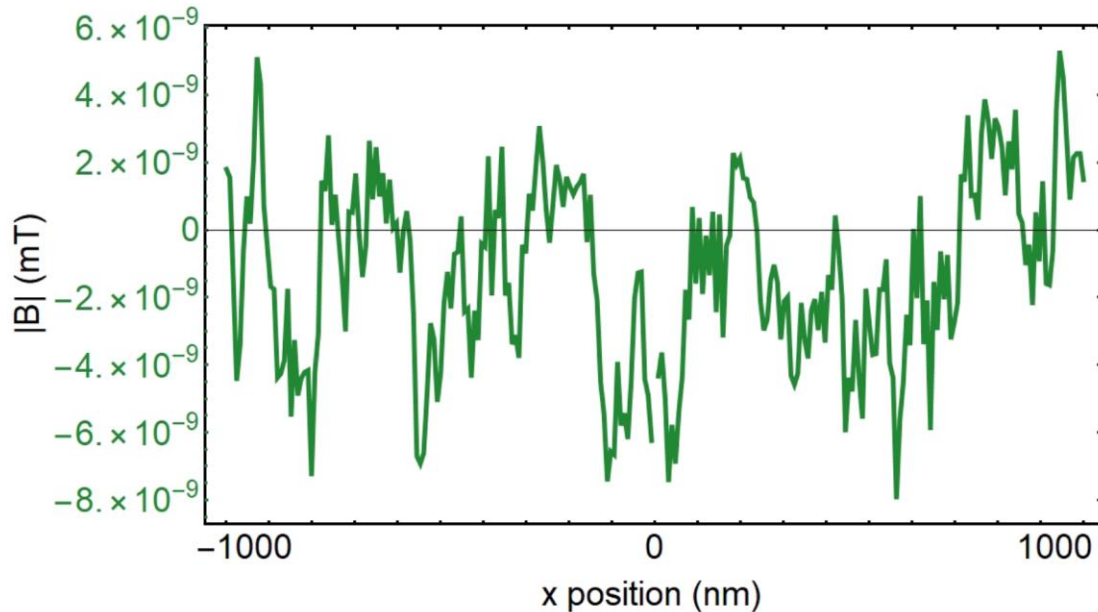

Figure 5.14. B_z field component along the wire for the double Dragonfly with the middle vertical magnet.

5.2.4 Braiding of Majorana Bound States in a T-junction

Braiding of MBSs is considered as a milestone for topological protected quantum computation since this manipulation of MBSs demonstrates the non-Abelian statistics of a Majorana fermion [1, 129]. It is proposed that in a one-dimensional Majorana nanowire model, a T-junction structure can realize the braiding of MBSs [130]. Natively, the geometry of a T-junction is a T-shape combination of two Majorana nanowires. In a one-dimensional wire, particles likely "collide" with each other and a T-shape geometry provides a method for exchanging particles.

We may utilize local magnetic field profiles produced by micromagnets to realize braiding of MBSs in a T-junction. The proposed structure is given in Figure 5.15. For the right and left sections, there are two double Dragonfly setups of magnets, which produce magnetic field profiles along the horizontal nanowire. The design of magnets in the middle section allows a magnetic field along the vertical nanowire. Compared to a globally external magnet field, local field profiles demonstrate the benefit of providing local fields in different directions at different locations. In the middle of the T-junction, we define three gates to control the coupling between different sections of the T-junction, which is indicated by the zigzag lines.

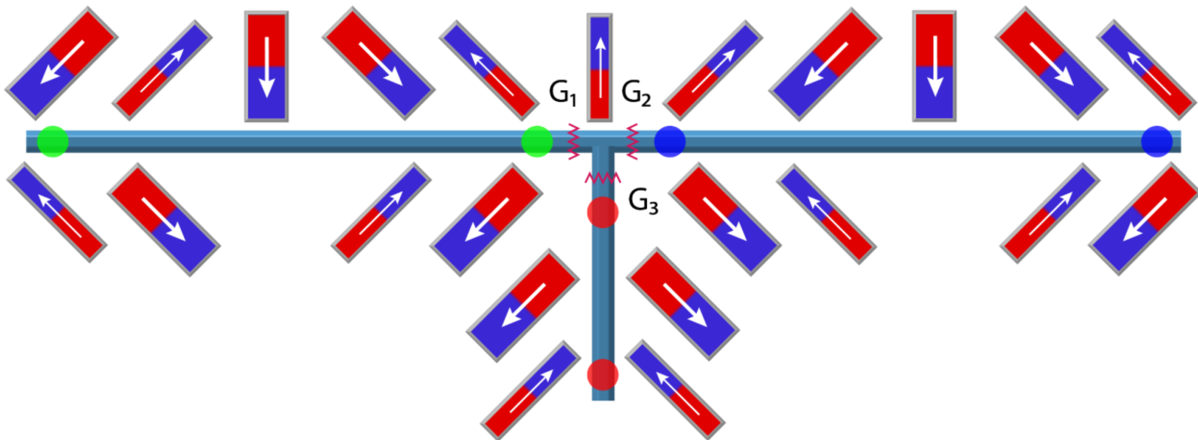

Figure 5.15. T-Junction setup. The top two sections of nanowire are 5000 nm in length in total and the perpendicular section is 1100 nm. Zigzag lines indicate electrostatic gates. Circles indicate desired positions of 6 MBSs with all gates on.

With an additional 40 mT of external magnetic field in *y*-direction, possible manipulations of MBSs are shown in Figure 5.16. First, if we use the three gates to pinch-off the corresponding local nanowire sections, the three sections of the T-junction are separated and there are three isolated Majorana nanowires. For each nanowire, there is a pair of MBSs indicated by colors and

shown in Figure 5.16 (a). In Figure 5.16 (b), G_3 still isolates the vertical nanowire but G_1 and G_2 are deactivated to couple the right and left section. The combination of the two sections is a long horizontal Majorana nanowire. The red color indicates the lowest energy state localized at the two ends of the horizontal nanowire, which is the pair of MBSs. There is a higher energy state (green) close to the middle of the nanowire. This is a pair of nearby MBSs. We can also couple the right section with the vertical section, isolating the left section or couple the left section with the vertical section, isolating the right section. These are shown in Figure 5.16 (c) and (d). Especially in Figure 5.16 (d), the blue wavefunction extends over the left and vertical section. Due to this extension of wavefunction, we observe purple states located at the end of the left and vertical sections. In Table 1, the energies of MBSs in Figure 5.16 are summarized. These simulations demonstrate the possibility to realize braiding in a T-junction with local magnetic field profiles. Though, the configurations of micromagnets are complicated and the feasibility is to be tested.

The local magnetic field profiles for this T-junction setup are available in Figure 5.17. The field profile for the horizontal nanowire is a complicated rotation field, but with symmetry about the middle of the nanowire. This field profile is not easily realized by applying external fields. This inspires us new possibilities of searching for MBSs by designing micromagnet patterns.

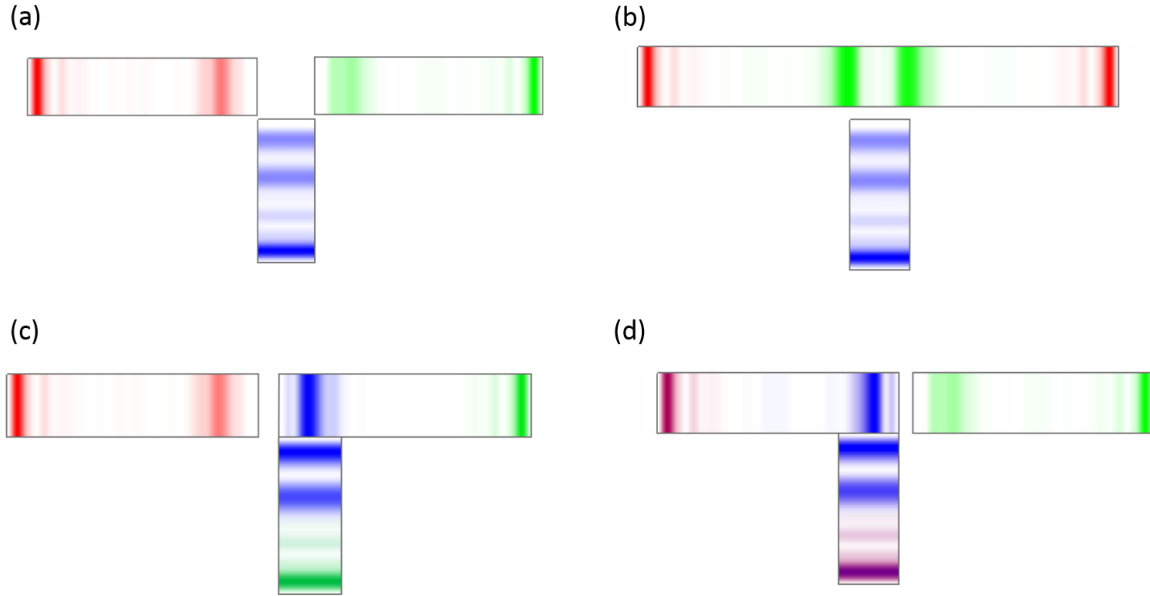

Figure 5.16. Probability distributions (color) of the ground, second and third lowest energy with (a) all gates (b) gate G_3, (b) gate G_1, (c) gate G_2 activated. Colors chosen so that red wavefunction always has a weight on the left end.

Table 5.1. Energies of MBSs in Figure 5.16

Energies of setup /*Δ*	(a)	(b)	(c)	(d)
E_0	1.6×10^{-3}	1.6×10^{-5}	3.5×10^{-4}	7.2×10^{-4}
E_1	2.3×10^{-3}	9.4×10^{-3}	1.6×10^{-3}	2.3×10^{-3}
E_2	9.4×10^{-3}	4.2×10^{-2}	4.3×10^{-3}	3.1×10^{-3}
E_3 (not shown)	1.5×10^{-1}	1.1×10^{-1}	1.3×10^{-1}	1.2×10^{-1}

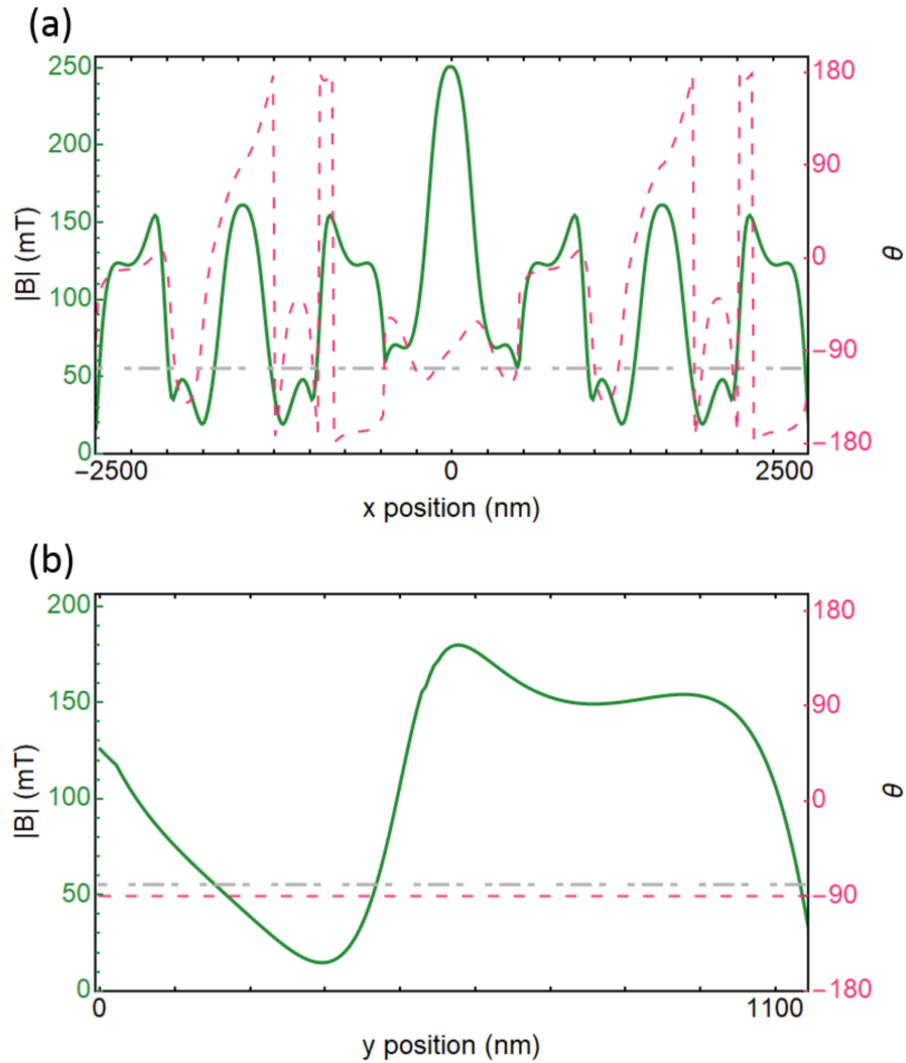

Figure 5.17. (a) Magnetic field of top wire for T-Junction. (b) Magnetic field in the T-Junction leg (vertical segment of nanowire). There is an external field of 40 mT applied in positive y-direction.

5.3 Preliminary Evaluation of Magnetization Pattern from Magnetic Force Microscopy

To evaluate the feasibility of the micromagnet setup for the T-junction, we perform magnetic force microscopy (MFM) to visualize magnetizations of micromagnets. For a

preliminary evaluation, we fabricate CoFe strips shown in the middle part of the setup in Figure 5.15. The CoFe strips are 20 nm thick to reduce magnetic signals and acquire higher resolution for imaging. Separate SQUID measurements show that for the antiparallel configuration of two strips with different dimensions, the required external field is between 15 mT and 20 mT. This agrees with the order of coercive fields inferred from Chapter 4. The CoFe patterns are imaged by atomic force microscopy (AFM) and an example is shown in Figure 5.18 (a). From the ATM image, the fabrication of CoFe strips is still far from perfect. Better e-beam writers with higher resolution may increase the fabrication quality.

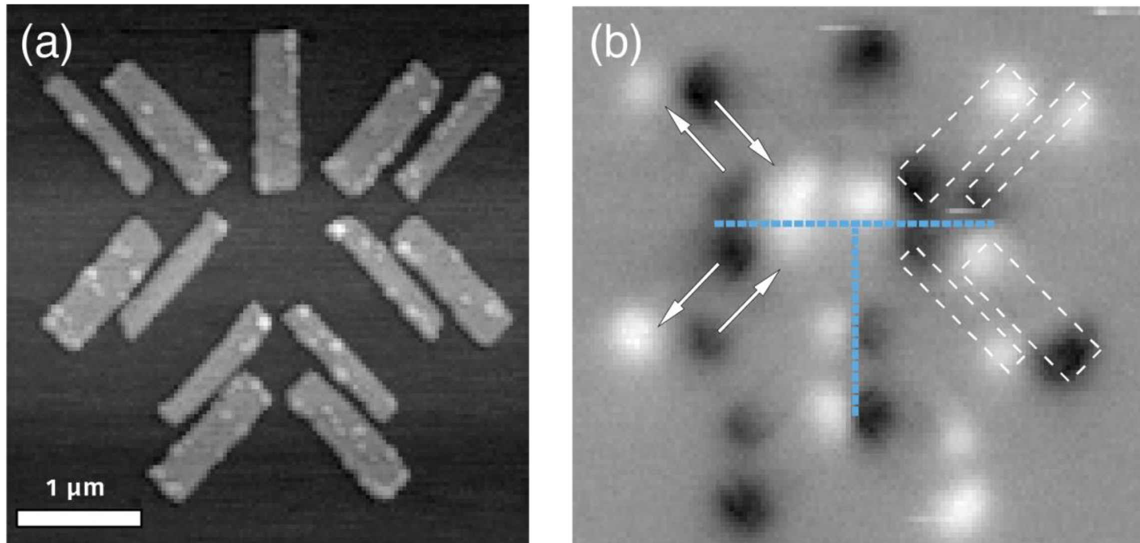

Figure 5.18. (a) Atomic force microscopy (AFM) of a T-junction setup with three Dragonfly magnet configurations. Magnetic film thickness is 20 nm. (b) Magnetic force microscopy (MFM) data on a different T-Junction of the same design. Arrows indicate magnetization direction; white dashed lines are example of magnet dimensions. Blue dashed line is where the Majorana nanowire is envisioned. The magnetic history was a magnetizing field from 100 mT to -16 mT to 0 mT applied at 45-degree direction, then 100 mT to -16 mT to 0 mT at 135 degrees.

An image from MFM is given in Figure 5.18 (b). Not all of the CoFe strips have the required magnetization shown in Figure 5.15. For the 24 patterns fabricated, we report 6 of 72 total Dragonflies with the required configuration of magnetization. More data are shown in Figure 5.19. For the fabrication we imaged by MFM, the yield of correct magnetization is still low. The magnitude of local magnetic fields is not large for small and thin magnets. These may challenge the feasibility of observing MBSs in a one-dimensional nanowire device. We may need better fabrication from e-beam writers with higher resolution and deposit thicker ferromagnet materials. We may also search for other ferromagnetic materials for more stable magnetization. Alternative designs of micromagnet patterns may also be considerable.

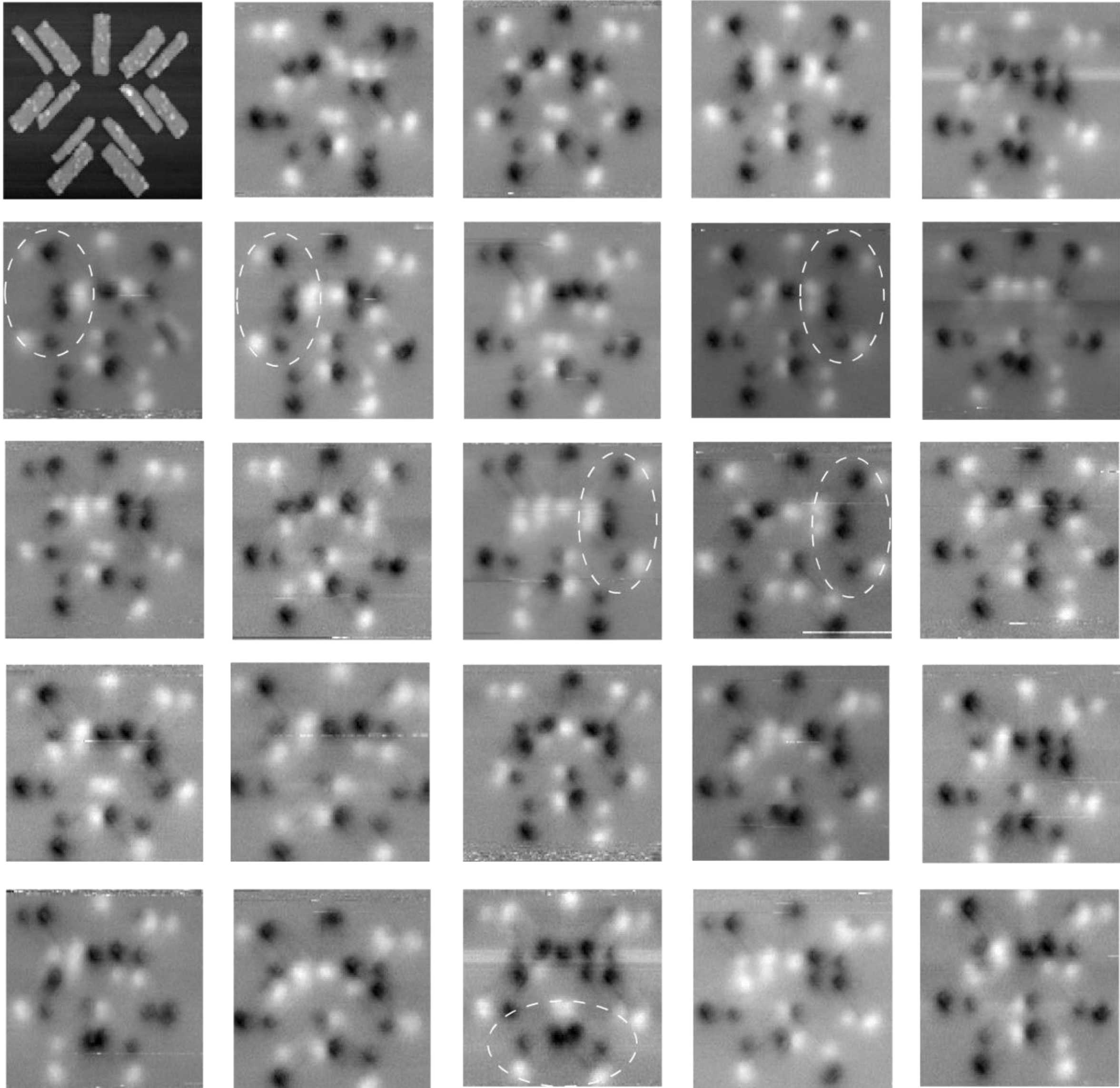

Figure 5.19. Magnetic force microscopy (MFM) data on 24 T-junction setups using three Dragonfly's. The magnet dimensions are the same as in Figure 5.4 but the distance between them differs. Top left: Atomic force microscopy (AFM) of one T-junction setup with three dragonfly magnet configurations. Magnetic film height 20 nm. Dashed ovals point out magnetizations favorable for generating MZM. The magnetic history was a magnetizing field from 100 mT to -16 mT to 0 mT applied at 45-degree direction, then 100 mT to -16 mT to 0 mT at 135 degrees.

6.0 Andreev Bound States under Local Magnetic Field Profiles

As discussed in Chapter 2, a hybrid superconductor-semiconductor nanowire device is a predicated platform of MBSs. Such a hybrid device requires a semiconductor nanowire with strong spin-orbit interaction and Zeeman field to lift spin degeneracy of electron states. For my search, I have access to InSb and InAs nanowires which have strong spin-orbit interaction. Moreover, advanced grown techniques enable in situ growth of high-quality superconductor contacts to the InSb and InAs nanowire (see Chapter 3). Zeeman field can be applied through superconducting coils installed on a dilution refrigerator. At low temperature inside a dilution refrigerator, quantum transport measurement for MBSs becomes a feasible task given the above components.

In this chapter, we will discuss preliminary investigation of MBSs in hybrid superconductor-semiconductor nanowire devices under local magnetic field profiles generated from micromagnets. This idea is introduced in Chapter 5, which is expected to support MBSs under zero external applied magnetic field. Data from our experiments demonstrate Andreev levels inside the induced superconducting gap, suggesting existence of quantum dots coupled with superconductivity. Additionally, visually long ZBPs under zero external magnetic field are observed. We also demonstrate an example that a ZBP has plateau-like features and the magnitude of the plateau is close to $0.5G_0$ (G_0 is the conductance quantum). We observe MBS-like features of energy states inside the induced superconducting gap. Nevertheless, MBSs and ABSs may share similar features and we attribute observed ZBPs to topologically trivial ABSs. Even though we cannot confirm any MBSs from ZBPs, the idea of local magnetic field profiles from micromagnets provides promise in study of MBSs in hybrid superconductor-semiconductor nanowire devices or other platforms.

6.1 Superconductor-semiconductor-superconductor Junctions

In a S-N-S nanowire junction, supercurrents may be developed through the junction. This is a Josephson junction, and we expect that the supercurrents are sensitive to magnetic fields. In fact, a Josephson junction is a basic component of a superconducting quantum interference device (SQUID) which is sensitive to small magnetic fields [131]. When micromagnets are placed close to a S-N-S nanowire junction, the local magnetic field effect discussed in Chapter 4 is to be observed. If supercurrents are injected into a S-N-S nanowire junction, we expect to observe hysteretic supercurrents under magnetic field scans. When a voltage bias is applied across the junction, we expect to observe an induced superconducting gap. If there is a quantum dot in this junction, ABSs may also appear.

6.1.1 S-N-S Junctions Based on InSb Nanowires

By a shadow technique (see Chapter 3), InSb nanowires can be grown with superconducting Sn contacts in situ. Measurements of high-quality S-N-S junctions based on these nanowires demonstrate large induced superconducting gap and gate-tunable supercurrents [81]. The induced gap is hard and resilient to magnetic fields as large as 2 T. Given the condition that experiments in this thesis are performed under low magnetic fields (hundreds of mT), these InSb nanowires are decent for our experiments. Devices can be fabricated straightforwardly by deposition of Ti/Au leads to Sn covered sections, with pre-processing to remove oxide layer covered on the nanowire. The nanowire is placed on a back-gate chip for chemical potential tuning. The schematic of a S-N-S nanowire junction is shown in Figure 6.1 (a) and a SEM image of a typical device is shown in Figure 6.1 (b).

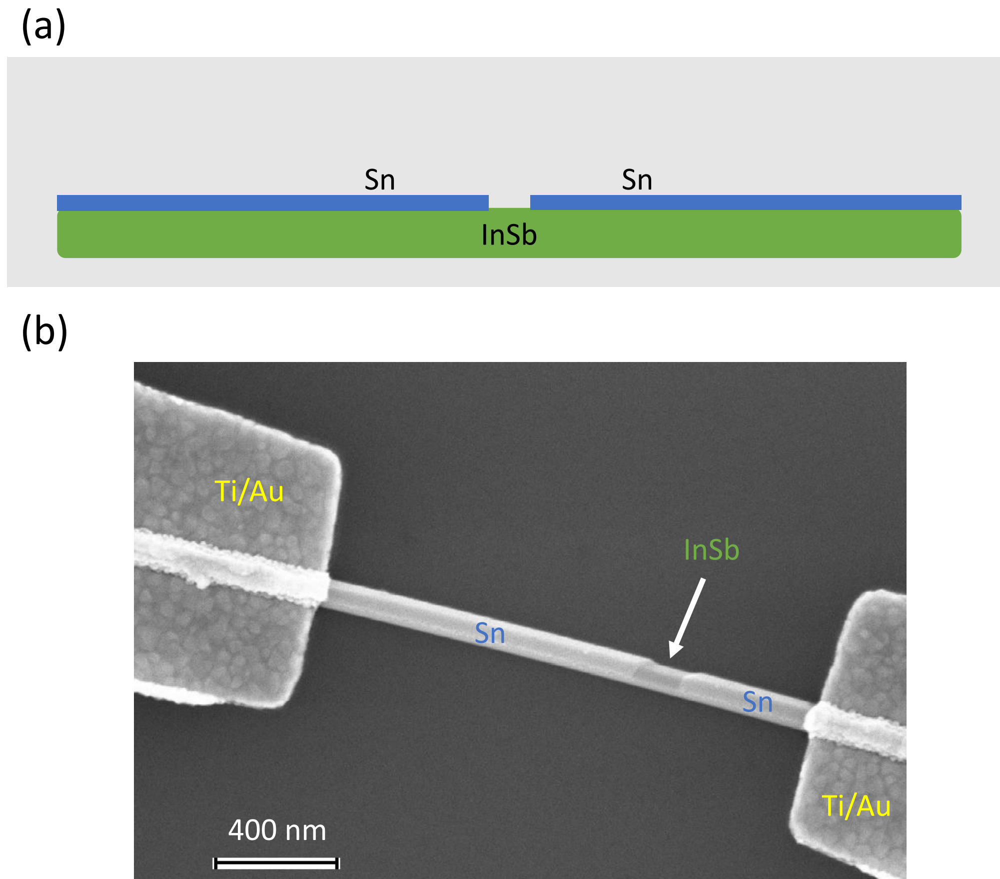

Figure 6.1. (a) Schematic of an InSb S-N-S junction device. (b) A SEM image of an InSb S-N-S device, SNS_1. A back gate is underneath.

To test the properties of device SNS_1, a voltage bias (V) is applied across the two Ti/Au leads and current through the nanowire is monitored at the base temperature inside a dilution refrigerator. The back gate (V_g) underneath the nanowire can tune the chemical potential of the device. Corresponding data are plotted in Figure 6.2 (a). Overall, the plot is quite noisy and there are many random charge jumps. Nevertheless, we can observe gap-like features which should be induced by Sn. Interestingly, there are energy states appearing inside the gap. These states have the loop-like features commonly attributed to Andreev levels [54]. The observation of ABSs indicates that in this S-N-S device, there are quantum dots coupled with superconducting Sn. This

strongly proves the superconducting proximity. In Figure 6.2 (b), we demonstrate another example of loop-like features from Andreev levels, which is measured in another device (device SSN_2). Observation of ABSs shows promise for detecting MBSs in these devices since there are also mechanisms for supporting topological states in a S-N-S junction [132]. Unfortunately, as shown in Figure 6.2, the S-N-S devices are quite noisy and it is pretty difficult to replicate desired energy states. This poses significant negative influence on future investigation of energy states in these devices. We may need better fabrication methods to improve S-N-S devices. Nevertheless, we may still use these devices to test local magnetic field effect by adding micromagnets.

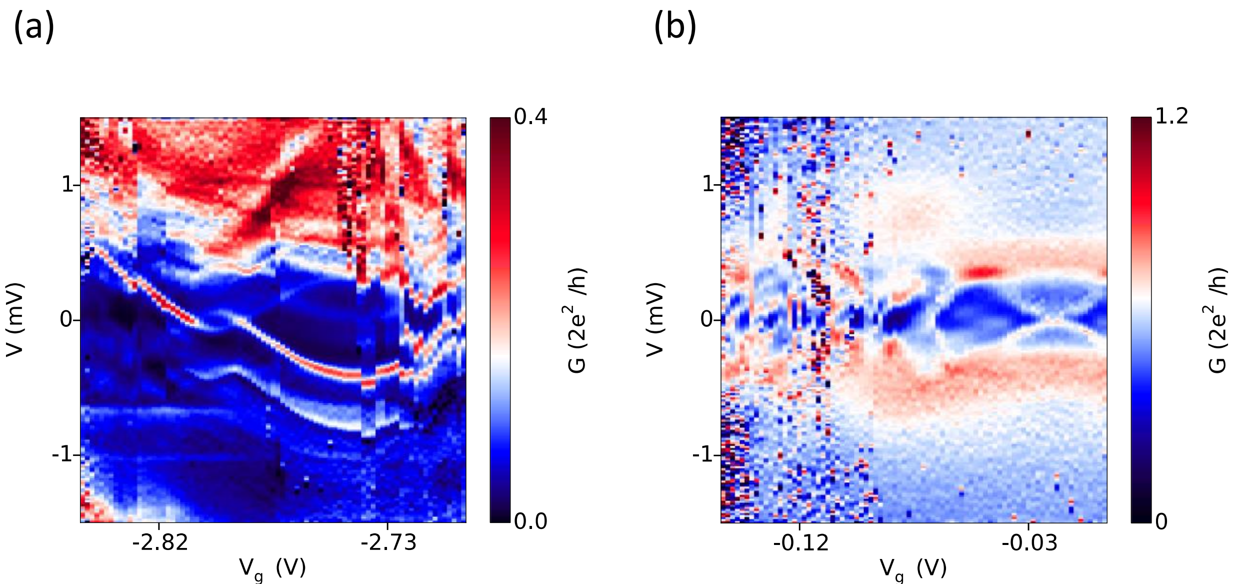

Figure 6.2. Scans of bias voltage (*V*) vs. gate voltage (V_g). (a) Measured in device SNS_1. (b) Measured in device SNS_2.

6.1.2 Hysteresis in S-N-S Devices

For a S-N-S junction, supercurrents can be generated through the junction due to Andreev reflections. If the supercurrents are sensitive to magnetic fields, we may expect to observe local

magnetic field effect if a S-N-S junction is under local magnetic field profiles generated from micromagnets nearby.

To demonstrate local magnetic field effect in a S-N-S junction, we fabricate devices similar to the devices shown in Figure 6.1 and add CoFe strips close to junctions. When the CoFe strip is magnetized, the local magnetic field from the strip penetrates the S-N-S junction. To demonstrate supercurrents through the nanowire, we apply current bias (I) and monitor voltage across the device.

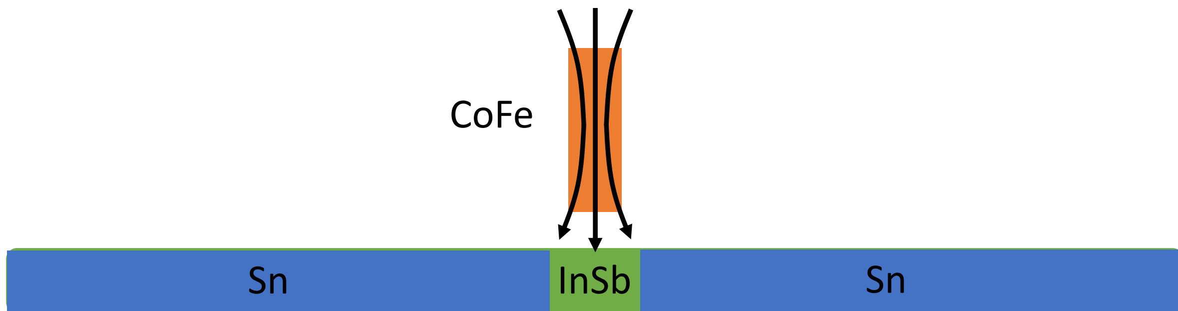

Figure 6.3. Schematic of an InSb S-N-S junction device with a CoFe strip. Stray field from a magnetized CoFe may penetrate the nanowire device, as indicated by arrows.

Figure 6.4 (a) shows a particular device (device SNS_3) which occasionally has two S-N-S junctions. Two CoFe strips are deposited close to each junction. From the SEM picture, there is an additional nanowire that does not contribute to any transport since not all the Ti/Au leads contact to it. This additional nanowire is from the difficulty to separate two nanowires during transferring to back-gate chips. To reduce confusion, schematics of this device are given in Figure 6.4 (b) and (c), which demonstrate more details of the device structure.

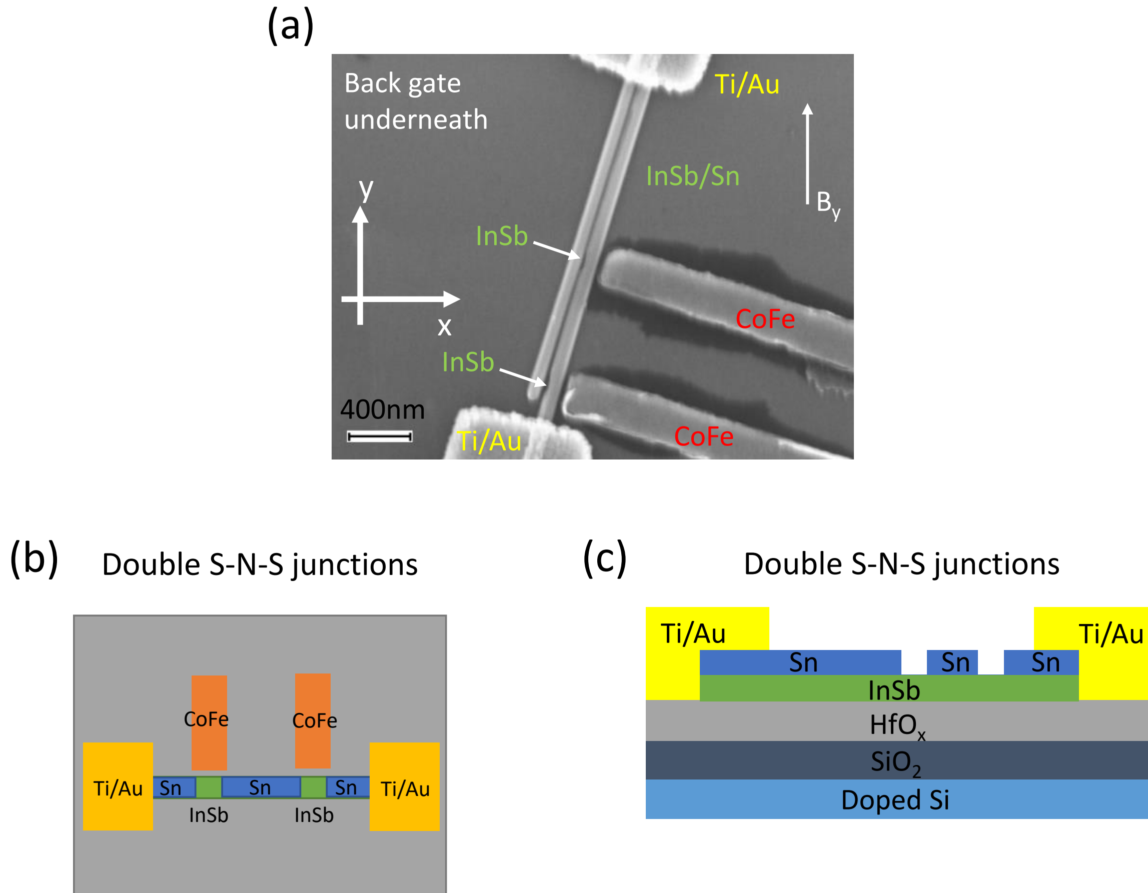

Figure 6.4. An InSb nanowire device (device SNS_3) with two S-N-S junctions. (a) A SEM image of device SNS_3. The direction of the applied magnetic field is given by the arrow. (b) Top-view schematic of device SNS_3. (c) Cross-section of the double S-N-S junctions.

We first apply an external magnetic field of -0.2 T in B_y direction to magnetize the CoFe strips. After that, the external magnetic field is set back to zero. By injecting current and tuning the back-gate voltage (V_g), we observe gate-tunable supercurrent in Figure 6.5. By taking differential resistance from the measured voltage, we observe two prominent lines (indicated by arrows) with varying magnitude depending on V_g. These correspond to the switching current. Within the gate voltage shown in this figure, the magnitude of allowed supercurrent through the

junction is getting larger. Supercurrents developed through a semiconductor by the superconducting proximity are gate-tunable.

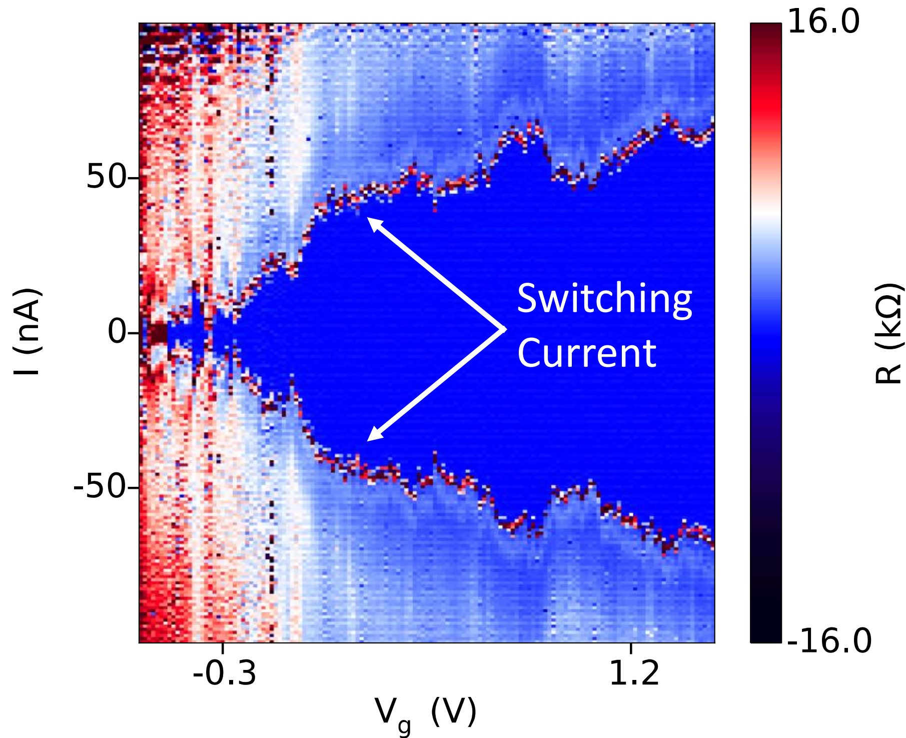

Figure 6.5. 2D plot of injected current (*I*) with respect of gate voltage (V_g) in device SNS_3. Resistance is acquired by taking differential of measured voltage and extracting input resistance. The switching current is indicated by arrows.

From magnetic field scans of the supercurrents developed in device SSN_3, we demonstrate local magnetic field effect by observation of hysteresis. In Figure 6.6, hysteretic supercurrent is presented by sweeping magnetic field in the *y*-direction. In Figure 6.6 (a), the magnetic field is swept from -0.2 T to 0.2 T. The switching current keeps increasing with a more positive magnetic field before a sharp drop. This sharp drop is from the switching of magnetization direction of CoFe strips. Larger magnetic field in the junction suppresses the supercurrent

developed in the S-N-S junction. Before reaching the coercive field of the micromagnets, local magnetic fields from the CoFe strips compensate for the applied positive magnetic field. The switching of magnetization direction after coercive field is sharp and results in a prominent dropping of supercurrent since local magnetic fields now enhance the applied magnetic field. There are also two extra white curves presented in the plot. This may come from multiple Andreev reflections [133]. In Figure 6.6 (b) where the external magnetic field is swept from 0.2 T to -0.2 T, the story for sharp switching from magnetization of CoFe strips is the same. In Figure 6.6, we observe hysteretic supercurrents and successfully demonstrate local magnetic field effect in a S-N-S junction.

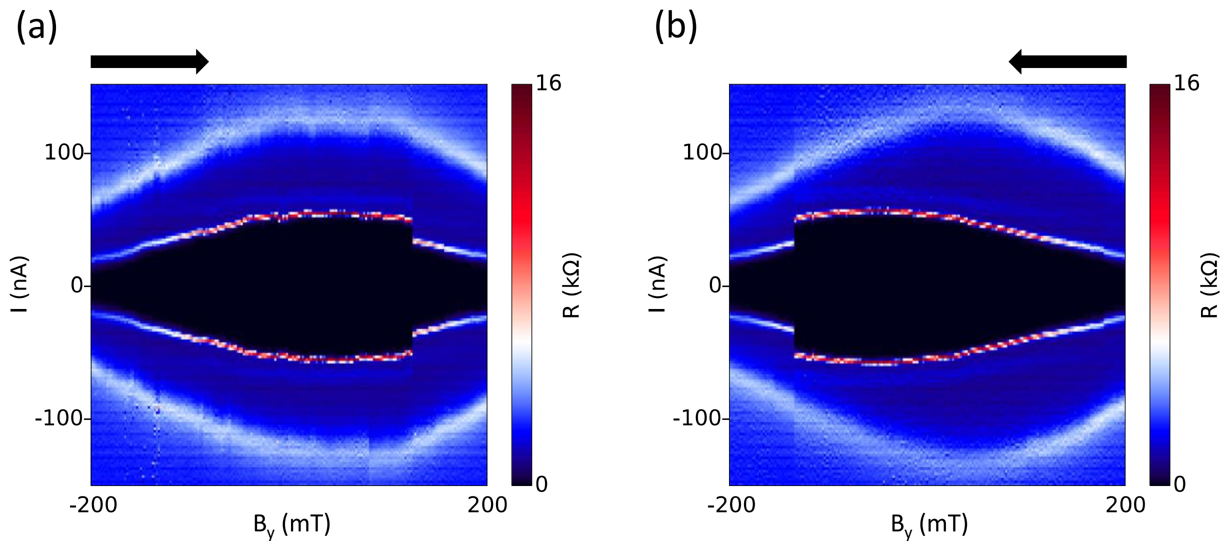

Figure 6.6. 2D plots of injected current (*I*) with respect to magnetic field (B_y) in device SNS_3. V_g = 3 V. (a) B_y is swept from -0.2 T to 0.2 T. (b) B_y is swept from 0.2 T to -0.2 T.

The direction of the applied magnetic field is not along the easy axis for magnetization of CoFe strips. Nevertheless, the magnetic field scans still demonstrate sharp switching of

supercurrents, indicating that there is a relatively stable magnetization resisting to the external magnetic field. In Figure 6.7, we show hysteretic supercurrent when the applied magnetic field is in the *x*-direction. Again, we observe clear hysteretic supercurrents. There are multiple sharp switches of supercurrents in the plots. The coercivity of the two CoFe strips may be different or the double junctions may introduce more complicated mechanisms. There are also extra white curves appearing in these plots, which are still likely from multiple Andreev reflections. The location of sharp switching in Figure 6.7 and Figure 6.6 is different because CoFe strips have different coercive fields for external magnetic fields applied in different directions. Overall, we confirm the existence of local magnetic field profiles in the nanowire devices.

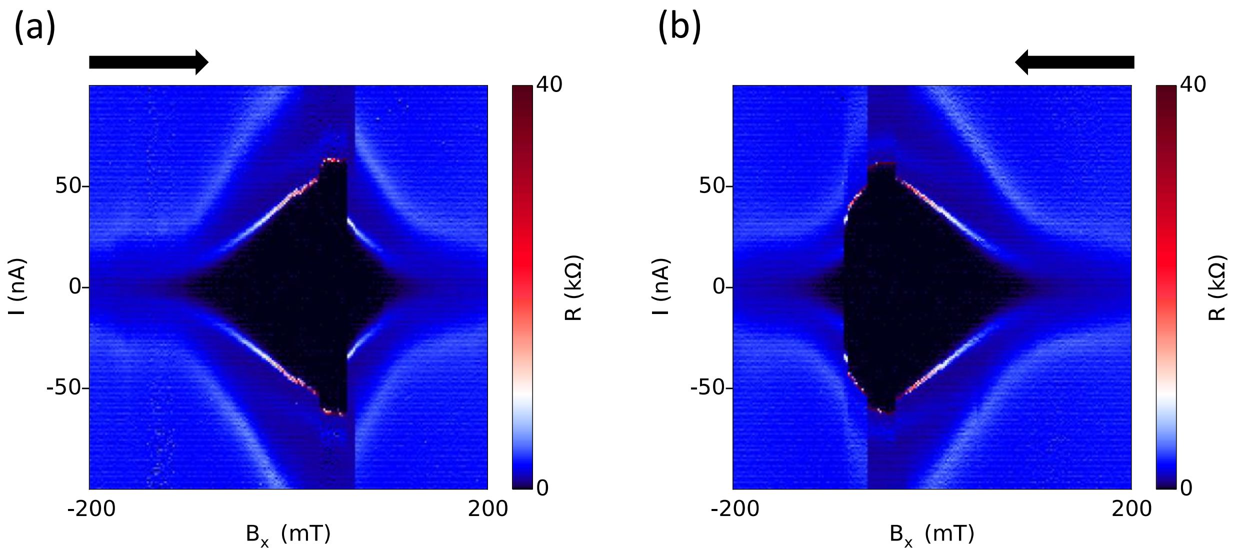

Figure 6.7. 2D plots of injected current (I) with respect to magnetic field (B_x) in device SNS_3. V_g = 3 V. (a) B_x is swept from -0.2 T to 0.2 T. (b) B_x is swept from 0.2 T to -0.2 T.

6.2 Superconductor-semiconductor Junctions

A nanowire S-N junction device is a typical structure used in experiments for MBSs. Following the basic device structure, we fabricate S-N junction devices based on InAs nanowire. An InAs nanowire has smaller spin-orbit interaction than an InSb nanowire. However, it is still believed to be a promising candidate for demonstrating MBSs. When micromagnets are deposited close to an S-N junction, local magnetic field effect should also play a role in these devices.

6.2.1 S-N Junctions Based on InAs Nanowires

To fabricate a S-N junction, InAs nanowires with an in situ grown layer of superconducting Al [82] are transferred onto a back-gate chip. A portion of Al layer is removed from a nanowire by chemical etching. By deposition of Ti/Au leads, a S-N junction or a common MBS device is fabricated. To introduce local magnetic fields, CoFe strips are deposited close to the junctions. In Figure 6.8, we show a SEM image of a typical device (device SN_1) with the schematic of the device structure. This particular device has two CoFe strips and the upper strip is also used as a side gate (V_{sg}). The misalignment of the two CoFe strips is intentionally designed for a stronger local magnetic field profile around the S-N interface. For each particular device, there is freedom to design the CoFe strips for stronger local magnetic field and better chemical tuning of the device.

To characterize device SN_1, a voltage bias is applied across the Ti/Au leads and current through the junction is monitored. By tuning of side-gate voltage, we may observe Andreev levels which can be attributed to three cases: weak-coupled, strong-coupled and the boundary between weak-coupled and strong-coupled [54]. In Figure 6.9 (a), we first apply a -0.2 T external magnetic field of B_θ where $\theta = 44^o$ to pre-magnetize the CoFe strips. After that, the external magnetic field

is swept back to 0 and the data are taken at zero external magnetic field. We observe loop-like features for the energy states appearing inside the induced superconducting gap. Recall from Chapter 2, the ground state energy changes from singlet (large loop) to doublet (small loop) and back to singlet (large loop). Figure 6.9 (a) demonstrates Andreev levels corresponding to the weak-coupled case. In this device, the observation of ABSs indicates there are quantum dots coupled with the superconducting Al.

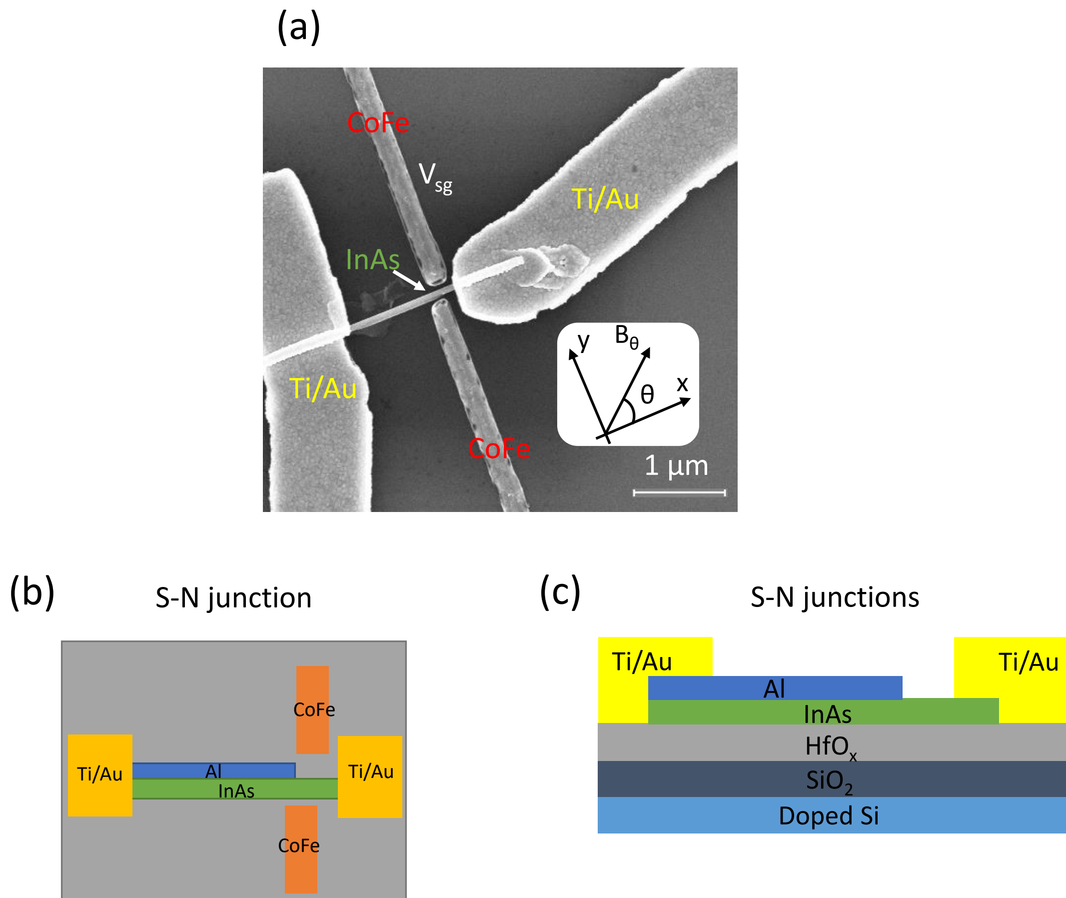

Figure 6.8. An InAs nanowire device (device SN_1) with one S-N junction and two CoFe strips. (a) A SEM image of device SN_1. The upper CoFe strip is also used as a side gate (V_{sg}). (b) Top-view schematic of device SN_1. (c) Cross-section of the S-N junction.

In Figure 6.9 (b), we pre-magnetize the CoFe strips using the same method as described for Figure 6.9 (a). By tuning side-gate voltage under zero external magnetic field, we observed energy levels corresponding to the case that is between weak-coupled and strong-coupled. Similarly, we observe the Andreev levels corresponding to the strong-coupled case in Figure 6.9 (c). In the case of Figure 6.9 (a) and (b), the crossing of Andreev levels results in ZBPs appearing inside the induced gap at zero external magnetic field. These ZPBs are topologically trivial and there is no strong evidence to relate them to MBSs.

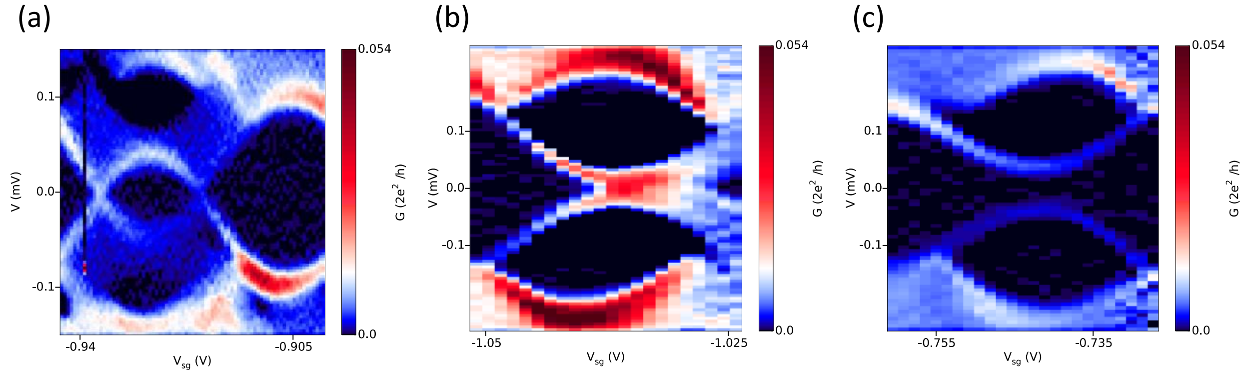

Figure 6.9. 2D plots of voltage bias (*V*) with respect of side-gate voltage (V_{sg}) in device SN_1. Conductance is acquired by taking differential of measured current. The CoFe strips are pre-magnetized by applying a -0.2 T magnetic field B_θ where θ = 44°. After pre-magnetization, the external magnetic field is swept back to zero for taking the data. (a) V_g = 9 V. Weak-coupled case. (b) V_g = 9.75 V. Between weak-coupled and strong-coupled. (c) V_g = 9 V. Strong-coupled case.

We then study the behaviors of ZBPs under magnetic field scans. In Figure 6.10 (a), Andreev levels at zero external magnetic field are plotted with respect to side-gate voltage. For this plot, the CoFe strips are pre-magnetized with a -0.1 T external magnetic field perpendicular to the nanowire (θ = 90°). After the external magnetic field is set back to zero, the CoFe strips

should be magnetized along their easy axes. From the plot, there are loop-like states inside the induced superconducting gap and we observe a ZBP due to the crossing of Andreev levels. This ZBP is hysteretic under magnetic field scans, as shown in Figure 6.10 (b) and (c). From Figure 6.10 (b), there is a sharp switching at positive magnetic field that the ZBP suddenly disappears. This comes from the CoFe strips' magnetization switching when the applied field gets larger than the coercive field. At larger negative external magnetic field, the ZBP splits into two lines. Figure 6.10 (c) basically tells the same story as Figure 6.10 (b). We observe hysteretic ZBPs which split at larger magnetic field.

In Figure 6.11, we demonstrate another example of ZBP at zero external magnetic field. The pre-magnetization process is the same as for Figure 6.10. Again, the ZBP is hysteretic under magnetic field scans. At larger magnetic field, however, the ZBP does not split this time. ZBPs of ABSs may split or not split under certain magnetic fields, which may depend on how Andreev levels react with the magnetic field.

To have a further understanding of ZBPs under magnetic fields, we plot a ZBP under different external magnetic fields shown in Figure 6.12. The pre-magnetization process is the same as for Figure 6.10. From Figure 6.10 and Figure 6.11, we can infer that the coercive field of CoFe strips is larger than 50 mT and a 50 mT external magnetic field does not switch the magnetization directions of the strips. The 50 mT external magnetic field shifts the location of the ZBP with respect to side-gate voltage, which indicates shifting of Andreev levels caused by the magnetic field.

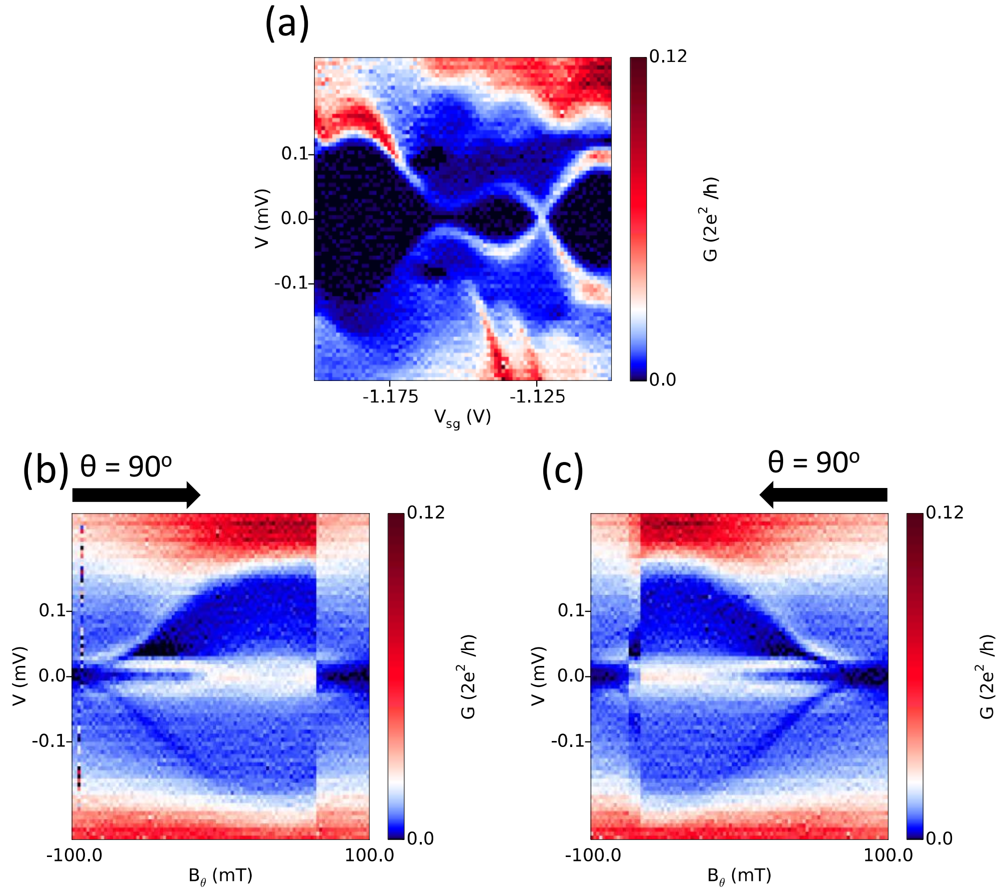

Figure 6.10. ZBP and hysteresis under magnetic field scans. V_g = 10.5 V (a) 2D plots of voltage bias (V) with respect of side-gate voltage (V_{sg}) in device SN_1. Conductance is acquired by taking differential of measured current. The CoFe strips are pre-magnetized by applying a -0.1 T magnetic field B_θ where θ = 90º. After pre-magnetization, the external magnetic field is swept back to zero for taking the data. (b, c) 2D plots of voltage bias (V) with respect of the external magnetic field, B_θ (θ = 90º) in device SN_1. Sweeping direction of magnetic field is given by arrows.

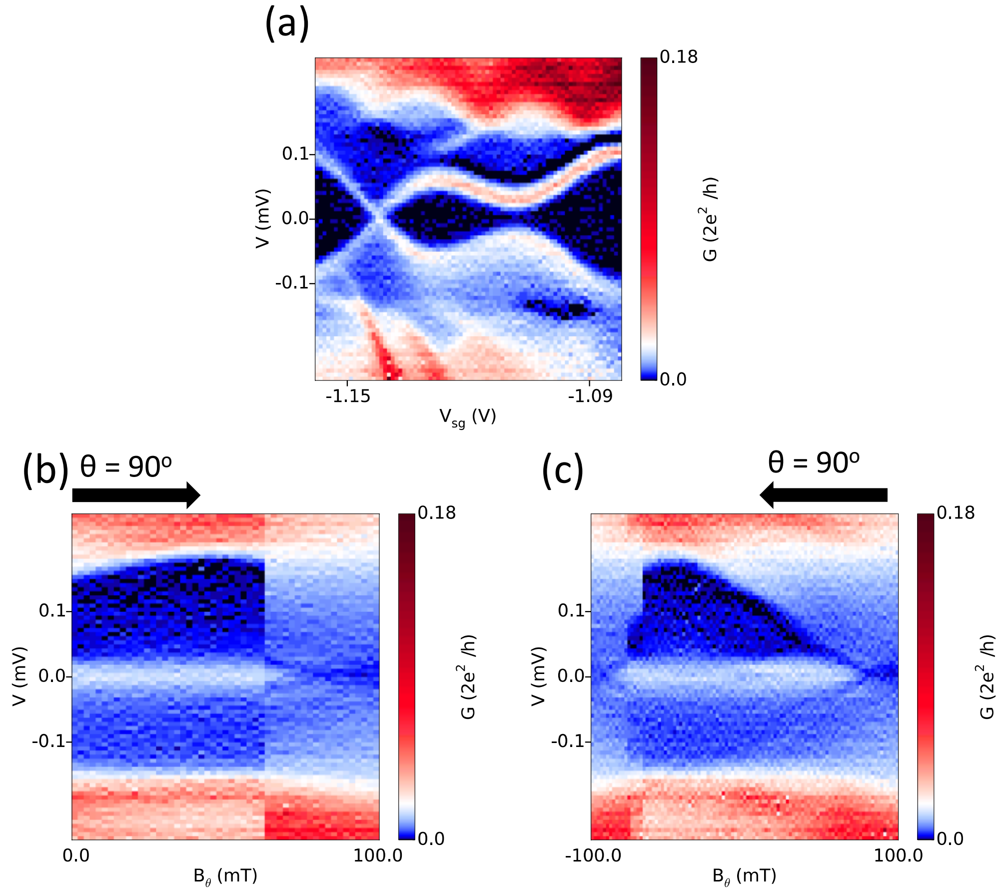

Figure 6.11. ZBP and hysteresis under magnetic field scans. V_g = 10.5 V (a) 2D plots of voltage bias (V) with respect of side-gate voltage (V_{sg}) in device SN_1. Conductance is acquired by taking differential of measured current. The CoFe strips are pre-magnetized by applying a -0.1 T magnetic field B_θ where $\theta = 90^o$. After pre-magnetization, the external magnetic field is swept back to zero for taking the data. (b, c) 2D plots of voltage bias (V) with respect of the external magnetic field, B_θ ($\theta = 90^o$) in device SN_1. Sweeping direction of the magnetic field is given by arrows.

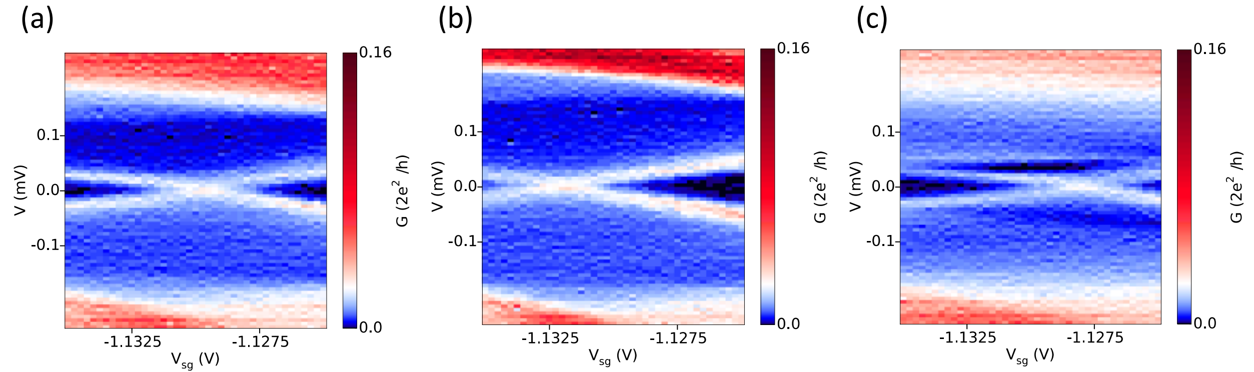

Figure 6.12. 2D plots of voltage bias (*V*) with respect of side-gate voltage (V_{sg}) in device SN_1 at different magnetic fields. Conductance is acquired by taking differential of measured current. The CoFe strips are pre-magnetized by applying a -0.1 T magnetic field B_θ where θ = 90°. After pre-magnetization, the external magnetic field is swept back to zero before taking any new data. V_g = 10.5 V. (a). B_θ = 0 mT. (b) Data acquired by adding a magnetic field that B_θ = 50 mT, θ = 90°. (c) Data acquired by adding a magnetic field that B_θ = -50 mT, θ = 90°.

6.2.2 Visually Long ZBPs in S-N Junctions

The ZBPs shown in above sub-sections are likely from the crossing of Andreev levels in the weak-coupled regime. A ZBP looks like a point located at the crossing point of energy levels when data are taken by varying the side-gate voltage. From the point of view of MBSs, ZBPs due to topological states may extend longer before the chemical potential or magnetic field is out of the topological regime. Even a quantized ZBP plateau is predicted to describe the robustness of the MBSs [60, 61]. This leaves us to the question of whether we can classify ZBPs based on their visual features.

Figure 6.13 (a) shows a SEM image of another InAs superconductor-semiconductor junction device (device SN_2). The structure of device SN_2 is basically the same as device SN_1. Compared to device SN_1, there is no mismatch of the two CoFe strips for device SN_2 and the corresponding local magnetic field profile may be different. Nevertheless, the basic idea is the same. Magnetized CoFe strips generate local magnetic fields and we search for ZBPs under zero applied external magnetic field. Again, CoFe strips can also be used as side gates. It seems that the lower CoFe strip attaches the nanowire or even the right-side Ti/Au lead. However, measurements prove that this lower CoFe strip does not conduct with the nanowire or the right-side Ti/Au lead.

To magnetize the CoFe strips, a -0.2 T magnetic field is applied perpendicular ($\theta = 0^{o}$) to the nanowire and then swept back to zero. The CoFe strips are therefore magnetized along their easy axes. Interestingly, we observe visually long ZBPs (present over an extended range in gate voltage) at zero external magnetic field, given in Figure 6.13 (b). The magnitude of this ZBP is larger than G_0 ($2e^2/h$). ZBPs larger than G_0 are not likely due to MBSs [134]. Instead, the ZBP shown in Figure 6.13 (b) is more likely from trivial ABSs. Local magnetic field suppresses the induced superconducting gap and the energy states inside the gap. When the ABSs are in the boundary between weak-coupled and strong-coupled regimes, visually long ZBPs may appear.

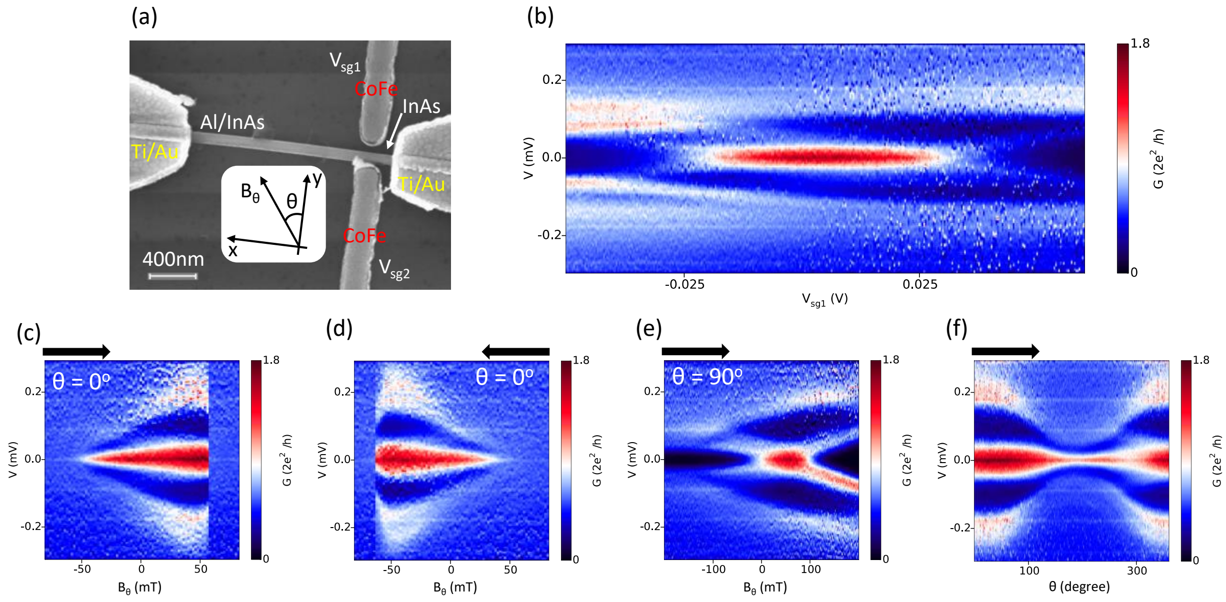

Figure 6.13. (a) SEM image of device SN_2, an InAs nanowire device. This device has an S-N junction and two CoFe strips close to the junction. The two CoFe strips also work as two side gates (V_{sg1} and V_{sg2}). (b) A scan of Vbias (*V*) vs. side-gate voltage (V_{sg1}) measured on device SN_2. The back-gate voltage is 8.25 V and the second side gate voltage (V_{sg2}) is 0 V. The CoFe strips are magnetized in the direction of $\theta = 180^{o}$ and the external magnetic field is 0 T. (c, d) Scans of Vbias vs. magnetic field. The angle of the magnetic field is labeled on the plots. The back-gate voltage is 8.25 V and both side gate voltages are 0 V. Sweeping directions of the magnetic field are given by arrows. (e) Scans of Vbias vs. magnetic field. The angle of the magnetic field is labeled on the plots. The CoFe strips are magnetized in the direction of $\theta = 180^{o}$. The back-gate voltage is 8.25 V and side gate voltages are 0 V. Sweeping direction of the magnetic field is given by an arrow. (f) Scans of Vbias vs. magnetic field at different angles. The magnitude of the external magnetic field is 0.04 T. The back-gate voltage is 8.25 V and both side-gate voltages are 0 V. Sweeping direction of the magnetic field is given by an arrow.

To demonstrate the effectiveness of local magnetic fields, we take magnetic field scans at the location of the ZBP. In Figure 6.13 (c), the external magnetic field perpendicular to the nanowire is swept from -0.2 T to 0.2 T. The ZBP is visually long since this peak is present over an extended range in external magnetic field. This ZBP also gets broader with respect to more positive external magnetic field before reaching the coercive field of CoFe strips. When the external magnetic field is larger than the coercive field of the strips, the magnetization switching causes a sharp change of the measured conductance. From Figure 6.13 (d), we confirm that this ZBP is hysteretic under magnetic field scans and we can infer a consistent coercive field from the sharp switches. To plot Figure 6.13 (e), we first pre-magnetize the CoFe strips using the same process for Figure 6.13 (b). After pre-magnetization, the magnetic field along the nanowire is swept from -0.2 T to 0.2 T at the location of the ZBP. This ZBP persists within a range of magnetic fields before splitting. There is no clear switching observed in this plot, indicating that the magnetization of CoFe along easy axes is stable under an external field of 0.2 T in the direction along the nanowire. When the CoFe strips have been magnetized, a small external magnetic field (0.04 T) in any direction does not induce observable magnetization switching. This is demonstrated in Figure 6.13 (f). The ZBP persists in all the field directions in this case.

In Figure 6.14, we demonstrate that it is possible to observe a ZBP smaller than G_0 and has a feature of plateau. The plots are still generated by device SN_2. The pre-magnetization process is the same as for Figure 6.13 and the ZBP is still measured under zero external magnetic field. The overall feature of Figure 6.14 (a) and Figure 6.13 (b) is quite similar. From the line-cut of the zero-bias, the magnitude of ZBP in Figure 6.14 (a) is smaller than G_0, which is allowed for MBSs [134]. It even shows a plateau-like feature around $0.5G_0$. Nevertheless, there is no strong evidence that this ZBP comes from MBSs. The magnitude of ZBPs due to ABSs may have values smaller

than, larger than or equal to G_0 [13, 63]. It should be possible for trivial ABSs to demonstrate any ZBPs' features observed in this device. A plateau-like feature can appear occasionally by tuning parameters like chemical potentials.

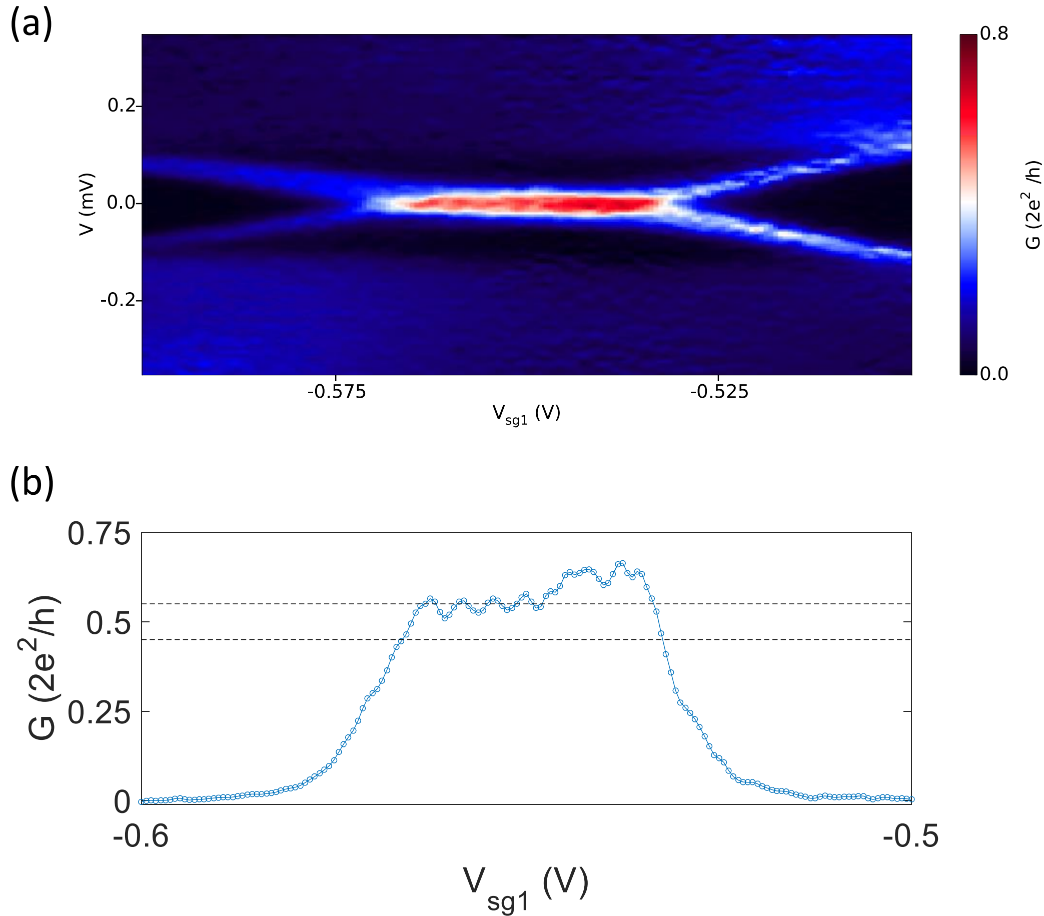

Figure 6.14. (a) A scan of V_{bias} (V) vs. side gate voltage (V_{sg1}) measured on device SN_2. The back-gate voltage is 6.075 V and the second side gate voltage (V_{sg2}) is 0 V. The CoFe strips are magnetized in the direction of θ = 180º and the external magnetic field is 0 T. (b) Line-cut of the differential conductance peak along the first side gate voltage (V_{sg1}) in plot (a).

6.3 More Comments on S-N Junctions

Discussion from the above sections tells us that there are trivial low-energy states inside the induced superconducting gap of S-N junction devices. In this section, we will present supplementary data measured in S-N junctions. This may help readers to establish a more comprehensive view of semiconductor S-N junction devices.

6.3.1 Induced Superconducting Gap and Shift from Measurement Setups

The appearing of energy states inside a gap sometimes requires fine tuning of parameters, for example, gate voltages. Andreev levels only appear at appropriate combinations of parameters. Many 2D scans of V_{bias} with respect to side gate voltage do not show any clear energy states inside the induced superconducting gap. In Figure 6.15 (a) (measured in device SN_2), for example, we observe the induced superconducting gap but there are no energy states clearly identified inside the gap. Based on this plot, the induced superconducting gap is on the order of 0.1 meV, which agrees with other publications [7, 135].

Sometimes, data is shifted due to measurement setup. This is shown in Figure 6.15 (b) that gives the original data set plotted in Figure 6.15 (a). The true zero-bias is shifted away. For plotting Figure 6.15 (a), we locate the true zero-bias by identifying the center of the induced gap and shift the true zero-bias back. For different measurement setups, the shift of data may be different. Since experiments are performed under low-bias and the features around zero-bias are important, we need to take account of possible shifts from measurement setups.

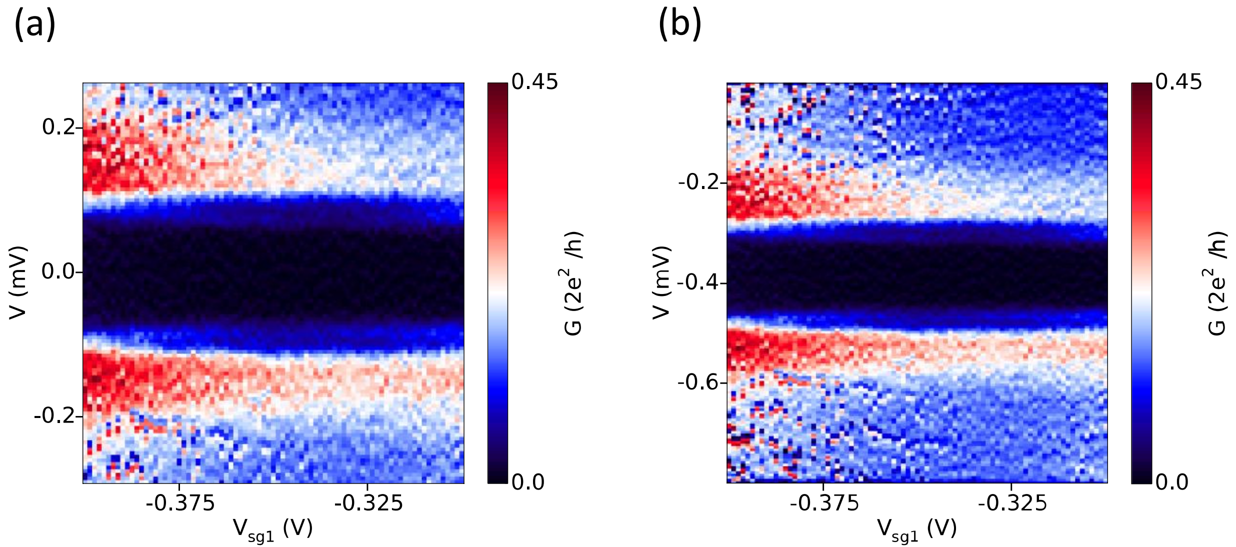

Figure 6.15. Scans of V_{bias} (V) vs. side gate voltage (V_{sg1}) measured on device SN_2. Vg = 7.5 V. Data are taken at zero external magnetic field. The CoFe strips are magnetized using the pre-magnetization process for Figure 6.13 (a). (a) Induced superconducting gap. (b) The plot uses the same data set as in (a). Offset from measurement setup and data at larger bias are not extracted.

6.3.2 Charge Jumps

Charge jumps are common in semiconductor nanowire devices discussed in this thesis. A charge jump may occur anytime and it poses a negative influence on the stability of a device. After a charge jump, sometimes a state will change and it may never come back. Typical charge jumps may bring prominent features. Especially for devices with micromagnets, features induced by magnetization switching are also prominent. Therefore, for magnetic field scans, we need observation of repeatable hysteresis to confirm the origin of some features. For example, in Figure 6.16, a charge jump during magnetic field scan occurs. We can identify this unwanted charge jump since the state has changed.

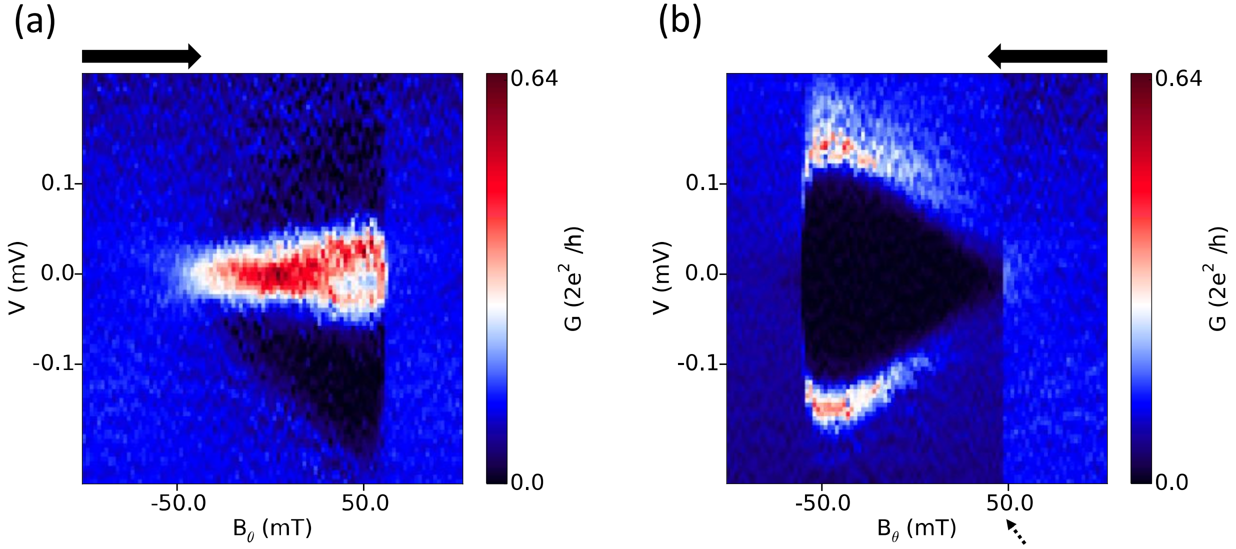

Figure 6.16. 2D plots of voltage bias (*V*) with respect to the external magnetic field, B_θ (θ = 113°) in device SN_2. Sweeping directions of the magnetic field are given by arrows. V_g = 6.075 V. V_{sg1} = -0.56 V. V_{sg2} = 0 V. (a) No charge jump. (b) There is a charge jump (indicated by the small arrow) which changes the original state.

6.3.3 More Examples of ABSs

We demonstrate visually long ZBPs with respect to side gate voltage in device SN_2. In this device, typical ABSs corresponding to different regimes are also available. We demonstrate an example from a weak-coupled regime in Figure 6.17. In Figure 6.18, the state can be classified to be in the strong-coupled regime.

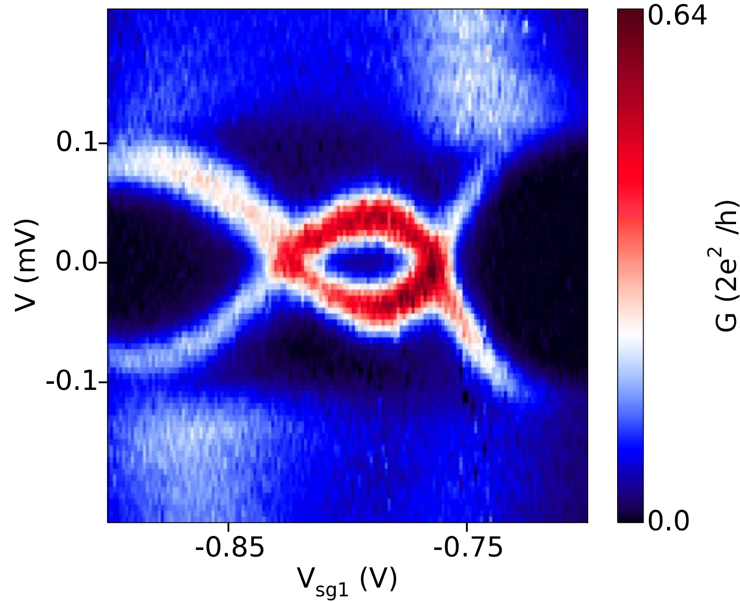

Figure 6.17. Scans of V_{bias} (V) vs. side gate voltage (V_{sg1}) measured on device SN_2. V_g = 6.45 V. V_{sg2} = 0 V. Data are taken at zero external magnetic field. The CoFe strips are magnetized using the pre-magnetization process described for Figure 6.13 (b).

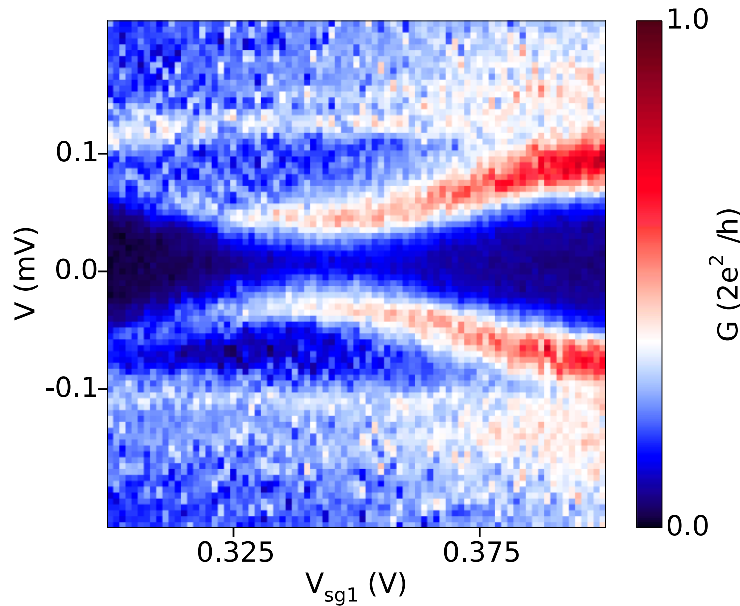

Figure 6.18. Scans of V_{bias} (V) vs. side gate voltage (V_{sg1}) measured on device SN_2. V_g = 6.075 V. V_{sg2} = 0 V. Data are taken at zero external magnetic field. The CoFe strips are magnetized using the pre-magnetization process described for Figure 6.13 (b).

6.3.4 ZBPs, MBSs and ABSs

Readers may have noticed the difficulty of confirming the existence of MBSs in a semiconductor nanowire S-N junction device. In fact, we may just attribute observed ZBPs to trivial ABSs. There seems to be no limitations to ABSs presenting features of plateaus with magnitude smaller than, larger than or equal to G_0. Even though demonstration of this may require fine tuning of parameters, there are no essential obstacles to access these states. On the other hand, to observe MBSs, it needs a small range of appropriate parameters to meet the topological criteria. It is difficult to judge if the device has entered the topological regime just based on observation of ZBPs.

Since MBSs appear as correlated pairs, colleagues have performed experiments attempting to observe the MBS pair simultaneously [13]. In these experiments, there is no such pair of MBSs observed to induce ZBPs simultaneously. Unfortunately, the observed ZBPs due to trivial ABSs share the features predicted for MBSs, just as we discussed in this chapter.

Despite the issue of confirming any MBSs, local magnetic fields generated from micromagnets indeed allow visually long ZBPs in an MBS device. This shows promise for future experiments aiming at MBSs.

7.0 Conclusions and Outlook

In this chapter, we will first summarize my thesis and then discuss the development for searching MBSs. I will also give my personal outlook on the future investigation of MBSs.

7.1 Conclusions of the Thesis

We have discussed the basic theoretical background of MBSs in a quantum wire model in Chapter 2. As topological non-trivial states, MBSs may appear in a one-dimensional quantum wire coupled with *p*-wave superconductivity [3] and should be protected by the bulk gap of the wire. Due to the difficulty of finding a natural *p*-wave superconductor, a more realizable model [4, 5] based on semiconductor nanowires is proposed and attracts efforts of experiments. Additionally, we discussed other concepts involved in a semiconductor nanowire device: quantum dots and ABSs. Especially, we also introduced the concept of ferromagnets since they are components for providing local magnetic fields in my devices. In Chapter 3, we explained how experiments may be performed for MBSs in semiconductor nanowire platforms by quantum transport measurements and other experimental methods. Device fabrication was introduced, and more detailed fabrication processes can be found in the Appendix.

In Chapter 4, we discussed experiments of simple semiconductor nanowire devices with ferromagnetic contacts. From measurements under magnetic fields, we observed hysteretic magnetoresistance with sharp switching due to coercive fields of ferromagnets. The features of measured hysteretic signals agree to some extent with expected features when there is injection of

spin-polarized current. However, in simple nanowire devices with normal contacts but without ferromagnetic contacts, similar hysteretic signals still appear by placing micromagnets near the devices. This confirms that local magnetic fields produced from micromagnets may penetrate semiconductor nanowires and induce hysteresis. Unfortunately, for devices with ferromagnetic contacts, any observed hysteresis may come from local magnetic field effect and confirmation of spin injection becomes difficult. Furthermore, numerical simulations of local magnetic fields from the micromagnets are performed and the numerical results basically agree with experimental data. The simulated coercive fields of ferromagnets and generated local magnetic fields are reasonable compared to measured data from experiments.

In Chapter 5, we demonstrated possible methods to use local magnetic fields generated by micromagnets to induce MBSs. Micromagnets can be arranged to provide local magnetic field profiles for MBSs. Several arrangements of micromagnets are provided and numerical simulations demonstrate promising results that MBSs may appear at zero or low external applied magnetic field. Moreover, by using micromagnets, we proposed a method to manipulate MBSs in a T-junction. In this T-junction, we may demonstrate braiding of MBSs, which may be a stronger signature of the existence of MBSs compared to ZBPs. Preliminary experiments were performed to understand the feasibility of magnetizing micromagnets properly. Results from MFM are far from perfect magnetization patterns since most of the micro-magnets are not magnetized in desired magnetization directions. However, I believe that better magnetization patterns can be formed by improving fabrication methods, for example, using a better EBL with higher resolution to write windows with sharper edges.

In Chapter 6, we discussed experiments in S-N-S and S-N semiconductor nanowire junctions. For an S-N-S device with micromagnet, hysteretic supercurrents with sharp switching

are observable and this hysteresis conforms local magnetic field effect from the micromagnets in devices coupled with superconductivity. In S-N devices with micromagnets, ZPBs under zero external applied magnetic field are observed. These ZPBs can be visually long (present over an extended range in magnetic field or gate voltage) and may even have plateau-like features. Under magnetic field scans, ZBPs are hysteretic and have sharp switching. Again, this proves the effectiveness of local magnetic fields from micromagnets. Instead of MBSs, the origin of observed ZBPs is more likely ABSs. ABSs are topologically trivial but share similar features with MBSs in terms of ZBPs. The magnitude of these trivial ZBPs can be larger than, smaller than or even equal to G_0 [13]. They may appear ubiquitously in a semiconductor nanowire [63]. This ambiguity becomes an essential problem to confirm MBSs in a semiconductor nanowire device. Nevertheless, the local magnetic field effect is confirmed, and this may bring new methods for searching MBSs.

7.2 Efforts for Searching MBSs

Four important components involved in the semiconductor nanowire model are superconductivity, spin-orbit interaction, Zeeman field and chemical potential tuning. Researchers are making efforts to realize a better platform for MBSs by developing better methods to induce superconductivity, to tune chemical potential and to provide Zeeman field. Colleagues with materials science background are also growing new materials with strong spin-orbit coupling. This thesis is aimed at a novel approach of proving the Zeeman field. we will discuss efforts from other researchers below.

7.2.1 Superconducting Proximity

The assessment of induced superconductivity is commonly based on the quality of the induced superconducting gap. We usually talk about soft gaps and hard gaps. For a soft gap, the conductance inside the gap may be finite, indicating unwanted low-energy states inside the gap. MBSs are energy states inside a gap and these unwanted energy states may confuse us in terms of understanding the features of MBSs. For a hard gap, measured conductance inside the gap is zero. Of course, even in this case, topologically trivial states, for example, ABSs may still appear inside the gap.

Compared to data from earlier experiments [6, 7, 10, 136], the quality of induced superconducting gaps is indeed much better nowadays. To induce a hard gap, researchers are trying to find better normal superconductors or to form better interfaces between superconductors and semiconductors. Some typical superconductors are Nb [10], NbTiN [6, 13, 55, 62, 63] and Al [7]. In recent years, superconducting Sn is also tested for InSb nanowires and the results are promising [81]. A straightforward method for contact formation is to deposit these metals by thin film deposition techniques. To have a better contact interface, techniques are developed to deposit superconducting metals in situ when the nanowires are grown and some of the superconductors are claimed to be under epitaxy growth [8, 20, 21, 79, 81, 137, 138]. Shadow techniques are developed to form high quality S-N or S-N-S junctions in situ [81, 82]. Additionally, there is a shadow-wall technique [139] which is beneficial for fabrication of hybrid superconductor–semiconductor devices. With these more advanced techniques, a smooth thin shell of superconductors may form on nanowires. The quality of induced gaps becomes better and fabrication processes can also be simplified.

7.2.2 Spin-orbit Interaction

The most commonly used semiconductor nanowires for MBSs are InSb and InAs nanowires due to their strong spin-orbit interaction. Spin-orbit interaction is an intrinsic property of the materials. Besides InSb and InAs, we are searching for more materials with strong spin-orbit interaction. Alloys of heavier elements may have stronger spin-orbit interaction. For example, PbTe nanowires may also have strong spin-orbit interaction and be platforms for MBSs [41, 83].

Theoretically, it is possible to use magnetic textures to relax the requirement of strong spin-orbit interaction [123]. We need more data from experiments to test the feasibility of this idea [124].

7.2.3 Development of Chemical Potential Tuning

The nanowires shown in this thesis are normally placed on a simple back-gate chip. As introduced in Chapter 3, more advanced designs of fine gates are possible to provide more flexible tuning of chemical potential. Development of EBL and thin film deposition technologies may provide the possibility to design and fabricate even more complicated and robust gate structures.

7.2.4 Other Development

An interesting development is that semiconductor nanowires may be grown by a method called selective area growth (SAG) [140-142]. In short, SAG allows nanowire to grow in desired locations on a substrate. By this method, we do not need to transfer nanowires from a grown chip.

It is a promising method to grow arrays of semiconductor nanowires on a substrate with gates. SAG may bring us a route for industrial applications of topological qubits.

7.2.5 Personal Comment on the History of Searching for MBSs in Hybrid Superconductor-semiconductor Nanowire Devices

The theories about MBSs in condensed matter physics are widely recognized by related researchers. However, experimental confirmation of MBSs is still an open question. The first experiment claiming observation of signatures (ZBPs) of MBSs in hybrid superconductor-semiconductor nanowire devices attracts lots of attention [6]. After more than ten years of studying similar devices, we now understand that simple observation of ZBPs cannot be solid evidence of MBSs. I am lucky to work in a research group which also contributes to learning this crucial point [13, 63].

In this thesis, we also explained why simply observing of ZBPs cannot be solid evidence for MBSs based on my experiments. The novel contribution of my work is using local magnetic fields from ferromagnets, which provides possibility to induce MBSs at zero external magnetic field. It is possible to observe visually long ZBPs present over an extended range in external magnetic field or chemical potential. Similar data are reported from other groups which also consider using ferromagnetic components [21]. Instead of attributing to local magnetic fields, a layer of ferromagnetic insulator may provide Zeeman field through ferromagnetic exchange coupling. However, possible local magnetic field effect may also exist for ferromagnetic insulators and further experiments may be performed to clarify this possibility. Additionally, I want to emphasize again the importance of verifying the origin of any observed ZBPs.

7.3 Outlook

From my personal point of view, the investigation of MBSs in a hybrid superconductor-semiconductor nanowire device is more or less obstructed by ambiguous features from topologically trivial states inside the induced superconducting gap. Efforts from better induced gaps and higher quality of materials may be beneficial towards final realization of MBSs. Nevertheless, we may need to develop better methods to confirm the existence of MBSs.

A simple approach to confirm MBSs in a semiconductor nanowire is to use a three-terminal setup to monitor the pair of MBSs simultaneously. Unfortunately, up till now, there is still no data to present this pair [13]. However, researchers may need to use this three-terminal setup to understand the origin of any observed ZBPs. Or researchers may develop other methods to confirm any topological states.

There are also other platforms predicted for Majorana fermions. For example, chiral Majorana modes may exist in quantum anomalous Hall-superconductor devices. There is still no experimental evidence to find these Majorana modes [143]. The concept of chiral Majorana modes is not quite the same as MBSs in a hybrid superconductor-semiconductor nanowire device. Any observation of chiral Majorana modes may still prove some essential properties of Majorana fermions and gives us some insights of topological states. Researchers may also give efforts of investigation to Majorana fermions in a variety of platforms [144-146]. Better approaches may appear in this process.

Additionally, demonstration of braiding may provide insights for MBSs. Braiding is also a milestone for topological qubits. People may consider braiding of MBSs in future experiments. Difficulties may appear for any braiding experiments, given the uncertainty of existence of MBSs in any platforms. Nevertheless, any successful demonstration of braiding will be very important

and all researchers in the related research area will be rewarded by this achievement. I wish that we may finally find MBSs, and the dream of topologically protected quantum computing will be realized in a reasonable time.

Appendix A Recipes of Fabrication

Substrate Cleaning:

- Ultrasonic cleaning in Acetone for 1 min
- Ultrasonic cleaning in IPA for 1 min
- Baking at 125° for 1 min.
- 200 W Oxygen plasma cleaning for 1 min.
- The time for ultrasonic cleaning and oxygen plasm cleaning can be adjusted depending on real conditions.

Spin-coating of PMMA (single-layer):

- PMMA 950 A4 at 2500 rpm for 1 min
- Bake at 175° for 15 min or pumping in vacuum for 12 hours.
- Spin speed can be adjusted to achieve desired PMMA thickness.

Spin-coating of PMMA (bi-layer):

- PMMA 495 A4 at 2500 rpm for 1 min
- Bake at 175° for 15 min or pumping in vacuum for 12 hours.
- PMMA 950 A2 at 2500 rpm for 1 min
- Bake at 175° for 15 min or pumping in vacuum for 12 hours.
- Spin speed can be adjusted to achieve desired PMMA thickness.

Spin-coating of Photo Resist (single-layer):

- S1805 at 4000 rpm for 1 min
- Bake at 115° for 2 min.

Spin-coating of Photo Resist (bi-layer):

- LOR 5B at 4000 rpm for 1 min
- Bake at 195° for 9 min.
- S1805 at 5000 rpm for 1 min
- Bake at 115° for 5 min.

EBL Process:

- Exposure is at 10 kV, 30 μm aperture and 180 μC/cm^2 dose.
- Dose test can be performed to find a proper dose.

Photolithography Process:

- Exposure is at dose 150 mJ/cm^2 for bi-layer photo resist.
- Exposure is at dose 65 mJ/cm^2 for single-layer photo resist.
- Dose test can be performed to find a proper dose.

Developing for PMMA:

- Developing in MIBK: IPA (1:3) for 60 s, then in IPA for 60 s.
- 200 W Oxygen plasma cleaning for 15-30 s.

Developing for Photo Resist (single-layer):

- Developing in AZ 400K (1:4) for 60 s, then rinsing in water for 30 s.
- 200 W Oxygen plasma cleaning for 15-30 s.

Developing for Photo Resist (bi-layer):

- Developing in CP-26 for 60 s, then rinsing in water for 60 s.
- Developing in AZ 400K (1:4) for 60 s, then rinsing in water for 60 s.
- 200 W Oxygen plasma cleaning for 15-30 s.

Deposition of Ti/Au:

- Deposition of 10 nm Ti and then 140 nm Au.
- The thickness of Ti can be 5 nm. The thickness of Au can be adjusted depending on real situations.

Lift-off for EBL:

- Keep sample in Acetone for 24 hours.
- Squeeze Acetone to remove any left residues.
- Rinse in IPA for 1 min.

Lift-off for Photo resist:

- Keep sample in PG remover for 24 hours.
- Squeeze Acetone to remove any left residues.
- Rinse in water for 1 min.
- Rinse in Acetone for 1 min.
- Rinse in IPA for 1 min.

Deposition of Co or CoFe:

- Deposition of Co or CoFe for desired thickness.
- Deposition of 5-10 Au to protect Co or CoFe from oxidation.

In-situ Ar Plasma Etching in Plassys Electron Beam Evaporation System:

- 500 V Ar plasma etching for 1 min.
- Or 2 cycles of 250 V Ar plasma etching for 40 s.

Chemical Etching for Al/AlO_x on InAs Nanowires:

- Etching in CD26: water (1:20) for 1 min.
- Rinse in water for several seconds.
- Etching in CD26: water (1:20) for another 1 min.

- Rinse in water for 1 min.

Sulfur Passivation for InSb Nanowires:

- Prepare $(NH_4)_2S_x$ solution by mixing 0.29 g sulfur with 3 ml $(NH_4)_2S$.
- Dilute the $(NH_4)_2S_x$ solution with water. The ratio to water is 1:500 or 1:200.
- Keep the sample in 10 mL diluted solution and in 60° water bath for 30 min.
- Rinse the sample in water for 1 min. After the passivation process, the sample needs to be transferred to a vacuum deposition chamber as soon as possible to avoid oxidation.

CoFe or Co Contacts:

- Spin-coating of PMMA (bi-layer).
- EBL writing of windows for contacts and developing.
- Performing sulfur passivation.
- Deposition of CoFe or Co contacts and Au protection layer.
- Performing lift-off.

Normal Contacts:

- Spin-coating of PMMA (bi-layer or single-layer).
- EBL writing of windows for contacts and developing.
- Performing Ar plasm etching in situ.
- Deposition of Ti/Au contacts.
- Performing lift-off.

Fabrication of Gate-chips:

- Spin-coating of photo resist (bi-layer or single-layer).
- Writing windows for leads or gate pads using photolithography.
- Performing developing.

- Deposition of Ti/Au. Typical thickness is 5 nm Ti / 55 nm Au for leads and 5nm Ti / 10 nm Au for gate pads.
- Small markers can be fabricated using the EBL process.

Deposition of HfO_x:

- In necessary, performing ELB process to write windows for deposition of HfO_x.
- Use ALD to deposit the HfO_x layer. A proper temperature needs to be selected to avoid destroying the loaded samples.
- Need ultrasonic for lift-off.

Appendix B List of Publications

Y. Jiang, E.J. de Jong, V. van de Sande, S. Gazibegovic, G. Badawy, E.P.A.M. Bakkers, S.M. Frolov, Hysteretic magnetoresistance in nanowire devices due to stray fields induced by micromagnets, Nanotechnology, 32 (2020) 095001.

M. Jardine, J. Stenger, **Y. Jiang**, E.J. de Jong, W. Wang, A.C. Bleszynski Jayich, S. Frolov, Integrating micromagnets and hybrid nanowires for topological quantum computing, SciPost Physics, 11 (2021) 090.

M. Gomanko, E.J. de Jong, **Y. Jiang**, S.G. Schellingerhout, E. Bakkers, S. Frolov, Spin and Orbital Spectroscopy in the Absence of Coulomb Blockade in Lead Telluride Nanowire Quantum Dots, SciPost Physics, 13 (2022) 089.

S.G. Schellingerhout, E.J. de Jong, M. Gomanko, X. Guan, **Y. Jiang**, M.S.M. Hoskam, J. Jung, S. Koelling, O. Moutanabbir, M.A. Verheijen, S.M. Frolov, E.P.A.M. Bakkers, Growth of PbTe nanowires by molecular beam epitaxy, Materials for Quantum Technology, 2 (2022) 015001.

Appendix C Links of Available Data

Chapter 2: https://zenodo.org/record/5531917

Chapter 4: https://github.com/frolovgroup/Yifan-Jiang

Chapter 5: https://zenodo.org/record/5091744

Bibliography

[1] S.D. Sarma, M. Freedman, C. Nayak, Majorana zero modes and topological quantum computation, npj Quantum Information, 1 (2015) 15001.

[2] V. Lahtinen, J. Pachos, A short introduction to topological quantum computation, SciPost Physics, 3 (2017) 021.

[3] A.Y. Kitaev, Unpaired Majorana fermions in quantum wires, Physics-Uspekhi, 44 (2001) 131.

[4] Y. Oreg, G. Refael, F. von Oppen, Helical liquids and Majorana bound states in quantum wires, Physical review letters, 105 (2010) 177002.

[5] R.M. Lutchyn, J.D. Sau, S. Das Sarma, Majorana Fermions and a Topological Phase Transition in Semiconductor-Superconductor Heterostructures, Physical Review Letters, 105 (2010) 077001.

[6] V. Mourik, K. Zuo, S.M. Frolov, S.R. Plissard, E.P.A.M. Bakkers, L.P. Kouwenhoven, Signatures of Majorana Fermions in Hybrid Superconductor-Semiconductor Nanowire Devices, Science, 336 (2012) 1003-1007.

[7] A. Das, Y. Ronen, Y. Most, Y. Oreg, M. Heiblum, H. Shtrikman, Zero-bias peaks and splitting in an Al–InAs nanowire topological superconductor as a signature of Majorana fermions, Nature Physics, 8 (2012) 887-895.

[8] M.T. Deng, S. Vaitiekėnas, E.B. Hansen, J. Danon, M. Leijnse, K. Flensberg, J. Nygård, P. Krogstrup, C.M. Marcus, Majorana bound state in a coupled quantum-dot hybrid-nanowire system, Science, 354 (2016) 1557-1562.

[9] Ö. Gül, H. Zhang, J.D.S. Bommer, M.W.A. de Moor, D. Car, S.R. Plissard, E.P.A.M. Bakkers, A. Geresdi, K. Watanabe, T. Taniguchi, L.P. Kouwenhoven, Ballistic Majorana nanowire devices, Nature Nanotechnology, 13 (2018) 192-197.

[10] M.T. Deng, C.L. Yu, G.Y. Huang, M. Larsson, P. Caroff, H.Q. Xu, Anomalous Zero-Bias Conductance Peak in a Nb–InSb Nanowire–Nb Hybrid Device, Nano Letters, 12 (2012) 6414-6419.

[11] M. Valentini, M. Borovkov, E. Prada, S. Martí-Sánchez, M. Botifoll, A. Hofmann, J. Arbiol, R. Aguado, P. San-Jose, G. Katsaros, Majorana-like Coulomb spectroscopy in the absence of zero-bias peaks, Nature, 612 (2022) 442-447.

[12] M. Valentini, F. Peñaranda, A. Hofmann, M. Brauns, R. Hauschild, P. Krogstrup, P. San-Jose, E. Prada, R. Aguado, G. Katsaros, Nontopological zero-bias peaks in full-shell nanowires induced by flux-tunable Andreev states, Science, 373 (2021) 82-88.

[13] P. Yu, J. Chen, M. Gomanko, G. Badawy, E.P.A.M. Bakkers, K. Zuo, V. Mourik, S.M. Frolov, Non-Majorana states yield nearly quantized conductance in proximatized nanowires, Nature Physics, 17 (2021) 482-488.

[14] H. Pan, S. Das Sarma, Physical mechanisms for zero-bias conductance peaks in Majorana nanowires, Physical Review Research, 2 (2020) 013377.

[15] S. Zhang, S.A. Dayeh, Y. Li, S.A. Crooker, D.L. Smith, S.T. Picraux, Electrical spin injection and detection in silicon nanowires through oxide tunnel barriers, Nano Lett, 13 (2013) 430-435.

[16] S. Heedt, C. Morgan, K. Weis, D.E. Burgler, R. Calarco, H. Hardtdegen, D. Grutzmacher, T. Schapers, Electrical spin injection into InN semiconductor nanowires, Nano Lett, 12 (2012) 4437-4443.

[17] J. Tarun, S. Huang, Y. Fukuma, H. Idzuchi, Y. Otani, N. Fukata, K. Ishibashi, S. Oda, Demonstration of spin valve effects in silicon nanowires, Journal of Applied Physics, 109 (2011).

[18] F. Zwanenburg, D. Van der Mast, H. Heersche, L. Kouwenhoven, E. Bakkers, Electric field control of magnetoresistance in InP nanowires with ferromagnetic contacts, Nano letters, 9 (2009) 2704-2709.

[19] H. Kum, J. Heo, S. Jahangir, A. Banerjee, W. Guo, P. Bhattacharya, Room temperature single GaN nanowire spin valves with FeCo/MgO tunnel contacts, Applied Physics Letters, 100 (2012).

[20] Y. Liu, S. Vaitiekėnas, S. Martí-Sánchez, C. Koch, S. Hart, Z. Cui, T. Kanne, S.A. Khan, R. Tanta, S. Upadhyay, M.E. Cachaza, C.M. Marcus, J. Arbiol, K.A. Moler, P. Krogstrup, Semiconductor–Ferromagnetic Insulator–Superconductor Nanowires: Stray Field and Exchange Field, Nano Letters, 20 (2020) 456-462.

[21] S. Vaitiekėnas, Y. Liu, P. Krogstrup, C.M. Marcus, Zero-bias peaks at zero magnetic field in ferromagnetic hybrid nanowires, Nature Physics, DOI 10.1038/s41567-020-1017-3(2020).

[22] R. Singh, B. Muralidharan, Conductance spectroscopy of Majorana zero modes in superconductor-magnetic insulator nanowire hybrid systems, Communications Physics, 6 (2023) 36.

[23] A. Maiani, R. Seoane Souto, M. Leijnse, K. Flensberg, Topological superconductivity in semiconductor--superconductor--magnetic-insulator heterostructures, Physical Review B, 103 (2021) 104508.

[24] N. Mohanta, T. Zhou, J.-W. Xu, J.E. Han, A.D. Kent, J. Shabani, I. Žutić, A. Matos-Abiague, Electrical Control of Majorana Bound States Using Magnetic Stripes, Physical Review Applied, 12 (2019) 034048.

[25] S. Turcotte, S. Boutin, J.C. Lemyre, I. Garate, M. Pioro-Ladrière, Optimized micromagnet geometries for Majorana zero modes in low g-factor materials, Physical Review B, 102 (2020) 125425.

[26] L. Fu, C.L. Kane, Superconducting Proximity Effect and Majorana Fermions at the Surface of a Topological Insulator, Physical Review Letters, 100 (2008) 096407.

[27] X.-L. Qi, T.L. Hughes, S.-C. Zhang, Chiral topological superconductor from the quantum Hall state, Physical Review B, 82 (2010) 184516.

[28] J. Wang, Q. Zhou, B. Lian, S.-C. Zhang, Chiral topological superconductor and half-integer conductance plateau from quantum anomalous Hall plateau transition, Physical Review B, 92 (2015) 064520.

[29] E. Majorana, Teoria simmetrica dell'elettrone e del positrone, Il Nuovo Cimento (1924-1942), 14 (2008) 171.

[30] J. Cayao, Hybrid superconductor-semiconductor nanowire junctions as useful platforms to study Majorana bound states, arXiv preprint arXiv:1703.07630, 2017.

[31] M. Tinkham, Introduction to superconductivity, Courier Corporation2004.

[32] A. Kitaev, Periodic table for topological insulators and superconductors, AIP Conference Proceedings, 1134 (2009) 22-30.

[33] P. Marra, Majorana nanowires for topological quantum computation, Journal of Applied Physics, 132 (2022) 231101.

[34] A.P. Schnyder, S. Ryu, A. Furusaki, A.W.W. Ludwig, Classification of Topological Insulators and Superconductors, AIP Conference Proceedings, 1134 (2009) 10-21.

[35] K. Ishida, H. Mukuda, Y. Kitaoka, K. Asayama, Z.Q. Mao, Y. Mori, Y. Maeno, Spin-triplet superconductivity in Sr2RuO4 identified by 17O Knight shift, Nature, 396 (1998) 658-660.

[36] S. Ran, C. Eckberg, Q.-P. Ding, Y. Furukawa, T. Metz, S.R. Saha, I.-L. Liu, M. Zic, H. Kim, J. Paglione, N.P. Butch, Nearly ferromagnetic spin-triplet superconductivity, Science, 365 (2019) 684-687.

[37] D. Aoki, A. Nakamura, F. Honda, D. Li, Y. Homma, Y. Shimizu, Y.J. Sato, G. Knebel, J.-P. Brison, A. Pourret, Unconventional superconductivity in heavy fermion UTe2, journal of the physical society of japan, 88 (2019) 043702.

[38] A. Pustogow, Y. Luo, A. Chronister, Y.S. Su, D.A. Sokolov, F. Jerzembeck, A.P. Mackenzie, C.W. Hicks, N. Kikugawa, S. Raghu, E.D. Bauer, S.E. Brown, Constraints on the superconducting order parameter in Sr2RuO4 from oxygen-17 nuclear magnetic resonance, Nature, 574 (2019) 72-75.

[39] P.F.S. Rosa, A. Weiland, S.S. Fender, B.L. Scott, F. Ronning, J.D. Thompson, E.D. Bauer, S.M. Thomas, Single thermodynamic transition at 2 K in superconducting UTe2 single crystals, Communications Materials, 3 (2022) 33.

[40] V.S. Pribiag, S. Nadj-Perge, S.M. Frolov, J.W. van den Berg, I. van Weperen, S.R. Plissard, E.P. Bakkers, L.P. Kouwenhoven, Electrical control of single hole spins in nanowire quantum dots, Nat Nanotechnol, 8 (2013) 170-174.

[41] M. Gomanko, E.J. de Jong, Y. Jiang, S.G. Schellingerhout, E. Bakkers, S. Frolov, Spin and Orbital Spectroscopy in the Absence of Coulomb Blockade in Lead Telluride Nanowire Quantum Dots, SciPost Physics, 13 (2022) 089.

[42] R. Hanson, L.P. Kouwenhoven, J.R. Petta, S. Tarucha, L.M. Vandersypen, Spins in few-electron quantum dots, Reviews of modern physics, 79 (2007) 1217.

[43] L.P. Kouwenhoven, D.G. Austing, S. Tarucha, Few-electron quantum dots, Reports on Progress in Physics, 64 (2001) 701.

[44] C.W.J. Beenakker, Theory of Coulomb-blockade oscillations in the conductance of a quantum dot, Physical Review B, 44 (1991) 1646-1656.

[45] H.A. Nilsson, P. Caroff, C. Thelander, M. Larsson, J.B. Wagner, L.-E. Wernersson, L. Samuelson, H.Q. Xu, Giant, Level-Dependent g Factors in InSb Nanowire Quantum Dots, Nano Letters, 9 (2009) 3151-3156.

[46] D. Loss, D.P. DiVincenzo, Quantum computation with quantum dots, Physical Review A, 57 (1998) 120-126.

[47] K.D. Petersson, J.R. Petta, H. Lu, A.C. Gossard, Quantum Coherence in a One-Electron Semiconductor Charge Qubit, Physical Review Letters, 105 (2010) 246804.

[48] K.D. Petersson, C.G. Smith, D. Anderson, P. Atkinson, G.A.C. Jones, D.A. Ritchie, Charge and Spin State Readout of a Double Quantum Dot Coupled to a Resonator, Nano Letters, 10 (2010) 2789-2793.

[49] G.E. Blonder, M. Tinkham, T.M. Klapwijk, Transition from metallic to tunneling regimes in superconducting microconstrictions: Excess current, charge imbalance, and supercurrent conversion, Physical Review B, 25 (1982) 4515-4532.

[50] C.-T. Chen, Scanning tunneling spectroscopy studies of high-temperature cuprate superconductors, California Institute of Technology, 2006.

[51] J.A. Gifford, Andreev Reflection Spectroscopy: Theory and Experiment, Arizona State University, 2015.

[52] H. Irie, C. Todt, N. Kumada, Y. Harada, H. Sugiyama, T. Akazaki, K. Muraki, Andreev reflection and bound state formation in a ballistic two-dimensional electron gas probed by a quantum point contact, Physical Review B, 94 (2016) 155305.

[53] B.J. van Wees, H. van Houten, C.W.J. Beenakker, J.G. Williamson, L.P. Kouwenhoven, D. van der Marel, C.T. Foxon, Quantized conductance of point contacts in a two-dimensional electron gas, Physical Review Letters, 60 (1988) 848-850.

[54] E.J.H. Lee, X. Jiang, M. Houzet, R. Aguado, C.M. Lieber, S. De Franceschi, Spin-resolved Andreev levels and parity crossings in hybrid superconductor–semiconductor nanostructures, Nature Nanotechnology, 9 (2014) 79-84.

[55] Z. Su, A.B. Tacla, M. Hocevar, D. Car, S.R. Plissard, E.P. Bakkers, A.J. Daley, D. Pekker, S.M. Frolov, Andreev molecules in semiconductor nanowire double quantum dots, Nature communications, 8 (2017) 585.

[56] P. Zhang, H. Wu, J. Chen, S.A. Khan, P. Krogstrup, D. Pekker, S.M. Frolov, Signatures of Andreev Blockade in a Double Quantum Dot Coupled to a Superconductor, Physical Review Letters, 128 (2022) 046801.

[57] T. Meng, S. Florens, P. Simon, Self-consistent description of Andreev bound states in Josephson quantum dot devices, Physical Review B, 79 (2009) 224521.

[58] I.O. Kulik, Macroscopic Quantization and the Proximity Effect in S-N-S Junctions, Soviet Journal of Experimental and Theoretical Physics, 30 (1969) 944.

[59] B.D. Josephson, Possible new effects in superconductive tunnelling, Physics Letters, 1 (1962) 251-253.

[60] M. Wimmer, A.R. Akhmerov, J.P. Dahlhaus, C.W.J. Beenakker, Quantum point contact as a probe of a topological superconductor, New Journal of Physics, 13 (2011) 053016.

[61] K.T. Law, P.A. Lee, T.K. Ng, Majorana Fermion Induced Resonant Andreev Reflection, Physical Review Letters, 103 (2009) 237001.

[62] J. Chen, P. Yu, J. Stenger, M. Hocevar, D. Car, S.R. Plissard, E.P.A.M. Bakkers, T.D. Stanescu, S.M. Frolov, Experimental phase diagram of zero-bias conductance peaks in superconductor/semiconductor nanowire devices, Science Advances, 3 (2017) e1701476.

[63] J. Chen, B.D. Woods, P. Yu, M. Hocevar, D. Car, S.R. Plissard, E.P.A.M. Bakkers, T.D. Stanescu, S.M. Frolov, Ubiquitous Non-Majorana Zero-Bias Conductance Peaks in Nanowire Devices, Physical Review Letters, 123 (2019) 107703.

[64] S. Zhang, Review of Modern Field Effect Transistor Technologies for Scaling, Journal of Physics: Conference Series, 1617 (2020) 012054.

[65] S.M. Frolov, A. Venkatesan, W. Yu, J.A. Folk, W. Wegscheider, Electrical Generation of Pure Spin Currents in a Two-Dimensional Electron Gas, Physical Review Letters, 102 (2009) 116802.

[66] X. Lou, C. Adelmann, S.A. Crooker, E.S. Garlid, J. Zhang, K.S.M. Reddy, S.D. Flexner, C.J. Palmstrøm, P.A. Crowell, Electrical detection of spin transport in lateral ferromagnet–semiconductor devices, Nature Physics, 3 (2007) 197-202.

[67] S.R. Plissard, D.R. Slapak, M.A. Verheijen, M. Hocevar, G.W.G. Immink, I. van Weperen, S. Nadj-Perge, S.M. Frolov, L.P. Kouwenhoven, E.P.A.M. Bakkers, From InSb Nanowires to Nanocubes: Looking for the Sweet Spot, Nano Letters, 12 (2012) 1794-1798.

[68] G. Badawy, S. Gazibegovic, F. Borsoi, S. Heedt, C.-A. Wang, S. Koelling, M.A. Verheijen, L.P. Kouwenhoven, E.P.A.M. Bakkers, High Mobility Stemless InSb Nanowires, Nano Letters, 19 (2019) 3575-3582.

[69] I. van Weperen, S.R. Plissard, E.P. Bakkers, S.M. Frolov, L.P. Kouwenhoven, Quantized conductance in an InSb nanowire, Nano letters, 13 (2013) 387-391.

[70] I. van Weperen, B. Tarasinski, D. Eeltink, V.S. Pribiag, S.R. Plissard, E.P.A.M. Bakkers, L.P. Kouwenhoven, M. Wimmer, Spin-orbit interaction in InSb nanowires, Physical Review B, 91 (2015).

[71] J.W.G. van den Berg, S. Nadj-Perge, V.S. Pribiag, S.R. Plissard, E.P.A.M. Bakkers, S.M. Frolov, L.P. Kouwenhoven, Fast Spin-Orbit Qubit in an Indium Antimonide Nanowire, Physical Review Letters, 110 (2013) 066806.

[72] S. Nadj-Perge, V.S. Pribiag, J.W.G. van den Berg, K. Zuo, S.R. Plissard, E.P.A.M. Bakkers, S.M. Frolov, L.P. Kouwenhoven, Spectroscopy of Spin-Orbit Quantum Bits in Indium Antimonide Nanowires, Physical Review Letters, 108 (2012) 166801.

[73] G. Badawy, B. Zhang, T. Rauch, J. Momand, S. Koelling, J. Jung, S. Gazibegovic, O. Moutanabbir, B.J. Kooi, S. Botti, M.A. Verheijen, S.M. Frolov, E.P.A.M. Bakkers, Electronic Structure and Epitaxy of CdTe Shells on InSb Nanowires, Advanced Science, 9 (2022) 2105722.

[74] S.A. Dayeh, D.P.R. Aplin, X. Zhou, P.K.L. Yu, E.T. Yu, D. Wang, High Electron Mobility InAs Nanowire Field-Effect Transistors, Small, 3 (2007) 326-332.

[75] S. Abay, D. Persson, H. Nilsson, H.Q. Xu, M. Fogelström, V. Shumeiko, P. Delsing, Quantized Conductance and Its Correlation to the Supercurrent in a Nanowire Connected to Superconductors, Nano Letters, 13 (2013) 3614-3617.

[76] K. Takase, Y. Ashikawa, G. Zhang, K. Tateno, S. Sasaki, Highly gate-tuneable Rashba spin-orbit interaction in a gate-all-around InAs nanowire metal-oxide-semiconductor field-effect transistor, Scientific Reports, 7 (2017) 930.

[77] M.B. Rota, A.S. Ameruddin, H.A. Fonseka, Q. Gao, F. Mura, A. Polimeni, A. Miriametro, H.H. Tan, C. Jagadish, M. Capizzi, Bandgap Energy of Wurtzite InAs Nanowires, Nano Letters, 16 (2016) 5197-5203.

[78] C. Fasth, A. Fuhrer, L. Samuelson, V.N. Golovach, D. Loss, Direct Measurement of the Spin-Orbit Interaction in a Two-Electron InAs Nanowire Quantum Dot, Physical Review Letters, 98 (2007) 266801.

[79] P. Krogstrup, N.L.B. Ziino, W. Chang, S.M. Albrecht, M.H. Madsen, E. Johnson, J. Nygård, C.M. Marcus, T.S. Jespersen, Epitaxy of semiconductor–superconductor nanowires, Nature Materials, 14 (2015) 400-406.

[80] T. Kanne, M. Marnauza, D. Olsteins, D.J. Carrad, J.E. Sestoft, J. de Bruijckere, L. Zeng, E. Johnson, E. Olsson, K. Grove-Rasmussen, J. Nygård, Epitaxial Pb on InAs nanowires for quantum devices, Nature Nanotechnology, 16 (2021) 776-781.

[81] M. Pendharkar, B. Zhang, H. Wu, A. Zarassi, P. Zhang, C. Dempsey, J. Lee, S. Harrington, G. Badawy, S. Gazibegovic, Parity-preserving and magnetic field–resilient superconductivity in InSb nanowires with Sn shells, Science, 372 (2021) 508-511.

[82] S.A. Khan, C. Lampadaris, A. Cui, L. Stampfer, Y. Liu, S.J. Pauka, M.E. Cachaza, E.M. Fiordaliso, J.-H. Kang, S. Korneychuk, T. Mutas, J.E. Sestoft, F. Krizek, R. Tanta, M.C. Cassidy, T.S. Jespersen, P. Krogstrup, Highly Transparent Gatable Superconducting Shadow Junctions, ACS Nano, 14 (2020) 14605-14615.

[83] S.G. Schellingerhout, E.J. de Jong, M. Gomanko, X. Guan, Y. Jiang, M.S.M. Hoskam, J. Jung, S. Koelling, O. Moutanabbir, M.A. Verheijen, S.M. Frolov, E.P.A.M. Bakkers, Growth of PbTe nanowires by molecular beam epitaxy, Materials for Quantum Technology, 2 (2022) 015001.

[84] A.I. Kingon, J.-P. Maria, S.K. Streiffer, Alternative dielectrics to silicon dioxide for memory and logic devices, Nature, 406 (2000) 1032-1038.

[85] J. Robertson, High dielectric constant gate oxides for metal oxide Si transistors, Reports on Progress in Physics, 69 (2006) 327.

[86] P.O. Oviroh, R. Akbarzadeh, D. Pan, R.A.M. Coetzee, T.-C. Jen, New development of atomic layer deposition: processes, methods and applications, Science and technology of advanced materials, 20 (2019) 465-496.

[87] D.B. Suyatin, C. Thelander, M.T. Björk, I. Maximov, L. Samuelson, Sulfur passivation for ohmic contact formation to InAs nanowires, Nanotechnology, 18 (2007).

[88] B.T. Matthias, T.H. Geballe, V.B. Compton, Superconductivity, Reviews of Modern Physics, 35 (1963) 1-22.

[89] *QT designed instrumentation*. https://qtwork.tudelft.nl/~schouten/

[90] *QTLab*. https://qtlab.sourceforge.net/

[91] Y. Ando, K. Kasahara, K. Yamane, K. Hamaya, K. Sawano, T. Kimura, M. Miyao, Comparison of Nonlocal and Local Magnetoresistance Signals in Laterally Fabricated Fe3Si/Si Spin-Valve Devices, Applied Physics Express, 3 (2010).

[92] O.M.J. van 't Erve, A.T. Hanbicki, M. Holub, C.H. Li, C. Awo-Affouda, P.E. Thompson, B.T. Jonker, Electrical injection and detection of spin-polarized carriers in silicon in a lateral transport geometry, Applied Physics Letters, 91 (2007).

[93] T. Sasaki, T. Oikawa, T. Suzuki, M. Shiraishi, Y. Suzuki, K. Tagami, Electrical Spin Injection into Silicon Using MgO Tunnel Barrier, Applied Physics Express, 2 (2009).

[94] S. Sahoo, T. Kontos, J. Furer, C. Hoffmann, M. Gräber, A. Cottet, C. Schönenberger, Electric field control of spin transport, Nature Physics, 1 (2005) 99-102.

[95] M. Oltscher, F. Eberle, T. Kuczmik, A. Bayer, D. Schuh, D. Bougeard, M. Ciorga, D. Weiss, Gate-tunable large magnetoresistance in an all-semiconductor spin valve device, Nat Commun, 8 (2017) 1807.

[96] F. Mireles, G. Kirczenow, Coherent spin-valve phenomena and electrical spin injection in ferromagnetic/semiconductor/ferromagnetic junctions, Physical Review B, 66 (2002).

[97] J. Yoneda, T. Otsuka, T. Takakura, M. Pioro-Ladrière, R. Brunner, H. Lu, T. Nakajima, T. Obata, A. Noiri, C.J. Palmstrøm, A.C. Gossard, S. Tarucha, Robust micromagnet design for fast

electrical manipulations of single spins in quantum dots, Applied Physics Express, 8 (2015) 084401.

[98] M. Pioro-Ladrière, Y. Tokura, T. Obata, T. Kubo, S. Tarucha, Micromagnets for coherent control of spin-charge qubit in lateral quantum dots, Applied Physics Letters, 90 (2007).

[99] M. Pioro-Ladrière, T. Obata, Y. Tokura, Y.S. Shin, T. Kubo, K. Yoshida, T. Taniyama, S. Tarucha, Electrically driven single-electron spin resonance in a slanting Zeeman field, Nature Physics, 4 (2008) 776-779.

[100] R. Neumann, L.R. Schreiber, Simulation of micro-magnet stray-field dynamics for spin qubit manipulation, Journal of Applied Physics, 117 (2015) 193903.

[101] A. Bordoloi, V. Zannier, L. Sorba, C. Schönenberger, A. Baumgartner, Spin cross-correlation experiments in an electron entangler, Nature, 612 (2022) 454-458.

[102] A. Bordoloi, V. Zannier, L. Sorba, C. Schönenberger, A. Baumgartner, A double quantum dot spin valve, Communications Physics, 3 (2020) 135.

[103] G. Fábián, P. Makk, M.H. Madsen, J. Nygård, C. Schönenberger, A. Baumgartner, Magnetoresistance engineering and singlet/triplet switching in InAs nanowire quantum dots with ferromagnetic sidegates, Physical Review B, 94 (2016).

[104] Y. Jiang, E.J. de Jong, V. van de Sande, S. Gazibegovic, G. Badawy, E.P.A.M. Bakkers, S.M. Frolov, Hysteretic magnetoresistance in nanowire devices due to stray fields induced by micromagnets, Nanotechnology, 32 (2020) 095001.

[105] R. Engel-Herbert, T. Hesjedal, Calculation of the magnetic stray field of a uniaxial magnetic domain, Journal of Applied Physics, 97 (2005).

[106] A. Goldman, Handbook of modern ferromagnetic materials, Springer Science & Business Media2012.

[107] F.J. Jedema, A.T. Filip, B.J. van Wees, Electrical spin injection and accumulation at room temperature in an all-metal mesoscopic spin valve, Nature, 410 (2001) 345-348.

[108] A. Hirohata, K. Yamada, Y. Nakatani, I.-L. Prejbeanu, B. Diény, P. Pirro, B. Hillebrands, Review on spintronics: Principles and device applications, Journal of Magnetism and Magnetic Materials, 509 (2020) 166711.

[109] J. Fabian, A. Matos-Abiague, C. Ertler, P. Stano, I. Žutić, Semiconductor spintronics, Acta Physica Slovaca, 57 (2007) 565.

[110] S. Datta, B. Das, Electronic analog of the electro-optic modulator, Applied Physics Letters, 56 (1990) 665-667.

[111] Z. Yang, B. Heischmidt, S. Gazibegovic, G. Badawy, D. Car, P.A. Crowell, E.P.A.M. Bakkers, V.S. Pribiag, Spin Transport in Ferromagnet-InSb Nanowire Quantum Devices, Nano Letters, 20 (2020) 3232-3239.

[112] Z. Wang, D. Pan, L. Wang, T. Wang, B. Zhao, Y. Wu, M. Yang, X. Xu, J. Miao, J. Zhao, Y. Jiang, Room-temperature spin transport in InAs nanowire lateral spin valve, RSC Advances, 6 (2016) 75736-75740.

[113] C. Bureau-Oxton, Fabrication de nanoaimants pour le contrôle rapide d'un spin électronique dans une boîte quantique double, Université de Sherbrooke, 2014.

[114] A. Manchon, H.C. Koo, J. Nitta, S. Frolov, R. Duine, New perspectives for Rashba spin–orbit coupling, Nature materials, 14 (2015) 871-882.

[115] S.J. van der Molen, N. Tombros, B.J. van Wees, Magneto-Coulomb effect in spin-valve devices, Physical Review B, 73 (2006).

[116] Y. Fukuma, Z. Lu, H. Fujiwara, G.J. Mankey, W.H. Butler, S. Matsunuma, Strong uniaxial magnetic anisotropy in CoFe films on obliquely sputtered Ru underlayer, Journal of Applied Physics, 106 (2009) 076101.

[117] T.H. Kim, Y.H. Jeong, J.S. Kang, Structural and magnetic properties of CoFe alloy films, Journal of Applied Physics, 81 (1997) 4764-4766.

[118] C.L. Platt, A.E. Berkowitz, D.J. Smith, M.R. McCartney, Correlation of coercivity and microstructure of thin CoFe films, Journal of Applied Physics, 88 (2000) 2058-2062.

[119] Q. Mustaghfiroh, C. Kurniawan, D. Djuhana, Magnetization Dynamic Analysis of Square Model CoFe and CoFeB Ferromagnetic Materials Using Micromagnetic Simulation, IOP Conference Series: Materials Science and Engineering, 553 (2019) 012009.

[120] A. Vansteenkiste, J. Leliaert, M. Dvornik, M. Helsen, F. Garcia-Sanchez, B. Van Waeyenberge, The design and verification of MuMax3, AIP advances, 4 (2014) 107133.

[121] L. Exl, S. Bance, F. Reichel, T. Schrefl, H.P. Stimming, N.J. Mauser, LaBonte's method revisited: An effective steepest descent method for micromagnetic energy minimization, Journal of Applied Physics, 115 (2014) 17D118.

[122] J. Klinovaja, P. Stano, D. Loss, Transition from Fractional to Majorana Fermions in Rashba Nanowires, Physical Review Letters, 109 (2012) 236801.

[123] M. Kjaergaard, K. Wölms, K. Flensberg, Majorana fermions in superconducting nanowires without spin-orbit coupling, Physical Review B, 85 (2012) 020503.

[124] M.M. Desjardins, L.C. Contamin, M.R. Delbecq, M.C. Dartiailh, L.E. Bruhat, T. Cubaynes, J.J. Viennot, F. Mallet, S. Rohart, A. Thiaville, A. Cottet, T. Kontos, Synthetic spin–orbit interaction for Majorana devices, Nature Materials, 18 (2019) 1060-1064.

[125] L.N. Maurer, J.K. Gamble, L. Tracy, S. Eley, T.M. Lu, Designing Nanomagnet Arrays for Topological Nanowires in Silicon, Physical Review Applied, 10 (2018) 054071.

[126] M. Jardine, J. Stenger, Y. Jiang, E.J. de Jong, W. Wang, A.C. Bleszynski Jayich, S. Frolov, Integrating micromagnets and hybrid nanowires for topological quantum computing, SciPost Physics, 11 (2021) 090.

[127] J.P.T. Stenger, B.D. Woods, S.M. Frolov, T.D. Stanescu, Control and detection of Majorana bound states in quantum dot arrays, Physical Review B, 98 (2018) 085407.

[128] L. Jiang, D. Pekker, J. Alicea, G. Refael, Y. Oreg, A. Brataas, F. von Oppen, Magneto-Josephson effects in junctions with Majorana bound states, Physical Review B, 87 (2013) 075438.

[129] D. Aasen, M. Hell, R.V. Mishmash, A. Higginbotham, J. Danon, M. Leijnse, T.S. Jespersen, J.A. Folk, C.M. Marcus, K. Flensberg, J. Alicea, Milestones Toward Majorana-Based Quantum Computing, Physical Review X, 6 (2016) 031016.

[130] J. Alicea, Y. Oreg, G. Refael, F. von Oppen, M.P.A. Fisher, Non-Abelian statistics and topological quantum information processing in 1D wire networks, Nature Physics, 7 (2011) 412-417.

[131] R.L. Fagaly, Superconducting quantum interference device instruments and applications, Review of Scientific Instruments, 77 (2006) 101101.

[132] E. Prada, P. San-Jose, M.W.A. de Moor, A. Geresdi, E.J.H. Lee, J. Klinovaja, D. Loss, J. Nygård, R. Aguado, L.P. Kouwenhoven, From Andreev to Majorana bound states in hybrid superconductor–semiconductor nanowires, Nature Reviews Physics, 2 (2020) 575-594.

[133] H.A. Nilsson, P. Samuelsson, P. Caroff, H.Q. Xu, Supercurrent and Multiple Andreev Reflections in an InSb Nanowire Josephson Junction, Nano Letters, 12 (2012) 228-233.

[134] H. Pan, C.-X. Liu, M. Wimmer, S. Das Sarma, Quantized and unquantized zero-bias tunneling conductance peaks in Majorana nanowires: Conductance below and above $2{e}^{2}/h$, Physical Review B, 103 (2021) 214502.

[135] W. Chang, Superconducting proximity effect in InAs nanowires, Harvard University, 2014.

[136] S.T. Gill, J. Damasco, D. Car, E.P.A.M. Bakkers, N. Mason, Hybrid superconductor-quantum point contact devices using InSb nanowires, Applied Physics Letters, 109 (2016) 233502.

[137] S.A. Khan, S. Martí-Sánchez, D. Olsteins, C. Lampadaris, D.J. Carrad, Y. Liu, J. Quiñones, M.C. Spadaro, T.S. Jespersen, P. Krogstrup, Epitaxially Driven Phase Selectivity of Sn in Hybrid Quantum Nanowires, arXiv preprint arXiv:2212.13314, DOI (2022).

[138] T. Elalaily, O. Kürtössy, Z. Scherübl, M. Berke, G. Fülöp, I.E. Lukács, T. Kanne, J. Nygård, K. Watanabe, T. Taniguchi, P. Makk, S. Csonka, Gate-Controlled Supercurrent in Epitaxial Al/InAs Nanowires, Nano Letters, 21 (2021) 9684-9690.

[139] S. Heedt, M. Quintero-Pérez, F. Borsoi, A. Fursina, N. van Loo, G.P. Mazur, M.P. Nowak, M. Ammerlaan, K. Li, S. Korneychuk, J. Shen, M.A.Y. van de Poll, G. Badawy, S. Gazibegovic, N. de Jong, P. Aseev, K. van Hoogdalem, E. Bakkers, L.P. Kouwenhoven, Shadow-wall lithography of ballistic superconductor-semiconductor quantum devices, Nat Commun, 12 (2021) 4914.

[140] P. Aseev, G. Wang, L. Binci, A. Singh, S. Martí-Sánchez, M. Botifoll, L.J. Stek, A. Bordin, J.D. Watson, F. Boekhout, D. Abel, J. Gamble, K. Van Hoogdalem, J. Arbiol, L.P. Kouwenhoven,

G. de Lange, P. Caroff, Ballistic InSb Nanowires and Networks via Metal-Sown Selective Area Growth, Nano Letters, 19 (2019) 9102-9111.

[141] R.L.M. Op het Veld, D. Xu, V. Schaller, M.A. Verheijen, S.M.E. Peters, J. Jung, C. Tong, Q. Wang, M.W.A. de Moor, B. Hesselmann, K. Vermeulen, J.D.S. Bommer, J. Sue Lee, A. Sarikov, M. Pendharkar, A. Marzegalli, S. Koelling, L.P. Kouwenhoven, L. Miglio, C.J. Palmstrøm, H. Zhang, E.P.A.M. Bakkers, In-plane selective area InSb–Al nanowire quantum networks, Communications Physics, 3 (2020) 59.

[142] D.V. Beznasyuk, S. Martí-Sánchez, J.-H. Kang, R. Tanta, M. Rajpalke, T. Stankevič, A.W. Christensen, M.C. Spadaro, R. Bergamaschini, N.N. Maka, C.E.N. Petersen, D.J. Carrad, T.S. Jespersen, J. Arbiol, P. Krogstrup, Doubling the mobility of InAs/InGaAs selective area grown nanowires, Physical Review Materials, 6 (2022) 034602.

[143] M. Kayyalha, D. Xiao, R. Zhang, J. Shin, J. Jiang, F. Wang, Y.-F. Zhao, R. Xiao, L. Zhang, K.M. Fijalkowski, P. Mandal, M. Winnerlein, C. Gould, Q. Li, L.W. Molenkamp, M.H.W. Chan, N. Samarth, C.-Z. Chang, Absence of evidence for chiral Majorana modes in quantum anomalous Hall-superconductor devices, Science, 367 (2020) 64-67.

[144] S. Nadj-Perge, I.K. Drozdov, J. Li, H. Chen, S. Jeon, J. Seo, A.H. MacDonald, B.A. Bernevig, A. Yazdani, Observation of Majorana fermions in ferromagnetic atomic chains on a superconductor, Science, 346 (2014) 602-607.

[145] D. Wang, L. Kong, P. Fan, H. Chen, S. Zhu, W. Liu, L. Cao, Y. Sun, S. Du, J. Schneeloch, R. Zhong, G. Gu, L. Fu, H. Ding, H.-J. Gao, Evidence for Majorana bound states in an iron-based superconductor, Science, 362 (2018) 333-335.

[146] F. Lüpke, D. Waters, S.C. de la Barrera, M. Widom, D.G. Mandrus, J. Yan, R.M. Feenstra, B.M. Hunt, Proximity-induced superconducting gap in the quantum spin Hall edge state of monolayer WTe2, Nature Physics, 16 (2020) 526-530.